Department of Precision and Microsystems Engineering

A Cryogenic Positioning System for Linear Variable Filter Optical Characterization

Joris Hooftman

Report no : 2024.055
Coach : Dr. N. (Nandini) Bhattacharya
Professor : Dr. N. (Nandini) Bhattacharya
Specialisation : Opto-Mechatronics
Type of report : Master Thesis
Date : 30 July 2024

A Cryogenic Positioning System for Linear Variable Filter Optical Characterization

by

Joris Hooftman

to obtain the degree of Master of Science
at the Delft University of Technology,
to be defended publicly on Thursday August 22, 2024 at 14:30.

Faculty:	Mechanical Engineering	
Department:	Precision and Microsystems Engineering	
Master Track:	High-Tech Engineering	
Project duration:	September 1, 2023 – August 31, 2024	
Student:	Joris Hooftman	4579070
Supervision:	Dr. N. (Nandini) Bhattacharya	TU Delft
	Dr. ir. W. (Willem) Jellema	SRON
	Ing. M.J. (Martin) Eggens	SRON
Committee:	Dr. N. (Nandini) Bhattacharya	TU Delft
	Dr. ir. W. (Willem) Jellema	SRON
	Ing. M.J. (Martin) Eggens	SRON
	Dr. O. (Omid) Nejadseyfi	TU Delft

An electronic version of this thesis is available at `https://repository.tudelft.nl/`.

TU Delft

SRON
Netherlands Institute for Space Research

Thank you Mom and Dad, for providing me with opportunities to grow.

Abstract

PRobe far-Infrared Mission for Astrophysics (PRIMA) is a cryogenically cooled NASA mission aimed at making hyperspectral observations in the far infrared. The Netherlands Institute for Space Research (SRON) will design and manufacture a Linear Variable Filter (LVF) for use within PRIMA's optics. In the design and manufacture of the LVF it is essential to characterize its optical properties. This is done by scanning a laser beam over the LVF's surface while at 4.2 K within a cryostat by means of a cryogenic positioning system. This research is tasked with designing that cryogenic positioning system; which must be capable of 2 degree-of-freedom planar motion to scan the the 40×20 mm surface of the LVF, with steps of 25 µm and an uncertainty in LVF position of ± 2.5 µm. Additionally, the mechanism must fit within the cryostat, and must be able to bring the LVF to a position that is out of the laser beam, resulting in a total horizontal range of motion of 57.5 mm. Due to the large range of motion, high accuracy requirements, low temperature, and limited available space, off-the-shelf solutions are not viable. A custom, highly integrated, solution must be developed. The far-infrared and cryogenic context requires that heat dissipation is kept to a minimum, and has consequences for the applicability of standard components such as ball bearings.

The design process begins with divergent concept generation. Through the course of two downselects, concepts of lesser promise are eliminated. The final concept consists of a 5-bar mechanism with a parallelogram to constrain the rotation of the LVF. It is driven by two stepper motors. Through the use of a MATLAB model, the lengths of the links that define the mechanism are optimized. A Monte Carlo tolerance analysis is performed to calculate the expected performance of the manufactured mechanism. Lastly, the theoretical mechanism is materialized as a CAD model.

The final design of the mechanism is capable of scanning the 40×20 mm surface of the LVF with steps of 25 µm or smaller; meeting the target requirement. The worst-case position uncertainty of of the LVF is approximately ± 5 µm; twice larger than the target requirement. The estimated heat dissipation is twice the targeted requirement, at 19.4 mW. The detent torque of the recommended stepper motor-gearbox combination provides a safety factor of 12.6 over the maximum torque required by the mechanism.

This page is intentionally left blank.

Contents

1 Introduction

NASA's PRobe far-Infrared Mission for Astrophysics (PRIMA) is an actively cryogenically-cooled, far-infrared space observatory planned for launch to an L2 orbit in the 2030 decade [1][2][3]. PRIMA is designed to reveal how abundant elements are built up in galaxies over cosmic time. It will make observations spanning the far infrared wavelengths of 24 to 240 µm, filling the under-explored gap in-between the James Webb Space Telescope (JWST) and the ground based Atacama Large Millimeter/submillimeter Array (ALMA) [1][3]. To reach the target sensitivity in the 24–240 µm wavelength range PRIMA's detectors must be kept at 0.1 K and its optics at 4.5 K [3]. These extreme temperatures are achieved with a cryogen-free cooling system using a combination of passive radiators and thermal shields, a hybrid mechanical cooler and a continuous Adiabatic Demagnetization Refrigerator system [3]. The Netherlands Institute for Space Research (SRON) is involved in the PRIMA mission and plays a key role in the research and development of PRIMAger: PRIMA's hyperspectral imager. PRIMAger's hyperspectral imaging capabilities within the compact volume of a space probe are in part enabled by the state of the art Linear Variable Filter (LVF) planned for use within its 4.5 K optics. Never before has an LVF been manufactured with such large dimensions, destined for cryogenic use and with such performance so far into the infrared. Consequently, it is essential to close the loop between modelling, designing and manufacturing. This is done by characterising the optical properties of the LVF. This allows for a feedback loop, enabling evaluation of the applied models and manufacturing techniques and enabling focused iteration of the LVF design to ensure it meets the requirements set by PRIMA.

The working principle of an LVF is based on the variation of its cavity length along one of its spatial dimensions. LVFs operate in a similar fashion to an array of Fabry-Perot (FP) type optical bandpass filters lined up side-by-side, where each FP transmits different resonant wavelengths due to its slightly different cavity length. In principle this results in an unlimited number of FP filters [4]. The FP shown in Figure 1.1a transmits wavelengths which satisfy the resonance condition $\lambda = 2d\cos\theta/m$ where m is the integer order and d (cavity length) and θ (incidence angle with respect to the normal) are constant [5]. One can see that in the case of the LVF shown in Figure 1.1b the cavity length d varies along the length of the LVF. This creates a continuum of resonance conditions and therefore a spatially separated continuum of transmitted wavelengths. This characteristic allows for spectral filtering over a wide range of wavelengths within a compact volume.

The specific design pursued by SRON does not involve dielectric mirrors and a traditional tapered FP design as shown in Figure 1.1b. This design strategy is not feasible for wavelengths in the far-infrared. The SRON design makes use of graded resonant metal-mesh filters spaced by a fixed cavity. The operating principle, and resulting output, is however equivalent to what is depicted in Figure 1.1b.

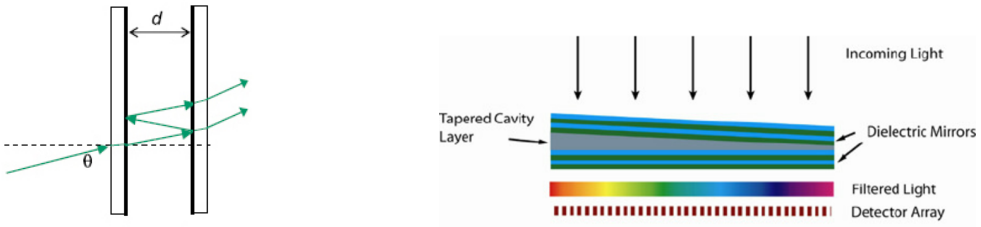

(a) adapted from [5]

(b) [4]

Figure 1.1: Diagrams of a Fabry-Perot etalon (a) and an LVF (b).

2 System Requirements

Due to the spatial variation of the LVF's properties it is necessary to characterise its optical performance at different points along its surface. The aim is to create a map of its local bandpass. This characterisation can occur in three different modes. In each case it consist of illuminating a point on – or the whole surface of – the LVF with light from a laser source, and measuring the light transmitted through LVF. The source is either a tunable laser, or a broadband thermal source. In the case of the broadband source, a Fourier Transform Spectrometer (FTS) setup is required. This consists of a Michelson interferometric arrangement and a broadband detector. This is required to be able to determine the wavelength of the transmitted light. In the case of the tunable laser source, this is not necessary, as the wavelength of the source is already known.

Furthermore, the LVF is destined for cryogenic operating conditions (4.5 K). The LVF's characterisation should occur at similar conditions as it is possible that the change in temperature effects its characteristics. This is achieved by placing the LVF within a cryostat where the environment is cooled using evaporating liquid helium. In the lab, cryogenic liquids are preferred over mechanical coolers due to their simplicity. Liquid helium is used due to its 4.2 K boiling point at atmospheric pressure [6], which is close to the operating conditions of the LVF within PRIMA. The aim is to measure the local bandpass of the LVF, and the research goal follows: design a setup capable of scanning the laser beam over the LVF (with a given step size in between the different positions) while it is inside the cryostat.

The cryostat available at SRON is a modified version of a HDL10 dewar cryostat from IRLabs [7]. A drawing of a model HDL10 is shown in Figure 2.1a . The CAD model of the working area assembly of the modified SRON version is shown in Figure 2.1b. Pictures of the SRON cryostat are shown in Figures 2.1d and 2.1e. Lastly the CAD model of the SRON LVF is shown in 2.1c. When in use, the cryostat will be flipped around to have the cryogenic storage tanks positioned above the working area assembly as to ensure contact between the cryogens and the cold working surface.

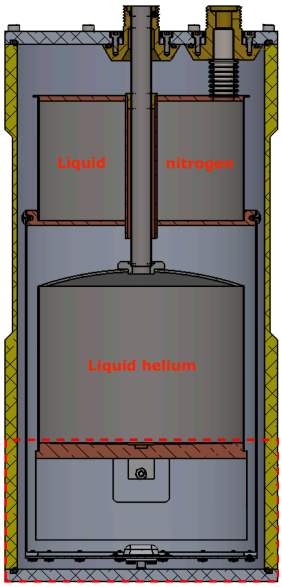

(a) A cross section of the IRLabs HDL10 dewar cryostat; adapted from [7]. The cryostat at SRON is a modified version of the HDL10. The working area assembly (highlighted by the dashed red rectangle) is shown in higher detail in (b).

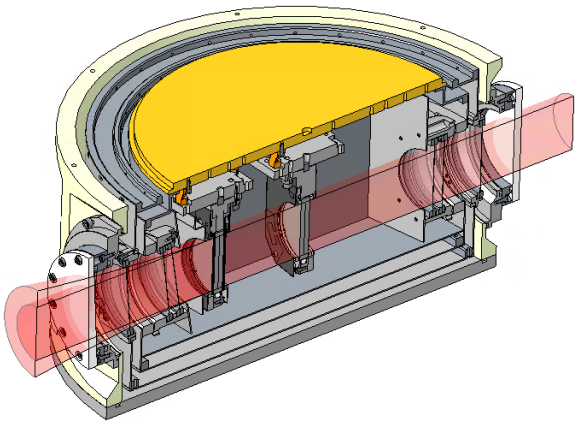

(b) A CAD model of working area assembly of the cryostat. The yellow surface is the cold working surface which is in contact with the liquid helium held in the reservoir above it.

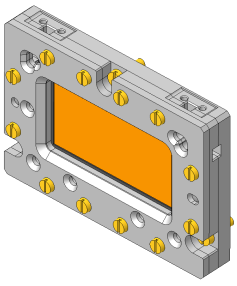

(c) A CAD model of the SRON LVF.

(d) A picture of the cryostat at SRON. When in use the cryostat would be flipped around as to have the gold colored cryogen reservoir assembly on top of the silver colored working area assembly.

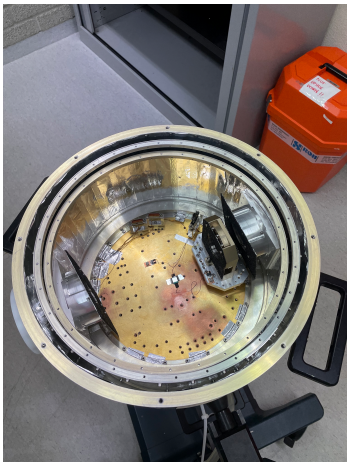

(e) A picture of the inside of the cryostat.

Figure 2.1: Details on the cryostat and LVF.

2.1. Target Functions and Performance

A key aspect of the project is its open-ended, system engineering nature. It consists of a broad spectrum of potential functions and criteria that would ideally all be incorporated into the design; however, their combination may prove to be infeasible or undesirable. The system-engineering challenge lies in determining the feasibility of combining these objectives and assessing the trade-offs related to each function or criteria in order to reach an optimal solution. Imagine the following scenario: to achieve a certain functionality 'X', a large range of motion is required. This large range of motion in turn makes the use of compliant mechanisms (which were preferred) infeasible. It therefore necessitates the use of ball-bearings (not preferred). A choice must be made: is the loss of compliant mechanism compatibility worth the gain that function 'X' offers? A system engineering approach requires evaluation of whether the gains from certain design choices are worth the concessions they demand. Due to this system engineering nature of the project, initially the ideal objectives and the maximum realistic expectations will be outlined. As the research and development of the design progresses, these ideal goals will be continually evaluated and modified with regards to their benefits and potential negative impacts on the system. The culmination of this process will be a final design that aims to provide an optimal balance between what is achievable and what is desirable, ensuring that the system performs as effectively as possible within the given constraints.

2.1.1. Functions

As mentioned earlier, the primary function of the system is to measure the local bandpass of the LVF. This can be achieved in 3 different measurement modes; focused, collimated, and position-scan. In the **focused mode** the laser beam is focused to a single point. The LVF is then moved into position as to illuminate the point on its surface that is to be tested. The laser source then sweeps over a given continuum of wavelengths, or in the case of the broadband source, is measured using using the FTS. Both allow for the measurement of the resonant wavelength at that position on the LVF. After the measurement occurs the LVF must move out of the beam; this way an unobstructed background measurement can be made of the laser light. This process is repeated for every point on the LVF. In the **collimated mode** the laser light is collimated and the beam's diameter is so large as to illuminate the entire optical surface of the LVF all at once. As before, a wavelength sweep is done or the broadband source is measured with the FTS. The measurements of the transmitted light are made and the LVF must move out of the beam afterwards. In this mode there is no need for repeated measurements since the entire LVF is measured at once. This mode in particular is required for the verification of uniform grid pattern samples, which serve as the foundational building blocks for subsequent LVF designs. In the **position-scan mode** the laser light is focused like in the focused mode. However instead of sweeping the wavelength of the source or measuring it with the FTS, it is the LVF's position that is swept. It is moved

continuously in a line as to continuously illuminate a different point along its surface on that line. Once the line sweep is completed the LVF must move out of the beam to obtain the unobstructed background measurement of the laser light. This process is repeated for each line on the LVF. The system must be able to perform the focused mode measurement; the collimated and position-scan measurements are optional.

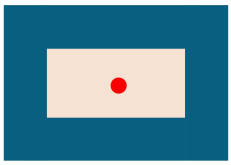

(a) Focused mode. The laser beam is focused to a point and its wavelength is continuously varied to sweep over a given range.

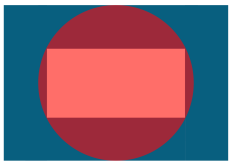

(b) Collimated mode. The laser beam is collimated as to illuminate the entire optical area of the LVF and the wavelength is continuously varied to sweep over a given range.

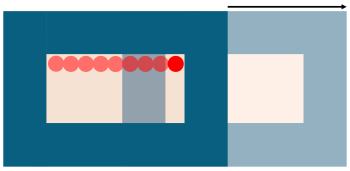

(c) Position-scan mode. The laser beam is focused to a point, its wavelength kept constant, and the position of the LVF is swept.

Figure 2.2: Three different modes of measuring the local bandpass of the LVF.

2.1.2. Performance

Range of motion (ROM): $77.5 \times 20\,\text{mm}$

The LVF has an optical area of $40 \times 20\,\text{mm}$ and its holder has a width of 12.5 mm around each edge. The window in the cryostat has a radius of 25 mm. The range of motion of the system must be able to cover the optical area of the LVF, and must be able to move the LVF out of the beam in X direction. For the focused mode this adds $1\times$ the thickness of the LVF holder (12.5 mm) to the ROM in either the X direction. To be able to move out of the beam in the collimated mode the LVF must completely clear the window, adding another 25 mm ($1\times$ cryostat window radius) to the ROM in the X direction. A system capable of the collimated measurement mode therefore has a ROM of $77.5 \times 20\,\text{mm}$. Figure 2.3 shows a visual description of these different movements. The system must be able to scan the optical area of the LVF (Figures 2.3a–2.3c) and must be able to exit the beam in X direction (Figures 2.3d–2.3e). Exiting the beam in Y direction is not feasible as there is insufficient space.

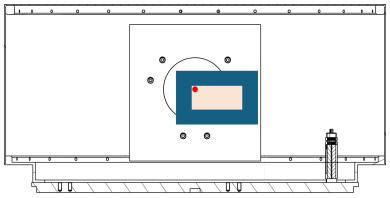

(a) Example initial position of the LVF.

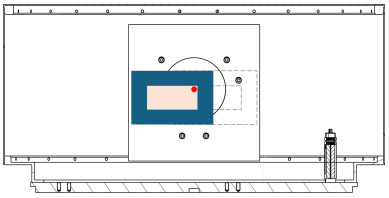

(b) Scan the optical area of the LVF in X-direction (40 mm).

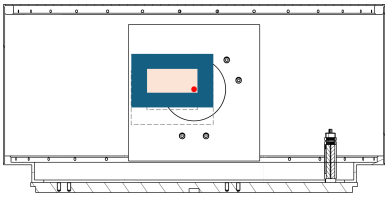

(c) Scan the optical area of the LVF in Y-direction (20 mm).

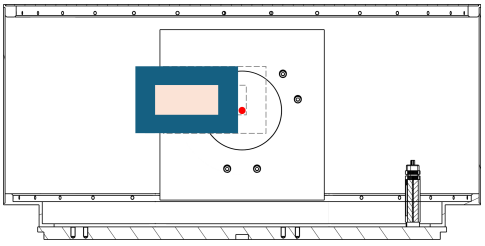

(d) Move the LVF out of the focused beam in X-direction (12.5 mm).

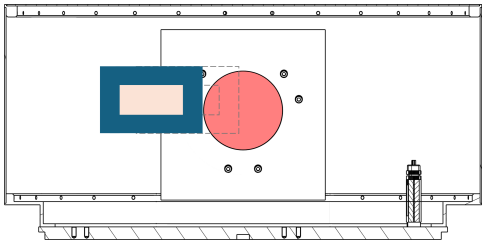

(e) Move the LVF out of the collimated beam in X-direction (25 mm).

Figure 2.3: Range of motion of the LVF displayed within the cryostat.

Step size: 25 µm **Positioning accuracy:** ±5 µm **Metrology:** ±2.5 µm
The full width at half maximum (FWHM) of the focused laser beam is approximately equal to $F \cdot \lambda$, where F is the focal ratio or f-number of the focusing lens and λ is the wavelength. This will later be referred to as spot-size. The beam has a focal ratio of f/20 and the shortest wavelength of light to be used is 25 µm. This leads to the smallest spot-size of the beam being on the order of 500 µm. Experience within SRON says that it is desirable to step the position of the LVF at a factor 20× smaller than the smallest spot-size, leading to steps of 25 µm or smaller. The accuracy of these steps should be a factor 5× smaller, leading to a positioning accuracy of 5 µm or less. Lastly the certainty in position of the LVF (through measurements) should be another 2× better: 2.5 µm or less. To explain the differences further, consider the following example situation: the LVF is at position 0. A step of 25 µm is to be taken. The actual position of the LVF is then allowed to be between 20 and 30 µm. Suppose the motor steps the LVF to 22 µm. The following measurement of the LVF's position must fall between 19.5–24.5 µm.

Time to move out, or back into, the beam: 6 s
The FTS measurements take a minimum of 60 seconds. That means that, the LVF will have to move out of the beam, or back into it, once every 60 seconds. Approximately 90 % of the total time should be spent measuring. That results in a positioning system with a duty cycle $\frac{movement\ time}{measurement\ time + movement\ time}$ of approximately 10 % and a maximum movement time of approximately 6 seconds.

Maximum deviations from perfectly planar XY motion
Piston: 300–500 µm **Tip:** 2–4 arcmin **Tilt:** 2–4 arcmin **Roll:** no specification (–)
These performance metrics are not critical. The depth of focus of the beam is approximately $\lambda \cdot F^2$, which is on the order of 10 mm for the given focal ratio and wavelength of f/20 and 25 µm. Experience within SRON says that it is desirable to be a factor 20 to 40× within the best focus plane, leaving a piston tolerance of 300–500 µm. Secondly, regarding tip and tilt; the f-number of a beam is related to the beam's divergence (half-angle) by $\arctan[1/(2F)]$, which in the paraxial approximation becomes $1/(2F)$. The half-angle of the f/20 beam is therefore 1/40 radians, or 1.4°. The tip and tilt of the LVF should be a factor 20 to 40× better than the half angle of the beam; leading to 2–4 arcminutes. Lastly, roll is not critical. Roll can effectively be seen as an X and Y translation, and as long as the position of the illuminated point on the LVF is known to within the specifications stated before, it is acceptable. Additionally, polarisation considerations do not introduce a roll angle requirement either. The detectors used are polarisation insensitive, and the need to measure the polarisation dependent response of the LVF is not anticipated.

2.1.3. Functional Analysis

Possible setup configurations to scan the laser beam over the LVF are: (a) move the laser source while keeping the cryostat, and the LVF within it, stationary, (b) move the cryostat with the LVF inside while keeping the laser source stationary, (c) move the LVF within the cryostat while keeping the cryostat and the laser source stationary. Diagrams of these different configurations are shown in Figure 2.4. For (a), moving the source and the input- and output optics, near perfectly co-aligned with respect to the LVF within the cryostat is complex and sensitive to small errors. Additionally, it will impede measurement and calibration accuracy as the optical environment is changed between measurements. For (b), it is challenging to move the entire cryostat with 25 µm steps, as well as it being slower in part due to the added dynamics of the 'sloshing' of the cryogenic liquids inside it. Additionally, as in (a), the changing nature of the optical environment will impede measurement and calibration accuracy. Based on experience within SRON option (c) is considered to be the best, easiest, and most versatile.

Design volume: Cylinder of D=300 mm h=140 mm
The LVF positioning system should fit within the existing cryostat, which has an internal diameter of 300 mm and an internal height of 140 mm. An order of magnitude estimation of the maximum allowed workspace-footprint ratio of the positioning system leads to $\frac{workspace\ area}{footprint\ area} = \frac{77.5 \cdot 20}{150 \cdot 140} \approx 0.074$. The workspace area is the ROM of the system, and the footprint area is the area taken up by the system. A large workspace-footprint ratio is desired, as it means that the system uses its footprint efficiently to reach a comparatively large workspace.

Average power dissipation: 10 mW
As the system, and possibly the actuators, will be placed within the cryostat, the amount of power or heat dissipation becomes important. The cryostat's reservoirs are filled with liquid nitrogen and helium

which evaporate in order to cool the working area to 4.2 K. There is a finite amount of energy stored within the cryogens, and the usable time of the cryostat will be reduced by any heat generated within it. A use time of 8 hours (normal working day) is desired. Experience within SRON shows that in order to achieve this, the average dissipation budget should be set at approximately 10 mW. This is based on the latent heat of vaporization of Helium, the available liquid Helium in the reservoir of the cryostat, and thermal parasitics in the cryostat.

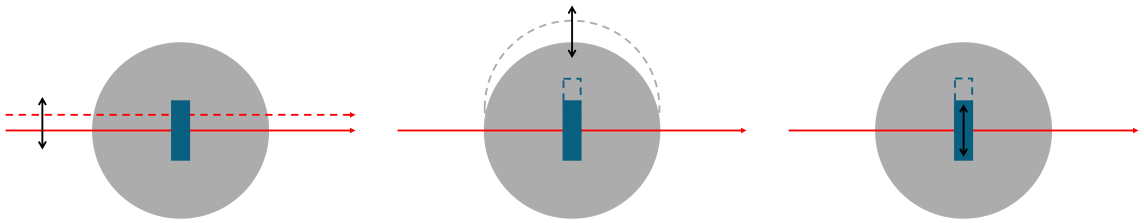

(a) Move the laser source **(b)** Move the cryostat **(c)** Move the LVF

Figure 2.4: Possible setup configurations to achieve scanning of the laser beam over the LVF's optical surface.

2.1.4. Additions

During the course of the thesis, two additional desirable functions emerged. Firstly, the ability to scan an LVF with a larger optical area of 55×25 mm. Secondly, the ability to utilize the system within the BIORAD; the room-temperature FTS optical testing setup. The testing procedure remains identical, where a laser is directed through the LVF and it's surface is scanned, however the geometry of the working area differs. The BIORAD is a rectangular prism with a depth of 229 mm in the direction of the laser beam, a height of 181 mm from floor to ceiling, and a width of 269 mm from side to side. It therefore has a larger height, a slightly reduced width, and a reduced depth compared to the cryostat. Despite the cryostat's larger dimensions, the available space is more constrained due to its rounded structure and the windows that extend into the interior. The most significant difference lies in the optical height: the vertical distance from the floor to the laser beam's focus. This is 10.15 mm larger in the BIORAD. While the system's compatibility with the cryostat is the primary objective, achieving compatibility with the BIORAD is desirable, provided the potentially necessary compromises are deemed to be acceptable.

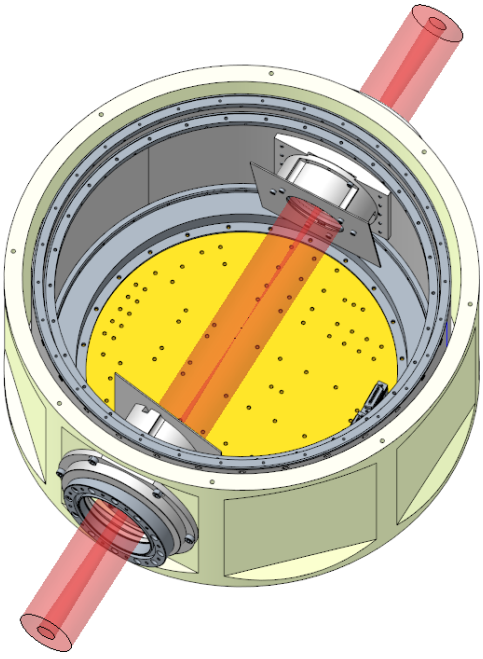

Figure 2.5: The cryostat working area.

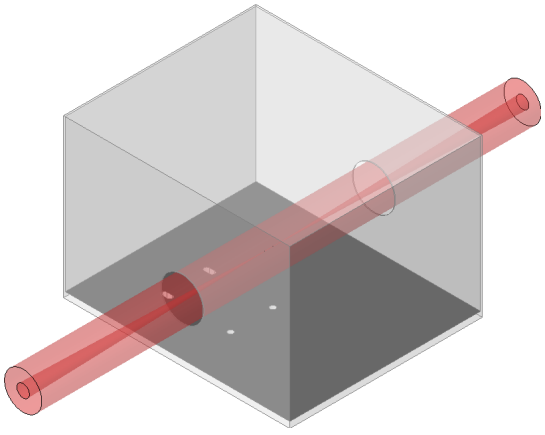

Figure 2.6: The BIORAD working area.

3 Literature Review Summary

A literature review was conducted on cryogenically compatible components (joints and actuators), state-of-the-art cryogenic positioning solutions, and non-cryo literature and mechanism types. The findings are detailed in Appendices A, B, and C; and are summarized in the bullet points below. Additionally, interviews were conducted with key SRON engineers to gain knowledge and learn from the experience that exists within SRON regarding tackling challenges such as the one posed within this thesis. The interviews contained questions on the limitations and advantages of actuators and flexpivots, but focused more on system considerations and broader topics grounded more in expertise and experience.

- Nothing found within industry or literature out-right meets the criteria set in Chapter 2.1.2, meaning a custom solution must be developed.
- Table 3.1 presents a summary of cryogenically compatible actuators and displays their relative performance. Actuation types highlighted in green show potential. Stepper motors show the most potential due to their outstandingly low dissipation (due to their detent torque), commercial-off-the-shelf availability, relatively low-cost, and heritage in comparable cryogenic test configurations.
- Due to the large ROM required and limited available space, monolithic compliant mechanisms are not suitable. Linkage-type mechanisms show the most promise, along with the NOVA-ASTRON perfectly constrained slider.
- The use of compliant joints (such as flexpivots) is preferred over ball bearings or linear guides. As such, it is desirable to limit the range of motion of each joint to a stroke compatible with compliant joints.

Table 3.1: Tabular summary of cryogenically compatible actuators and their relative performance.

		Stroke	Step size & Accuracy	Force	Size	Dissipation	Extras
Linear	Walking piezo	✓	✓	maybe	+ + +	–	+ Stages with built-in linear guides – fragile
	Linear synchronous motor	✓	✓	✓	–	+	
	Voice coil actuator	✓	✓	✓	+ +	+ +	
Rotary	Stepper motor	✓	✓	✓	+	+ + + +	+ Detent torque
	Brushless DC motor	✓	✓	✓	+	+ +	

4 Brainstorming Design Phase

The design process begins with a brainstorm of concepts, which are downselected to three concepts. These three concepts are then assessed more rigorously, resulting in another downselect where the most promising concept is selected for detailing. This concept is refined into a a final design. The trade-off analysis and selection process for the initial brainstorm, and later also of the leftover three concepts, was comprehensive; taking much of the initial project time. This was done to minimize the risk of not considering a concept with high potential, and to avoid the pursuit of a concept that could lead to suboptimal results.

The design process begins by brainstorming different possibilities. An extensive concept generation process was conducted, where initially different actuation and guidance topologies were generated which were capable of producing planar motion. Consequently, for each topology multiple concepts were generated. Some topologies and concepts were easily deemed unsuitable, and will therefore not be presented here. The seven different actuator and joint topologies generated are shown in Figure 4.3. These seven topologies are used to generate approximately 14 concepts, nine of which (1.1, 2.2, 3.1, 3.4, 4.1, 5.1, 5.3, 11.2, 12.1) are deemed to be sufficiently promising to work out further. For each of these nine concepts simple calculations were done to estimate the minimum required lengths of the links, and 1:1 scale paper models were constructed, accompanied by a 1:1 scale paper model of the LVF. These models are then laid on top of a 1:1 print-out of the cryostat's cross-section. This process allows for the development of a general understanding of the spatial constraints imposed by the cryostat, and which concepts are better suited to fitting within the available space. Scans of these 1:1 models can be found in Appendix D, where first the 1:1 model is shown in the cryostat, after which the link length calculations are shown. These nine concepts are evaluated, and the three most promising concepts are selected for further evaluation. While evaluating the concepts, it is important to remember that when in use, the cryostat is turned upside down. Meaning that the cryostat's floor (the copper plate with mounting holes) will actually be on-top. Consequently, in every diagram displayed, the direction of gravity is oriented **upwards**.

Thought was also put into different possibilities to *fold* ROM. For example by rotating the LVF (Figure 4.1) or by using flip-mirrors to redirect the laser beam (Figure 4.2). However these methods were deemed to not provide enough benefit over the complexity they added, and the potential reduction in measurement accuracy they would induce.

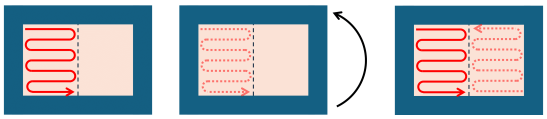

(a) Scan the left half of the LVF. **(b)** Rotate the LVF. **(c)** Once again, scan the left half of the LVF.

Figure 4.1: Folding ROM by rotating the LVF effectively halves the horizontal size of the LVF. The laser only ever has to scan half the width of the LVF.

(a) Scan the left half of the LVF. **(b)** Activate the flipmirror, and once again complete the same scanning motion. Due to the flipmirror this will now scan the right half of the LVF.

Figure 4.2: Folding ROM by using a flipmirror effectively halves the horizontal size of the LVF. The laser only ever has to scan half the width of the LVF. The diagrams show a top-down view. The initial position of the LVF is shown as a dotted rectangle, and the final position is shown as a solid rectangle.

Concepts were assessed based on intuition and experience, without the application of strict weighted criteria. Concepts deemed to have more favourable attributes such as simplicity, potential for high stiffness, no or limited overconstraints, and low dissipation were favored. Conversely, concepts were

negatively ranked if they were deemed to have a high sensitivity to requiring perfect alignment, a high potential for binding issues, long kinematic chains, large moments and forces, or reliance on less desirable components such as ball screws or ball bearings. The final downselect took place during a design review meeting with Martin Eggens.

Concept 3.4 (of which no drawing in present the Appendix) consists of a very simple, direct mounting, of two Onnes piezo stages in series; one on-top of the other. This system excels due to its outstandingly small total size, extraordinary positioning accuracy and small step size, while having built-in (once more extremely accurate) position measurement and feedback control. It is the smallest and most accurate concept. However the concept potentially struggles with actuator fragility, and insufficient actuator force. Onnes is a new company, the technology has little heritage, and the actuators are costly, at approximately 10 to 20 times the price of a Phytron stepper motor. Additionally, the long travel range required for this application, would require a custom-made actuator, further increasing the price. These downsides are deemed to outweigh the accuracy benefits.

Concept 1.1 is direct drive and simple, however has low potential for stiffness, requires ball bearings in the joints, encounters large moments when at the extremes of its workspace, and subsequently also requires high torques from the motors. Additionally, the lower motor has to move and carry the weight of the motor positioned in the elbow, further increasing the expected dissipation. The simplicity of the concept is outweighed by its lacking performance. Furthermore, the concept is similar to concept 2.2, to which it was compared, and deemed inferior to. Therefore this concept was eliminated.

Concept 5.1 was seen as similar to concept 11.2, deemed to be inferior, and was therefore eliminated. It has components positioned far from the floor. The top end of the ballscrew for example must be supported by a ball bearing that is connected to the fixed world. This would require a sizable and stiff frame that reaches all the way to the top of the ballscrew.

Concept 12.1 was considered to be similar, and inferior, to concept 4.1, and was therefore eliminated. The concept possesses large moments, a low potential for stiffness. Additionally the motors are part of the moving mass, resulting in large required forces and diminished dynamic performance.

Concept 5.3 was deemed to be relatively simple and have a relatively high potential for stiffness. However the large joint ranges of motion make ball bearings a necessity. Additionally due to the spatial constraints of the cryostat, the links would be required to be small, resulting in the mechanism reaching close to its singularity positions at the edges of the workspace, resulting in high forces. Furthermore, the links, joints and actuators will likely be larger than drawn, meaning that attaching the links in the optimal position (centrally on the LVF) is likely to be infeasible. The actuator and link on the bottom of the LVF will likely need to attach on the side of the LVF, resulting in a far less desirable configuration and significantly higher forces and moments. As a result of these considerations, this concept was eliminated.

Concept 4.1 was considered to have a large potential for stiffness while still remaining relatively simple. However it is severely overconstrained. Ensuring that the multiple linear guides are sufficiently parallel will be extremely challenging, and that makes this concept very prone to binding issues. Additionally, the forces and moments are large. These large moments could potentially be resolved by dding a second ball screw along the right side of the LVF, turning this concept into an H-Drive. This however adds extra complexity, and adds to the overconstraints within the concept. Due to the extreme overconstraints within the concept, it was eliminated.

The following three concepts (3.1, 11.2, and 2.2) are considered to be the three most suitable concepts and are selected for further evaluation.

Concept 3.1 benefits from putting the largest range of motion in the perfectly constrained slider, where an increase in required range of motion poses no real alterations to the design and requires no concessions to be made. This allows for the Y-stage on top top only be responsible for a much more limited range of motion, allowing for it to be designed as a compliant mechanism. The slider itself is also able to act as the linear guide for the actuator, further increasing the simplicity of the design. The components are positioned near to the floor, which is beneficial for stiffness and thermal performance. The slider provides a very stiff platform for the Y-stage to be mounted on. The largest downside of this concepts is the complexity in the design of the perfectly constrained slider.

Concept 11.2 has its components placed near the floor allowing for simple stiff connections, and is low dissipation due to the use of stepper motors. The concept is simple, and direct drive by two ballscrews, which are in turn also its largest downside. The ballscrews must be aligned to be very parallel, and will require a linear guide along side them.

Concept 2.2 is very simple, direct drive, and low dissipation due to the sue of stepper motors. It has good potential for stiffness, however the into-the-plane stiffness may be lacking. The actuators are places near to the floor of the cryostat's resulting in simple mounting and thermal strapping. Ball bearings will likely be required in the joints. The simplicity of this concept is its greatest advantage.

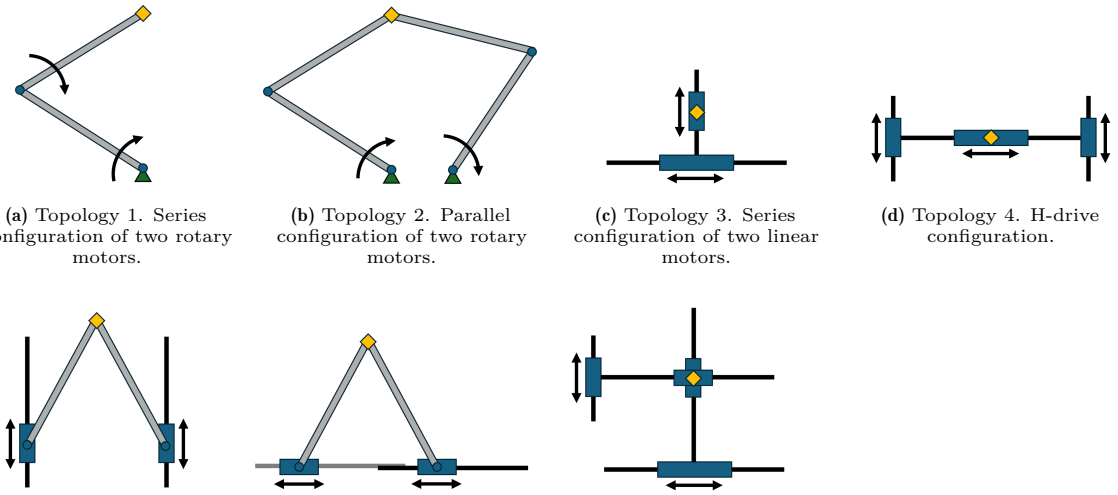

(a) Topology 1. Series configuration of two rotary motors.

(b) Topology 2. Parallel configuration of two rotary motors.

(c) Topology 3. Series configuration of two linear motors.

(d) Topology 4. H-drive configuration.

(e) Topology 5. Parallel configuration of two linear motors. Vertical.

(f) Topology 11. Parallel configuration of two linear motors. Horizontal.

(g) Topology 12. Parallel configuration of two linear motors. XY.

Figure 4.3: The 7 different mechanism topologies.

5 Conceptual Design Phase

After the downselect in the previous chapter, there are are three remaining concepts: 3.1 (Slider), 11.2 (TT, due to the two translation actuators), 2.2 (RR, due to the two translation actuators). To further be able to differentiate between these three concepts, and ultimately be able to chose the most promising one, further analysis is required. In this chapter, preliminary MATLAB models are developed for each concept, and more thorough analysis of their characteristics are made.

5.1. Slider

The slider concept consists of a NOVA-ASTRON perfectly constrained slider that provides the ROM in X-direction. On top of the slider is a serially mounted Y-stage, for which there are two variations. The first option (shown in Figure 5.1) is a Y-stage that consists of a parallelogram of rigid links, where each joint is a flexpivot, and the base of one link is driven by a stepper motor or brushless-DC (BLDC) motor; where a stepper motor would be preferred due to the lower dissipation. In the second variation (Figure 5.2c), the Y-stage could consist of a parallel leaf spring stage (detailed in Figure A.5b) actuated by a voice-coil-actuator (VCA). Each figure includes an approximately true-to-scale depiction of what the Y-stage actuator would look like. Approximate dimensions for the actuators were taken from Phytron for the stepper motors [8] and from ThorLabs for the VCA [9]. In the case of each variation, the slider would move all the way to the left to move the LVF out-of-the-beam (OOB).

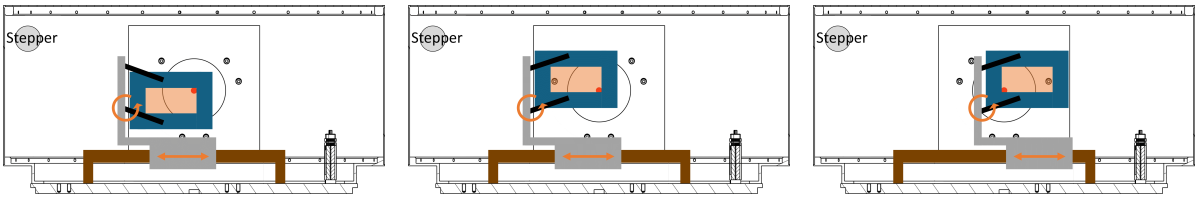

(a) LVF in the low-left position.

(b) LVF in the high-left position, showing the motion and working of the Y-stage.

(c) LVF in the high-right position, showing the motion and working of the X-stage.

Figure 5.1: Y-stage consisting of a parallelogram of rigid links with flexpivots in the joints, and driven by a stepper motor.

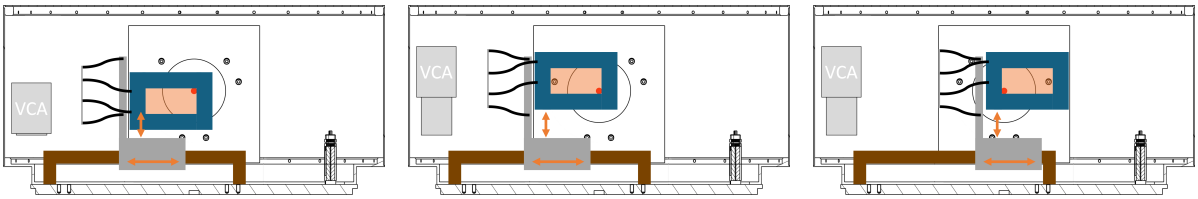

(a) LVF in the low-left position.

(b) LVF in the high-left position, showing the motion and working of the Y-stage.

(c) LVF in the high-right position, showing the motion and working of the X-stage.

Figure 5.2: Y-stage consisting of a parallel leaf spring stage, and driven by a VCA.

5.1.1. Y-Stage Comparison

Both the flexpivot stage and leaf spring stage are similar, but also have key differences. In the paragraphs below, they will be compared with respect to different key performance characteristics.

5.1.1.1. Arm Length

Both stages require some arm length in order to function. They must be able to provide 20 mm of stroke in Y direction, which can be split into +10 mm and −10 mm from the neutral position.

As stated in Appendix A.3, a rule-of-thumb for the maximum angular stroke of a loaded flexpivot from C-Flex, is ±10°. Knowing the required range of motion and the maximum angle of the joints, the shortest required arm length for the flexpivot stage is given by $L = \frac{10}{\sin(10°)} \approx 57.6\,\text{mm}$. Next, the shortest arm length required for the leaf spring stage can be calculated using the approximation derived in Chapter A.3 ($L \approx 12.5\sqrt{\delta_{max}}$) which yields a length of approximately 39.5 mm. It can thus be concluded that the leaf spring stage is more compact than the flexpivot stage (as 39.5 mm is less than 57.6 mm).

Unlike is possible for the flexpivot arms, the leaf springs can not connect around the top and bottom of the LVF in order to save on space. This is because of the vertical support bar, as shown in Figure 5.2 in grey. The point where the leaf springs attach to the LVF, is at the same X-coordinate as this vertical support bar. Therefore, moving the arm-LVF attachment point to the right on the LVF in order to save space, would soon result in optical obstruction, as that vertical support bar would find itself behind or in front of the optical area of the LVF.

In the OOB position, the LVF, and any part of the mechanism, must fit within the area between the sidewall of the cryostat and the window. Knowing the diameter of the cryostat (300 mm) and the diameter of the window (25 mm), leads to knowing that there is 137.5 mm of space budget left to fit the the entire width of the LVF (65 mm) and the Y-stage. As shown in Figure 5.1, the arms of the flexpivot stage do not stick out, and do not take up much extra space; therefore this space budget is ample. The arms of the leaf spring stage however do have to stick out, resulting in the total width being equal to $arm\ length + LVF\ width = 104.5\,\text{mm}$. 104.5 is less than 137.5, therefore it can be concluded that this stage would fit within the cryostat (leaving 33 mm of leftover space), as the total width is less than the available space budget,.

One drawback of the flexpivot stage is that its motion is not in a straight line, but in an arc. This means there is some cross axis coupling between the X and Y motion. However this is not very problematic, since the path of this arc is very well characterisable. The leaf spring stage is capable of straight line motion.

5.1.1.2. Stiffness

The stiffness a stage is able to provide is supporting directions (forces in X and Z, and moments around X, Y, and Z) is an important consideration. Due to it's rigid links, the flexpivot stage is able to provide a higher supporting stiffness than leaf spring stage. Leaf spring stages are susceptible to moments and off-axis forces (especially at their deflection extremes). Forces in the Z-direction, moments around the X- and Y-axis could cause the leaf flexures to twist or buckle. Additionally, when in the deflected position and bent into their s-shape the leaf flexures lose a lot of stiffness against forces in the X-direction and moments around the Z-axis. These kinds of forces are present, and considerable, due to the fact that the LVF is hanging off the side of the stage, constantly applying a moment around the Z-axis. It is desirable to mount one leaf spring stage on each side of the LVF in order to counteract these lacking stiffnesses with respect to the LVF twisting around the X-axis direction and "falling into the page". However this does not fit within the OOB space budget available. It would require the space for another arm length (39.5 mm) while there is only 33 mm of budget left. This leaves increasing the length of the leaf spring's into-the-page dimension as the only option for increasing the supporting stiffness of the leaf spring stage.

5.1.1.3. Actuators

For the leaf spring stage, ideally the VCA would be positioned in the same Z-plane as the leaf-springs, and near directly below the center of mass of the LVF in X-direction. However it is clear that there is insufficient space to fit the actuator there. This means that the VCA has to be connected at a different Z-depth, which would create a moment around the X-axis, for which the leaf springs of the stage are susceptible to twisting. Due to the fact that it would optically obstruct the path of the laser through the LVF, the VCA would also have to connect at an X-location different than its optimal positioning, which would result in an undesirable moment around the Z-axis acting on the leaf spring stage.

The positioning of the stepper motor in the flexpivot stage is not problematic. What is undesirable, is that the actuator is positioned at the end of a lever arm. This increases the torque required from the actuator, and decreases its maximum allowable angular step size. The longer the arm, the smaller the angular steps are that the motor must be able to make to reach the 25 µm step-size requirement, and additionally the larger the moment arm is from actuator to the center of gravity of the LVF.

A simple sine relationship calculates the required motor angular step size: $motor\ angular\ step = \sin^{-1}\left(\frac{LVF\ y\ step\ size}{L}\right) = \sin^{-1}\left(\frac{25\times10^{-3}}{57.6}\right) = 0.025°$. Phyron's VSS stepper motors takes steps of 1.8°, meaning that a gearbox would be required reach the step size requirement while still being able to utilize the detent torque of the stepper motor. This is a drawback as gearboxes add losses, backlash, and an extra point of potential failure. A gearbox with a ratio of $\frac{1.8}{0.025} \approx 72$ would be required.

Next, regarding the torque requirement of the motor, the arms of the mechanism are able to attach above and below the center of mass of the LVF, resulting in a lever-arm equal to the length of the arms (57.6 mm). The LVF weighs approximately 60 g resulting in a torque requirement of approximately 34 Nmm. Deforming three flexpivots to their maximum angle requires a very small torque from the motor of approximately 1 Nmm. Due to the already required gearbox with ratio of 72, the total torque requirement for the stepper motor gets reduced by the same factor, bringing it down to $\frac{35}{72} \approx 0.45$ Nmm, for which the detent torque of the smallest Phytron VSS stepper motor (0.9 Nmm) [8] is already sufficient. Additionally, the LVF can be gravity balanced, in theory by simply applying a constant force spring to it that is tuned to the mass of the LVF, in which case the required torque to move the LVF would approach zero.

5.1.1.4. Conclusion

Due to the lower dissipation aided by of the use of a stepper motor with detent torque, smaller actuator and easier actuator mounting, fewer problems with optical obstruction, higher stiffness, and superior compactness due to the possibility of mounting the arms around the top and bottom of the LVF, the flexpivot stage is preferred over the leaf spring stage.

5.1.2. Slider Considerations

The slider can be actuated by any linear actuator, for example a, stepper motor and ballscrew or VCA. The slider itself acts as the linear guide, so no extra linear guide mechanism needs to be incorporated. Once again, a stepper motor is preferred due to its low dissipation, however it comes with similar downsides as the ballscrew stage mentioned in Appendix B.2: a need for intentional slack in the system or a high degree of parallelism between the slider and the ballscrew, and an increased chance of wear and tear and binding issues. These downsides are however still preferred over a constantly dissipating actuator.

The only force required from the actuator, if losses to friction in the bearings are neglected, is the force required so accelerate the slider. Given that $a = \frac{2s}{t^2}$ and the fact that in the worst case scenario the stage would have to move the entire X ROM (77.5 mm) in 10 s. The stage would need to accelerate for half the distance, and decelerate for the other half of the distance. This results in $a = \frac{2\cdot0.5\cdot ROM\ x}{(0.5\cdot time\ to\ change\ pos)^2} = \frac{2\cdot0.5\cdot77.5}{(0.5\cdot10)^2} = 3.1\,\mathrm{mm/s^2}$. Making a rough order of magnitude estimate for the total moving mass being 1 kg results in a required slider actuator force of 3.1 mN, which is very small.

Lastly, in regards to the dimensioning of the slider, the wider the mover is, the higher its stiffness to rotation around the Z-axis. This is desired as the weight of the LVF is potentially off-center. A wider mover results in a larger total length of the slider, as the total length of the slider is determined by the sum of the X ROM and the width of the mover. However a sufficiently wide mover should be possible to fit within the cryostat, even if the slider as a whole is a comparatively bulky concept.

5.1.3. Overview

Benefits of the slider concept as a whole are that the dimensioning of both the Y-stage and the slider are trivial, and this would allow for quickly moving on to the designing and manufacturing stages. The slider also provides a perfectly constrained, and stiff base that takes care of the largest ROM stroke. This provides a solid foundation for the Y-stage which is positioned on top of it. There is also very little cross-axis coupling, which results in very easy to control kinematics. Lastly, the uncertainty in the

measurement of the position of the LVF can be very low. The slider itself is perfectly constrained, and the Y-stage on-top consists of compliant joints, and as a result, accurately measuring the position of the slider and the angle of the link in the flexpivot stage would result in a measurement of the position of the LVF with a high degree of certainty as there is very little uncertainty in the chain from slider, through the Y-stage, to the LVF. The sliders downsides are its size, abundance of parts and interfaces, and lack of direct-drive, likely resulting in a complex design process and a laborious assembly process. Out of the three concepts, the design of the slider concept is deemed to be the most complex.

5.2. TT

The TT concept consists of two stepper motor driven ballscrews separated from each other in the Z-direction. Stepper motors are once again preferred due to their low dissipation. A gearbox on the stepper motors will not be necessary as the ballscrew itself already acts to create mechanical advantage. These ballscrews each drive a stage or ballnut which connect to the LVF through rigid links with flexpivots in the joints. Moving these ballnuts in sync will result in X-motion of the LVF, and moving them in opposite directions will result in Y-motion of the LVF. A parallelogram is required to constrain the rotation of the LVF. Depictions of this motion are shown in Figure 5.3, including a true-to-scale representation of the stepper motors that would drive the ballscrews. Furthermore, as will be introduced later in this section, the crossed-mode of the mechanism is shown in Figure 5.4.

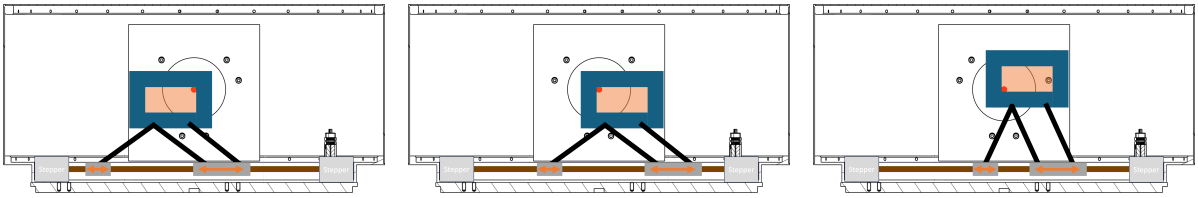

(a) LVF in the low-left position.

(b) LVF in the low-right position, showing that moving the ballnuts in sync changes the X-position of the LVF.

(c) LVF in the high-right position, showing that moving the ballnuts in opposite directions changes the Y-position of the LVF.

Figure 5.3: Overview of the TT concept, consisting of two separate ballscrews driving a ballnut.

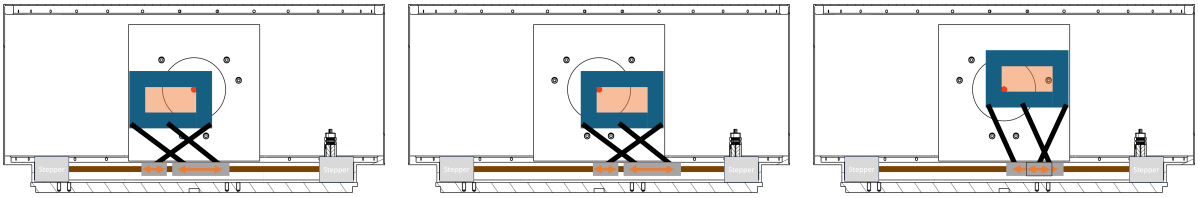

(a) LVF in the low-left position.

(b) LVF in the low-right position.

(c) LVF in the high-right position.

Figure 5.4: The TT concept in crossed mode. The crossed mode is kinematically identical to the wide mode.

5.2.1. Parallelogram

As shown in Figure 5.5, the parallelogram is necessary because the two links can lay anywhere on their respective circles, and as such, the rotation of the LVF is not constrained. If the ballnuts move towards each other, then there are compressive forces within the mechanism, the mechanism will want to buckle and fold in on itself, and the LVF will no longer be horizontal. Technically speaking, the use of flexpivots means that the use of a parallelogram is not strictly necessary. The system 'wants' to be at a position of equilibrium at the lowest potential energy, and for the flexpivots that means all of them equally and minimally flexed. The system will therefore aim to be in a symmetrically deformed state, resulting in a horizontally oriented LVF. However, this only works in an ideal world. It is unreliable to depend on the reproducibility of the torque generated by the flexpivots due to hysteresis in the material and variation in stiffness at large angles. So the angle of the LVF should be mechanically constrained, and this can be achieved through the use of a parallelogram.

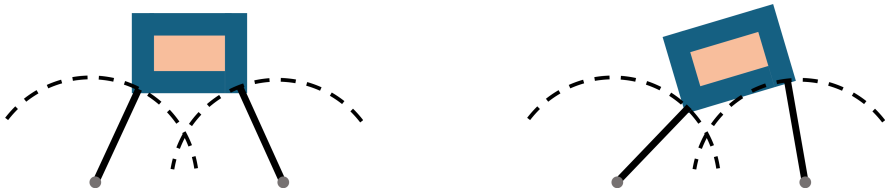

Figure 5.5: Without a parallelogram the rotation of the LVF is not constrained. For a given position of both ballnuts, the links can still find themselves anywhere on their respective circles.

5.2.2. Equations

5.2.2.1. Link Length and Angle

When dimensioning the links, their length (L) is an important dimension, however the minimum angle (α) of the links is as well. The angle of the link is defined with respect to the positive Y-axis. If a link of a given length starts in a vertical position, it will have to cover a comparatively large angular stroke to achieve 20 mm of change in the Y-coordinate of its tip. If the same link starts in a horizontal position, that required angular range of motion to achieve 20 mm of Y-ROM will be much less. Therefore, with respect to efficiency in achieving the required Y-ROM, it is desirable for the links to be near horizontal. This however would require an infinite amount of force to reach. With respect to force efficiency, vertical links are the most effective. Vertical links also reduce the total width of the mechanism, or how far the legs stick out form under the LVF.

The length of the links also impacts how easily the required Y-ROM can be achieved. Longer links cover more distance for a given angular stroke, and therefore can afford to be positioned at a minimum angle that is closer to vertical, and therefore more beneficial in terms of required force and wideness. Since the joints of the links are flexpivots, their angular stroke is limited to the rule-of-thumb of 20° total. The following relationship (accompanied by Figure 5.6) relates minimum link angle to link length.

$$L\cos(\alpha) - ROM_y = L\cos(\alpha + flexrom)$$

Where $flexrom$ is 20° and ROM_y is 20 mm. This relationship calculates, for a given link length, the closest to vertical it can be placed while still being able to achieve the required 20 mm of Y-ROM within 20° of joint flexion. Increasing arm length results in a reduction of the minimum angle, thereby reducing the required force and wideness. Not every length of link is suitable, as the length can be too short to be able to generate 20 mm of Y-ROM over 20° of angular stroke, even with an initial angle near 90°. A result of this method of dimensioning is that the attachment point of the arms to the LVF is not chosen, but enforced by the minimum angle.

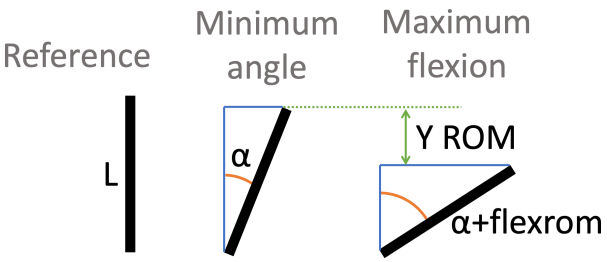

Figure 5.6: The derivation of the relationship between minimum angle and link length.

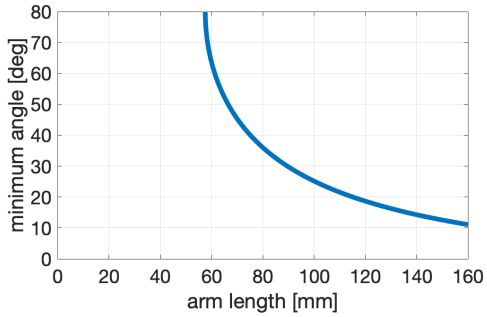

Figure 5.7: The plot of minimum angle versus arm length.

5.2.2.2. Ballscrew Pitch

Stepping the LVF in increments of 25 µm is required. The stepper motor takes angular steps of 1.8°, leading to 200 steps per revolution. A ballscrew's pitch is the mm of ballnut travel per full revolution of the ballscrew. Calculating the pitch (p) required to step the LVF in sufficiently small increments is done as follows. In X-direction it is simply $p = 25 \cdot 10^{-3} \cdot 200$. For LVF steps in Y-direction, the closer the arms are to horizontal, the more sensitive the Y motion of the LVF is with respect to the angular steps of the stepper motor. Therefore the pitch requirement must be set at the most sensitive point; the maximum angle. The required pitch is calculated as $p = \frac{25 \cdot 10^{-3}}{\tan(\alpha + 20°)} \cdot 200$.

5.2.2.3. Actuator Torque

The force required from the stepper motors is also maximum at the point of maximum angle. The maximum total force required (in N) is equal to the force required to flex the flexpivots, and the force required to support the weight of the LVF through the nonlinearity created by the angle of the link: $F_{total\ max} = LVF_{total\ mass} \cdot 9.81 \cdot \tan(\alpha + 20°) + 6 \cdot \frac{torsional\ spring\ rate \cdot 20°/2}{L \cdot \cos(\alpha + 20°)}$. This total force is divided equally over the two stepper motors. This force is translated to a motor torque (in Nmm) requirement as follows: $\tau_{max} = \frac{0.5 \cdot F_{total\ max} \cdot p}{2\pi}$ [10] [11]. The total mass of the LVF and mounting hardware is assumed to be 160 g. The assumed torsional spring rate is 0.0339 Nmm/degree [12].

5.2.3. Dimensioning

As shown in Figure 5.7, the minimum possible link length (that results in a final total angle of almost 90°) is 59. This however results in a ballscrew with a pitch of 0.22, which is too small and not available for purchase. The smallest link length that is viable, as limited by the requirement of having a pitch greater than or equal to 1, is 62 mm. It has acceptable motor torque of 0.65 Nmm. Through trial-and-error it was found that a link length of approximately 68 mm is the upper limit. Longer links result in unavoidable optical obstruction of the window in the OOB position. Link lengths of 68 mm have a smaller minimum angle, and therefore stick out less and are less wide than links of 62 mm. However they are still unacceptably wide. Figure 5.8a shows that in the OOB position the end of the link and the ball nut come unacceptably close to the sidewall of the cryostat. Therefore it can be concluded that there is not a single link length for this concept which is capable of fitting within the cryostat.

There is however a possible solution: crossed mode. Kinematically identical to the configuration shown before, simply mirroring each link around the Y-axis drastically reduces the wideness of the mechanism, as shown when comparing Figure 5.8a to 5.8b. Arm lengths of up to 75 mm are now possible before optical obstruction once more becomes an issue. This allows for reduced force and relaxed ballscrew pitch requirement. The downside of this crossed configuration however is drastically reduced stiffness. A system in the crossed mode would be less resistant to forces in X-direction and moments around the Z-axis as there is an instant center of rotation at the point where the links cross.

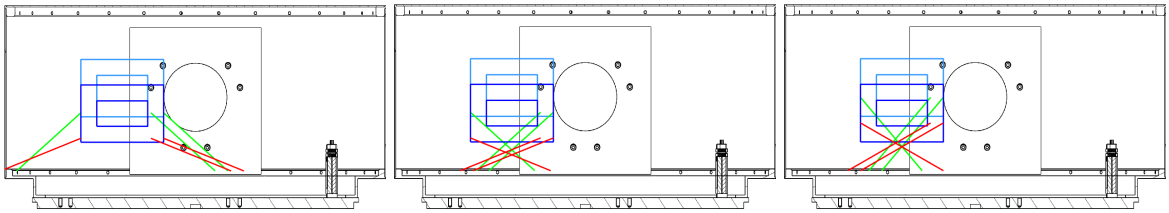

(a) Wide mode with 68 mm long links. Showing that the mechanism is unacceptably wide.

(b) Crossed mode with 68 mm long links. Showing that in crossed mode, the mechanism is no longer unacceptably wide.

(c) Crossed mode with 75 mm long links. Showing that longer links wold begin to cause optical obstruction.

Figure 5.8: Depictions of the TT mechanism within the cryostat in the OOB position.

5.2.4. Torsional Constraint

Imagine the ballnut and arms are connected to the ball screw, but not connected to the LVF. When the stepper motor actuates the ballscrew, the ballnuts and arms will simply spin around in place. A constraint on the rotation of the ballnut around the spindle is required in order to produce linear motion. Now imagine the arms are connected to the LVF. If the ballscrews are actuated in opposite directions (in order to raise or lower the LVF) this torsional constraint can be provided for by the opposing moments of the two ballscrews; through the kinematic chain from one ballscrew, through the LVF, to the other ballscrew. In this case it is the LVF and its bracket that absorb the torsional load; they must therefore also be sufficiently stiff. However, if the spindles are actuated in the same direction, there are no opposing moments, and therefore also no torsional constraint. As a result, the ballnuts, arms, and LVF would, just like before, simply spin around in place. Additional components are required to provide this torsional constraint on both ballnuts.

This torsional constraint could be provided for by a pin with a bearing running through a slot along the length of the spindle. This would induce some rotational backlash. However, the ballscrew itself should only act to provide the driving force, and ideally not be relied on for constraints and linear guidance properties. Therefore, some sort of linear guidance is still required. This requirement essentially turns this concept into two ballscrew stages side by side: and as is mentioned in Appendix B, ballscrew stages are overconstrained (requiring near perfect alignment of the many linear guides, or requiring intentional slack where necessary) and very susceptible to wear, tear, and binding issues within a cryogenic environment. The simplicity which this concept seemed to have quickly vanishes, and it turns into an overconstrained, and complex design, with necessary extras to solve some of its shortcomings (like the requirement of separate linear guidance, or at least a torsional constraint for the ballnuts).

A less serious, but still notable issue, arises from the fact that the ballscrews are in different Z-planes, which causes a moment around the Y-axis when the LVF is actuated. This torsional moment is transmitted to the joints, which must be strong enough to support the load.

5.2.5. Measurement

The most attractive characteristic of the concept is the fact that its measurement uncertainty has the potential the be very small. To measure the position of the LVF, the positions of the ballnuts must be known. In the kinetic chain from ballnut to LVF there is very little uncertainty as the arms are rigid and the joints joints are compliant. The largest uncertainty is created by the backlash of the ballscrew. However any linear backlash in the ballscrew can be made irrelevant by applying a separate measurement instrument for the position of the ballnuts. This would result in very precise knowledge of the position of the ballnuts, and consequently also of the LVF.

5.2.6. Overview

In conclusion, it is necessary to position the links in the crossed mode, which reduces the stiffness of the system. Furthermore, and most importantly, the system essentially consists of two ballscrew stages, of which the shortcomings are known and deemed to be too severe, and only acceptable if offset by great benefits. The redeeming qualities of this concept are low dissipation due to its use of stepper motors, and its potential for low measurement uncertainty. However, in terms of both performance metrics, the Slider concept performs at least equally as good and poses less fundamental downsides in its kinematics. The slider is perfectly constrained (as opposed to the overconstrained nature of the TT ballscrew stages) and also consists of two stepper motors. Therefore, between the TT and the Slider concepts, it is the Slider which is preferred.

5.3. RR

The RR concept consists of a 5-bar mechanism which is driven by two stepper motors. As before, stepper motors are preferred due to their low dissipation. A gearbox will be necessary to reach the required LVF step size. A 5-bar mechanism does not constrain the rotation of the LVF around the z-axis, therefore the left arm of mechanism is “copied” over to the right to create a parallelogram whereby this LVF rotation is constrained. The concept is similar to what is shown in [13], which is discussed in Appendix C.5. Depictions of the motion of the arms of the 5-bar mechanism and the parallelogram, as well as a true-to-scale representation of the size of the stepper motor, is show in Figure 5.9.

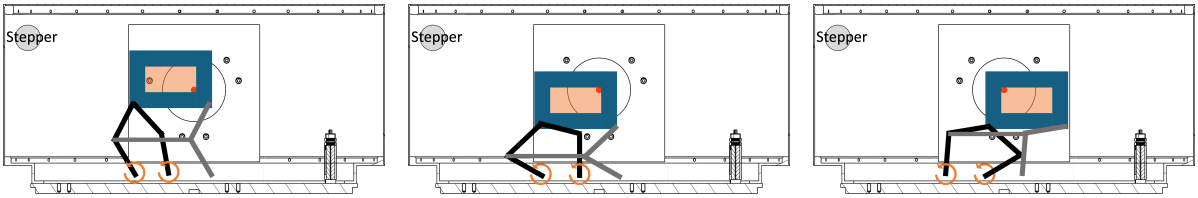

(a) LVF in the high-left position. **(b)** LVF in the low-left position. **(c)** LVF in the low-right position.

Figure 5.9: Overview of the RR concept, consisting of a 5-bar-mechanism driven by two stepper motors, and a parallelogram to constrain the rotation of the LVF.

5.3.1. Operating Modes

A 5-bar mechanism has different operating modes, as shown in Figure 5.10. The first step is considering which mode is most suitable for this application. The $+-$ working mode is clearly inferior to the others due to its limited workspace, and the $++$ mode is the mirror image of the $--$ mode. Therefore only the $--$ and $-+$ modes will be considered. The reachable workspaces shown, are deceiving. They allow the lower arm to go past horizontal, which in the case of the mechanism in the cryostat, is not possible, as the lower arm would crash into the floor of the cryostat. The pink dashed lines represent the true workspace each mode could reach in the cryostat. The $-+$ mode is preferred over the $--$ mode due to its perceived ability to inscribe a larger rectangle. A consideration must also be made for whether or not the link lengths will be made symmetric, meaning that both under arms are the same length, and both upper arms are the same length. The workspace the mechanism must be able to reach is a rectangle centered around the middle of the mechanism. Non-symmetric link lengths, and the non-symmetric reachable workspace they create, therefore pose no real benefit. The simplicity gained in designing, manufacturing and assembly are considered more valuable. Keeping the links symmetric reduces the design variables from 5 to 3, and therefore drastically reduces the number of combinations possible.

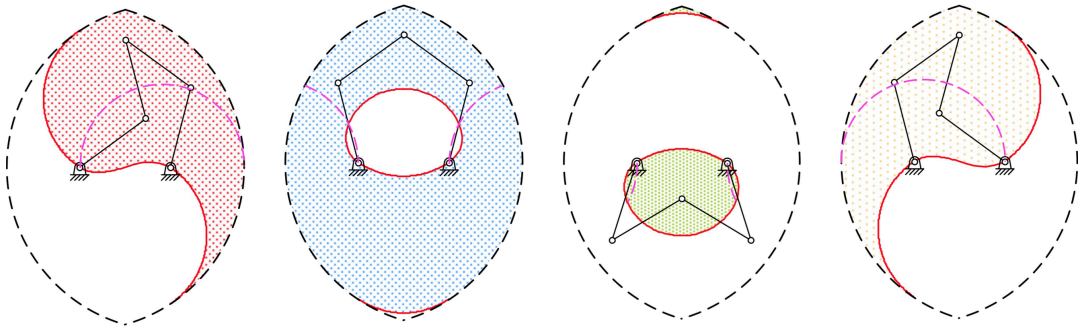

(a) working mode $++$ (b) working mode $-+$ (c) working mode $+-$ (d) working mode $--$

Figure 5.10: The four different modes of a 5-bar mechanism and the workspaces they can reach. Adapted from [14]

5.3.2. Dimensioning

The dimensioning of the lengths of the links of the 5-bar mechanism is complex, and requires an optimization routine. Three degrees of design freedom (L_a, L_b, L_c) influence various performance metrics (motor step-size requirement, motor torque requirement, workspace size, joint flexion ROM) in nonlinear and opposing ways. For example, longer links result in lower joint flexion ROM but may not fit within the cryostat.

While the design space is too large and complex to search through manually, some focused trial-and-error still aids in gaining a preliminary understanding of the capabilities of the concept. The tools used during this search through the design space are outlined in Chapter 6. An example of a plot of a link length combination, and one of its performance metrics, is shown in Figure 5.11. These types of plots are used to evaluate different link length combinations, and iterate through the design space to gain understanding of it. The most consequential discovery made during this preliminary search through the design space is that the required range of motion of the joints is likely too high to be able to use flexpivots. The best case scenario may be that a large portion of the total joint angular range

of motion can be assigned to the LVF attachment joint, leaving the elbow joint with a comparatively small flexion range, allowing for the application of flexpivots. However it is possible (and possibly more likely) that not a single joint is able to employ flexpivots, and that every joint must consist of ball bearings. Furthermore it was discovered that motor torque and angular step-size are likely to be easily achievable with the available VSS stepper motors and gearboxes from Phytron. It is also likely that the arms of the 5-bar mechanism will have to attach higher up on the LVF than shown in Figure 5.9. This may result in the arms passing behind or in-front of the optical area of the LVF, resulting in optical obstruction becoming a challenge to work around.

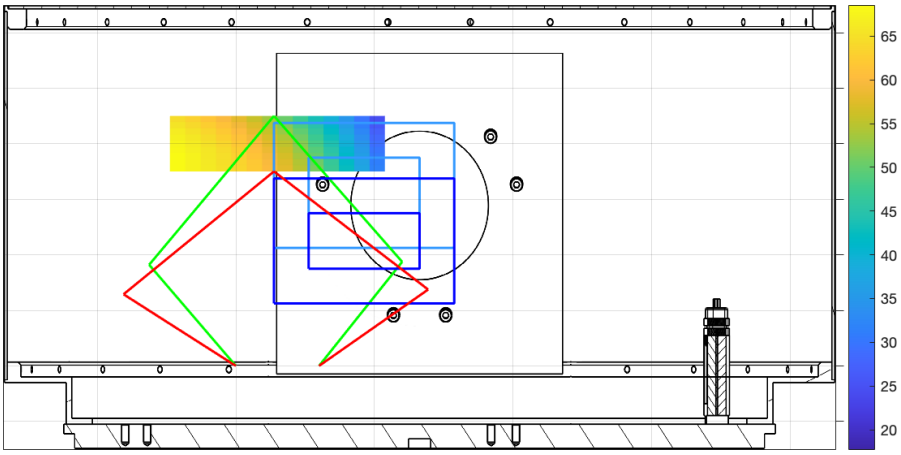

Figure 5.11: A representation of an example 5 bar mechanism. In this case $L_a = 48$, $L_b = 70$, and $L_c = 30$. The mechanism is presented within a cross-section view of the cryostat. The heatplot shows the torque required from the left stepper motor to bring the LVF to that position in the workspace.

5.3.3. Overview

The RR concept is the most simple of the three concepts. It is directly driven by the two stepper motors, and there is no need for extra linear guides or extra complexity that is not shown within Figure 5.9. It is also almost perfectly constrained. As shown in [13], overconstraints come from the joints and the horizontal link connecting the left arm to the parallelogram arm. These overconstraints can be relieved as shown in [13]. Alternatively, the choice can be made to not relive these overconstraints, and rely on a high degree of parallelism between the centerlines of the joint holes to ensure that the overconstraints do not cause significant issues. Additionally, the torque requirements are expected to be low, and easily achievable with the available actuators from Phytron. A downside of the RR is that the dimensioning of the lengths of the links is complex, and required an optimization routine. Additionally, similar to the TT concept, this RR concept struggles with limited stiffnesses with respect to the LVF twisting around the X-axis direction and “falling into the page”. Lastly, the employment of flexpivots is unlikely to be feasible.

5.4. Downselect

As stated earlier, the Slider is preferred over the TT due to its superior kinematics, perfect constraint, and equal performance in terms of low dissipation and measurement uncertainty, while posing fewer fundamental downsides. Thus this final evaluation only takes place between the Slider and the RR. Both concepts perform equally well in terms of dissipation. The Slider’s main benefits over the RR are its higher stiffness, fewer overconstraints, and its ability to avoid ball bearings. If RR were able to employ flexpivots in all of its joints, it would clearly stand out as the most preferred concept due to its great level of simplicity. The question then becomes: is the reduction in accuracy created by the required use of ball bearings worth the increase in simplicity. This is challenging to answer based on mathematics and modelling alone, and required some insight, judgement and experience. Ultimately the increase in simplicity was considered to be more valuable than the reduction in position metrology accuracy. The RR concept is therefore considered to be the most suitable and will be developed further into a manufacturing ready design.

6 Preliminary Design Phase

6.1. MATLAB Model

Due to the complexity of the dimensioning of the link lengths of the RR mechanism, a MATLAB model was used to evaluate the performance of different combinations of link lengths to ultimately be able to reach a conclusion on which link lengths are optimal. There are three design degrees of freedom (L_a, L_b, L_c) and a combination of L_a, L_b, L_c will be referred to as a *triplet*. There are 10 performance metrics or constraints which are calculated for a given triplet: inequalities 1, 2, 3, and 4, required elbow joint flexion ROM, required LVF joint flexion ROM, required motor torque, required motor angular step size, max joint radial load, and optical obstruction distance. Some of these performance metrics or constraints are functions only of the link lengths, and some are also a function of the position of the end-effector (EE) within the workspace (WS) of the mechanism.

Figure 6.1b shows the symmetric 5-bar mechanism with its singularity curves. If link A of the left arm is horizontal, then as the right arm is actuated, the EE will trace the path of the circle with its center at $(-L_a, 0)$ and with radius L_b. The same will happen if link A of the right arm is kept horizontal. The two larger circles have a radius of $L_a + L_b$, and have their origins at the base of their respective arms. These circles show the maximum reach of each individual arm. The bottom blue singularity curve shows the path traced by the EE if the B-links of both arms are co-linear. This position takes infinite force to reach. This bottom singularity curve does not exist if the two smaller circles of radius L_b are large enough to intersect with each other. These curves (the red circles and the blue curve) mark the reachable WS of the mechanism, highlighted in green. The bottom blue singularity curve is calculated as a parametric curve using the following equations, simplified from [15], where C_x and C_y are the X and Y coordinates of the parametric curve which is a function of the parametric variable θ_1.

$$L_1 = L_a \qquad L_2 = 2L_b \qquad L_3 = L_a \qquad L_4 = L_c \qquad L_p = L_b$$

$$K_1 = \frac{L_4}{L_1} \qquad K_4 = \frac{L_4}{L_2} \qquad K_5 = \frac{L_3^2 - L_4^2 - L_1^2 - L_2^2}{2L_1L_2}$$

$$B = -2\sin(\theta_1) \qquad A = \cos(\theta_1) - K_1 + K_4\cos(\theta_1) + K_5$$

$$C = K_1 + (K_4 - 1)\cos(\theta_1) + K_5$$

$$\theta_2 = 2\tan^{-1}\left(\frac{-B - \sqrt{B^2 - 4AC}}{2A}\right)$$

$$C_x = L_1\cos(\theta_1) + L_p\cos(\theta_2) \qquad C_y = L_1\sin(\theta_1) + L_p\sin(\theta_2)$$

Figure 6.1b shows that for triplets where the reachable area is large enough, there is freedom in the positioning of the WS within that reachable area of the mechanism. The margined WS can be shifted up or down while still being within the green shaded area. The possible positions of the margined WS are contained within the possible WS. The choice was made to always position the WS centered and symmetrical within the green area. The X-position of the WS will always be centered around the $L_c/2$ line, and the Y-position will be positioned as to have equal spacing between the red circles on the top and bottom of the margined WS. There is however no freedom in the positioning of the LVF; the area over which it moves must always be positioned over the laser beam. This can lead to a situation as shown in Figure 6.2, where the WS of the arms is positioned at a different height than where the LVF must be. This offset can be accounted for by introducing struts that are rigidly attached to the LVF, which bridge the gap and connect to the arms of the mechanism.

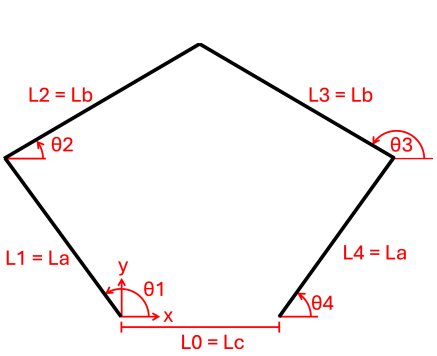

(a) The lengths and angles of the RR mechanism.

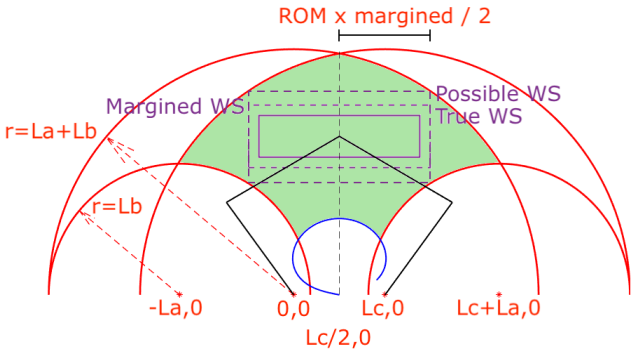

(b) The red and blue singularity curves showing the different workspaces of the mechanism. The true WS drawn with the solid line, the margined WS is larger than the true WS by some margin around each edge, and the possible WS has the same width as the margined WS, but is made to be as tall as possible.

Figure 6.1: Conventions used for the mechanism.

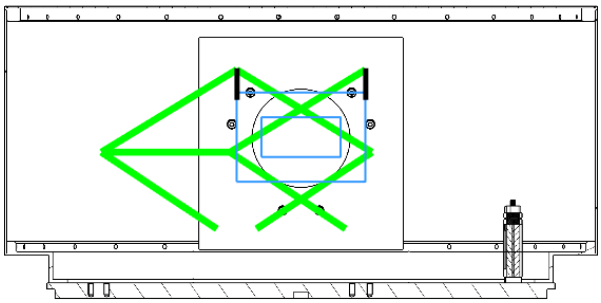

Figure 6.2: It is possible for the WS of the arms to be at a different height than where the LVF must be positioned. This offset is accounted for by introducing struts which bridge the gap.

6.1.1. Inequalities and Initial Filtering

The process of finding the optimal triplet begins with a 3 dimensional design space that is initially chosen to be too large. This means that the minimum and maximum lengths of the links are so short or long that it is sure that they will result in a failing triplet. Lengths L_a and L_b range from 1 mm to 300 mm in steps of 1 mm and L_c ranges from 0 mm to 299 mm in steps of 1 mm. The first step is to calculate four inequalities and disqualify triplets that fail to meet the requirements. The calculations of these inequalities are solely functions of constants and L_a, L_b and L_c. This means that they are vectorizable over the design space and are therefore fast to calculate for every possible triplet. This saves on computation time by reducing the number of triplets for the next steps, where more computationally expensive calculations are performed. For a given triplet, the four inequalities ensure that: the margined WS fits within the area constrained by the red singularity circles, the margined WS is not higher than the ceiling of the cryostat and is not lower than the highest point of the bottom blue singularity curve, the left arm does not crash into the sidewall of the cryostat in lower left position in the margined WS, and lastly that there is an OOB position that is sufficiently far to the left.

The Y-coordinates of the top and bottom right corners of the possible WS can be calculated using the right triangles shown in Figure 6.3. Inequality 1 checks that the difference between these two Y-coordinates is large enough to accommodate the necessary margined Y-ROM.

$$TR_y = \sqrt{(L_a + L_b)^2 - \left(\frac{1}{2}L_c + \frac{1}{2}ROM_{x\ margined}\right)^2}$$

$$BR_y = \sqrt{L_b^2 - \left(L_a + \frac{1}{2}L_c - \frac{1}{2}ROM_{x\ margined}\right)^2}$$

$$\text{inequality 1:}\quad -(TR_y - BR_y - ROM_{y\ margined}) \leq 0$$

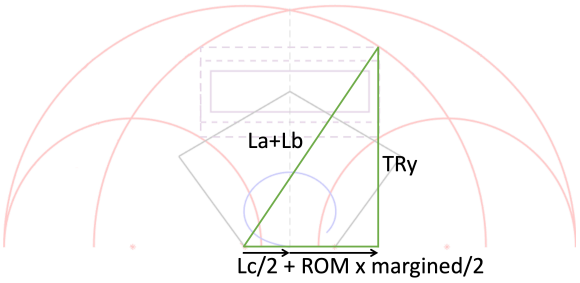

(a) The right triangle used to calculate TR_y. The length of the bottom of the triangle is $L_c/2 + ROM_{x\ margined}$.

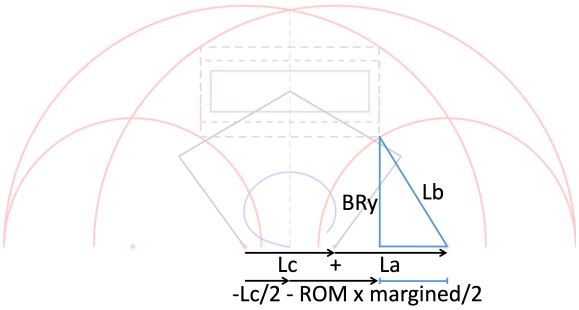

(b) The right triangle used to calculate BR_y. The length of the bottom of the triangle is $(L_c + L_a) + (-L_c/2 - ROM_{x\ margined}/2)$.

Figure 6.3: The right triangle used to calculate TR_y and BR_y.

For inequality 2, BR_y and TR_y are respectively limited to the top of the blue singularity curve and the ceiling of the cryostat. For example, if BR_y is lower than the top of the blue singularity curve, BR_y is set to be equal to the Y-coordinate of the top of the blue singularity curve, otherwise it is left unchanged. The inequality then checks if the Y-ROM is still sufficient. The height of the cryostats ceiling is known. The highest point of the blue singularity curve always occurs at the $L_c/2$ X-coordinate, and when the mechanism is symmetrical and both B-links are horizontal. The Y-coordinate of the highest point of the blue singularity curve is equal to $\sqrt{L_a^2 - \left(L_b - \frac{1}{2}L_c\right)^2}$, as shown using the diagram in Figure 6.4.

$$
\begin{aligned}
TR_y &= \min(TR_y,\ \textit{ceiling height}) \\
BR_y &= \max(BR_y,\ \textit{top blue curve}) \\
\text{inequality 2:}\quad &-(TR_y - BR_y) + ROM_{y\ margined} \leq 0
\end{aligned}
$$

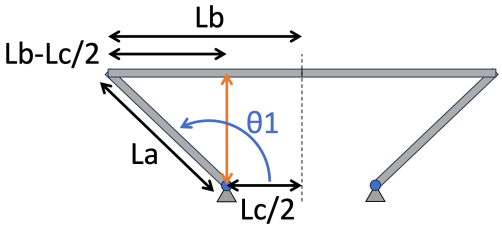

Figure 6.4: The right triangle used to calculate the Y-coordinate of the top of the blue singularity curve.

For inequality 3, the X-coordinate of the elbow of the left arm is calculated for when the EE is positioned in the lower left corner of the margined WS. This will be called the *wideness* of the mechanism as this is the furthest out to the left that any part of the mechanism will reach while the EE is within the WS. As is shown in Figure 5.9, the origin of the mechanism is offset from the center of the cryostat in X-direction. To calculate the wideness, first this mechanism offset must be calculated. The parallelogram length is a chosen dimension that sets the distance between the origin of the mechanism, and the base of the parallelogram arm. The explanatory diagrams to derive the mechanism offset equation are shown in Appendix E.

$$
\begin{aligned}
wideness &= L_a \cos(\theta_1\ in\ lower\ left\ corner) \\
mechanism\ offset &= LVF\ holder\ width + \frac{1}{2}ROM_{x\ margined} + \frac{1}{2}L_c \\
&\quad + \frac{1}{2}(parallelogram\ width - LVF\ total\ width) \\
\text{inequality 3:}\quad &-wideness - (cryostat\ radius - mechanism\ offset) \leq 0
\end{aligned}
$$

The effect these inequalities have on the design space is shown below. Triplets that pass inequalities 1, 2 and 3 will be referred to as 123-viables.

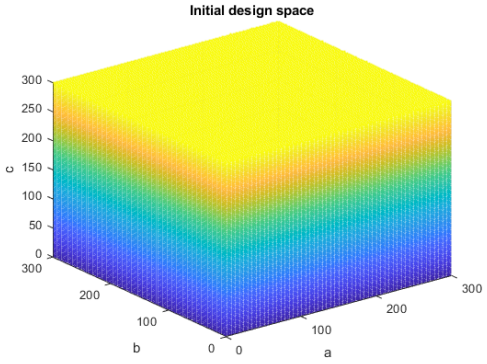

(a) The initial 3 dimensional design space.

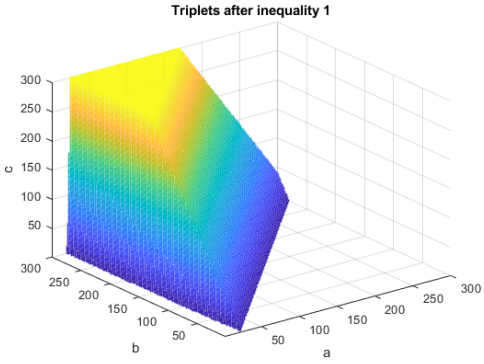

(b) The triplets left after inequality 1.

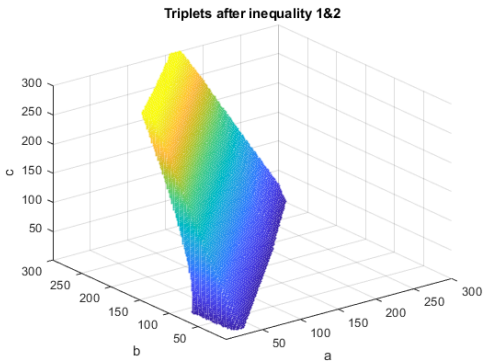

(c) The triplets left after inequality 1 and 2.

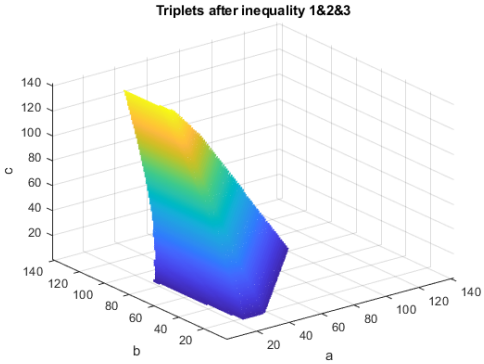

(d) The triplets left after inequality 1, 2 and 3.

Figure 6.5: Scatter plots of the design space. Showing the initial design space, and how triplets get "cut off" by applying the constraints of the inequalities. Note that the axes are more zoomed-in for figure (d).

Lastly, there is inequality 4, which verifies that there is a viable OOB position. While it is true that the LVF must move at least 77.5 mm total in X-direction in order to clear the window of the cryostat, it is not true that while in the leftmost position the LVF must be able to move up or down 20 mm. The true rectangular WS of the mechanism is only required to be 40×20 mm, as long as there is a single OOB position that is sufficiently far to the left. Using Figure 6.6 as a visual aid, the true WS can be set to 40×20 mm and the OOB position can be placed within the pink highlighted area to the left of the WS: which exists if the coordinate of the intersection point of the circles (marked with a black X) is sufficiently far to the left. The X-coordinate of the intersection point can be calculated using circle intersection equations [16] [17]. Another constraint is that the Y-coordinate of the intersection point between the smaller circle (radius L_b and origin at $(-L_a, 0)$) and the vertical dashed OOB line must be lower than the ceiling of the cryostat, otherwise the sufficiently far to the left OOB position can never be reached as the mechanism would crash into the ceiling. This can be calculated as half the length of the chord of the smaller circle at the OOB line. These two conditions (sufficiently far to the left and lower than the ceiling) form inequality 4.

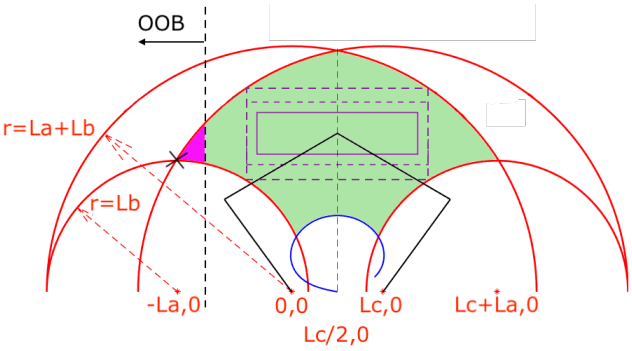

Figure 6.6: The reachable area of the mechanism, showing that the OOB position can be placed in the pink area, allowing for the required true rectangular WS to set equal to the optical area of the LVF.

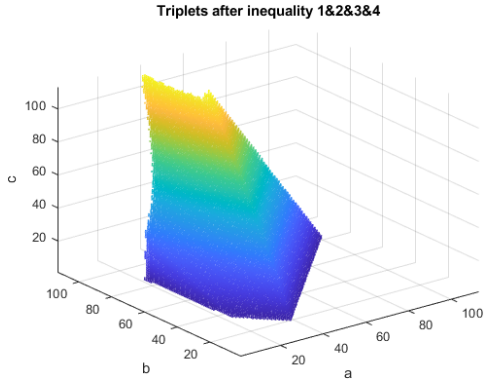

Figure 6.7: The triplets left after inequality 1, 2, 3, and 4. Note that the axes are zoomed-in once again.

6.1.2. Sweeping the Workspace

It is now known that the leftover triplets are able to reach an area large enough to cover the margined WS that they will fit within the cryostat, and that there is a viable OOB position. Now their fitness will be evaluated further. These fitness values require sweeping over the WS of the mechanism. For example, the torque required by the motors changes as the LVF moves through the WS. This torque may be maximum in a predictable point like a corner of the WS, however, like stated earlier, it takes an infinite amount of force to bring the EE to the bottom blue singularity curve. So if the WS is close to this curve, the maximum torque may occur around the center bottom of the WS. Therefore, for completeness and to mitigate any risk of incorrect assumptions, the following performance metrics were calculated over a grid of X,Y points spanning the entire margined WS. As stated earlier, the performance metrics are: required elbow joint flexion ROM, required LVF joint flexion ROM, required motor torque, max joint radial load, required motor angular step size, and optical obstruction distance. From these calculations over the entire WS, it is only the largest or smallest value of a given performance metric that is critical. For example, for a given triplet, if one position within the WS has a joint load of 5 N, while the rest of the WS has joint loads around 1 N, the joints must still be capable of handling loads of 5 N.

6.1.2.1. Setup

A given triplet reaches a given WS. For each triplet the X,Y coordinates of the corners of its accompanying margined WS are known. A grid of X,Y points is created spanning the WS using MATLAB's ndgrid function. Using the inverse kinematic equations of a 5-bar mechanism [18], the angles $\theta_1, \theta_2, \theta_3$ and θ_4 can be calculated for each X,Y point.

$$\theta_1 = 2\tan^{-1}\left(\frac{-F_1 + \sqrt{E_1^2 + F_1^2 - G_1^2}}{G_1 - E_1}\right) \qquad \theta_4 = 2\tan^{-1}\left(\frac{-F_4 - \sqrt{E_4^2 + F_4^2 - G_4^2}}{G_4 - E_4}\right)$$

$$\theta_2 = \cos^{-1}\left(\frac{x - L_a\cos(\theta_1)}{L_b}\right) \qquad \theta_3 = \cos^{-1}\left(\frac{x - L_c - L_a\cos(\theta_4)}{L_b}\right)$$

$$E_1 = -2L_a x \qquad E_4 = 2L_a(-x + L_c)$$

$$F_1 = -2L_a y \qquad F_4 = -2L_a y$$

$$G_1 = L_a^2 - L_b^2 + x^2 + y^2 \qquad G_4 = L_c^2 + L_a^2 - L_b^2 + x^2 + y^2 - 2L_c x$$

6.1.2.2. Elbow and LVF Joint Flexion ROM

Due to the symmetry of the mechanism and the symmetric placement of the WS, the flexion ROM requirement of the left, right, and parallelogram arms are all equal. To calculate the ranges of motion of the joints, first θ_1 and θ_2 are calculated for the different stances of the mechanism over the WS using the inverse kinematics equations. Next the values are be shifted as to start at zero.

$$Flexion_{LVF\ absolute} = \theta_2 - \min(\theta_2)$$
$$Flexion_{elbow\ absolute} = (\theta_1 - \theta_2) - \min(\theta_1 - \theta_2)$$

Lastly the zero flexion position is placed halfway in the total stroke of the joint, so as to range from −value to +value. Which corresponds to the ± in the allowable stroke of a flexpivot.

$$Flexion_{LVF} = Flexion_{LVF\ absolute} - \max(Flexion_{LVF\ absolute})/2$$
$$Flexion_{elbow} = Flexion_{elbow\ absolute} - \max(Flexion_{elbow\ absolute})/2$$

6.1.2.3. Motor Torque and Joint Radial Load

The motor torque calculations take the mass of the EE (LVF mass + bracket mass) and the mass of the links into account. A bracket will have to be designed to serve as the interface between the LVF and its holder, and the links of the mechanism, thus its mass is already taken into account. The parallelogram arm and horizontal link are not taken into account. The equations for the motor torque requirement were adapted from [19]. Once more, due to the symmetry of the system, the torque requirement for both motors is equal. For conciseness only the torque of the motor for the left arm will be referred to. Each link is assumed to be a rectangular prism, with a given width and depth, and its mass is calculated as $volume \cdot density$. The mass of a link is assumed to be a point mass at its center. The mass of the EE is assumed to be a point mass at the location of the EE joint of the mechanism. The placement of C_1, C_3 and C_4 is trivial: their α's are zero, and their r's half of their link length. C_2 is special as it it chosen to incorporate the EE mass as well as the link mass. C_2 is placed at the center of mass (COM) of the two point masses of the link mass and the EE mass. The equations to calculate joint radial loads are also adapted from [19]. The force f_{01} (and due to symmetry also f_{04}) always has the largest magnitude out of all the different forces. For conciseness, this is the force that will be most commonly reffed to when referencing joint loads. Below is the derivation of the torque requirement equation and joint radial load equation. The motor torque results were cross checked with the results from [18]. [18] provides a matrix $\mathbf{A}$ which can be used to to calculate motor torques via $\boldsymbol{\tau} = \mathbf{J}^T\mathbf{F}$ where $\mathbf{J}^T = \mathbf{A}^{-1}$ and $\mathbf{F}$ is the force on the EE. The results were consistent with each other. [18] does not provide a method for calculating joint loads or accounting for links with mass, therefore [19] is preferred.

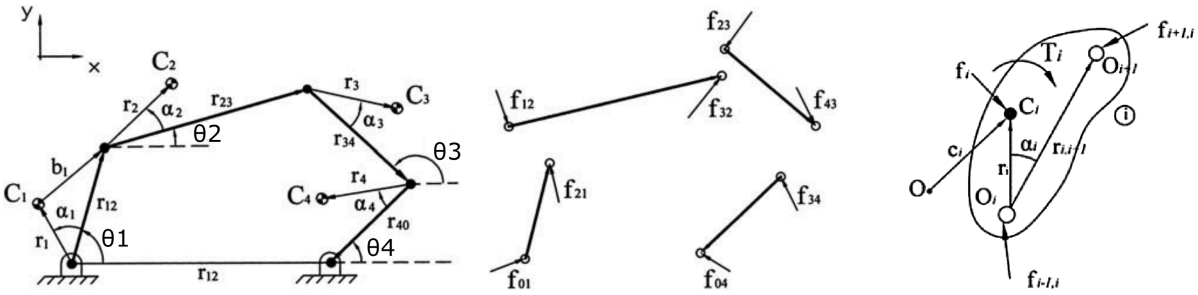

(a) Positions of centers of mass and joint forces.

(b) Free body diagram of a general link.

Figure 6.8: Conventions for use in the equations of motor torque and joint radial loads. Adapted from [19].

The wrench $\mathbf{w}_i$ exerted onto each link can be defined as follows for $i = 1, 2, 3, 4$. Where T_i is the torque on the ith link, f_x and f_y represent the x and y components of the force acting at the COM of the ith link, g is the acceleration due to gravity, and m_a, m_b, m_{EE} are the masses of the A and B-links and the EE respectively.

$$\mathbf{w}_i = \begin{bmatrix} T_i \\ f_x \\ f_y \end{bmatrix}, \qquad \mathbf{w} = \begin{bmatrix} \mathbf{w}_1^T & \mathbf{w}_2^T & \mathbf{w}_3^T & \mathbf{w}_4^T \end{bmatrix}$$

$$\mathbf{w}_1 = \begin{bmatrix} \tau_1 \\ 0 \\ m_a \cdot g \end{bmatrix}, \qquad \mathbf{w}_2 = \begin{bmatrix} 0 \\ 0 \\ (m_a + m_{EE}) \cdot g \end{bmatrix}, \qquad \mathbf{w}_3 = \begin{bmatrix} 0 \\ 0 \\ m_b \cdot g \end{bmatrix}, \qquad \mathbf{w}_4 = \begin{bmatrix} \tau_4 \\ 0 \\ m_a \cdot g \end{bmatrix}$$

The vectors $\mathbf{r}_{i,i+1}$ representing the links can be defined as follows, where L_i is the length of the link and θ_i its angle. $\mathbf{r}_{34}$ and $\mathbf{r}_{40}$ are negative because their angle is not measured at their tail, but at their head.

$$\mathbf{r}_{i,i+1} = \begin{bmatrix} L_i cos(\theta_i) \\ L_i sin(\theta_i) \end{bmatrix}$$

$$\mathbf{r}_{12} = \begin{bmatrix} L_a cos(\theta_1) \\ L_a sin(\theta_1) \end{bmatrix}, \qquad \mathbf{r}_{23} = \begin{bmatrix} L_b cos(\theta_2) \\ L_b sin(\theta_2) \end{bmatrix}, \qquad \mathbf{r}_{34} = -\begin{bmatrix} L_b cos(\theta_3) \\ L_b sin(\theta_3) \end{bmatrix}, \qquad \mathbf{r}_{40} = -\begin{bmatrix} L_a cos(\theta_4) \\ L_a sin(\theta_4) \end{bmatrix}$$

The vectors $\mathbf{r}_i$ representing position of the centers of mass can be defined as follows. Often the location of the COM is half way along the length of the link. For link 2 the location of the COM must be placed at the COM created by the COM of the link and the COM of the EE. The EE mass is positioned at the end of the link, and the mass of the link is positioned half way along the link.

$$\mathbf{r}_1 = 0.5 \cdot \mathbf{r}_{12}, \qquad \mathbf{r}_2 = \frac{m_{EE} + m_b \cdot 0.5}{m_{EE} + m_b} \mathbf{r}_{23}, \qquad \mathbf{r}_3 = 0.5 \cdot \mathbf{r}_{34}, \qquad \mathbf{r}_4 = 0.5 \cdot \mathbf{r}_{40}$$

Next, some variables are defined for later use.

$$\mathbf{b}_i = \mathbf{r}_{i,i+1} - \mathbf{r}_i, \qquad \mathbf{E} = \begin{bmatrix} 0 & -1 \\ 1 & 0 \end{bmatrix}, \qquad \mathbf{1} = \begin{bmatrix} 1 & 0 \\ 0 & 1 \end{bmatrix}, \qquad \mathbf{0} = \begin{bmatrix} 0 \\ 0 \end{bmatrix}, \qquad \mathbf{O} = \begin{bmatrix} 0 & 0 \\ 0 & 0 \end{bmatrix},$$

Next a matrix $\mathbf{B}$ is defined as

$$\mathbf{B} = \begin{bmatrix} \mathbf{r}_1^T\mathbf{E} & \mathbf{b}_1^T\mathbf{E} & \mathbf{0}^T & \mathbf{0}^T & \mathbf{0}^T \\ \mathbf{1} & -\mathbf{1} & \mathbf{O} & \mathbf{O} & \mathbf{O} \\ \mathbf{0}^T & \mathbf{r}_2^T\mathbf{E} & \mathbf{b}_2^T\mathbf{E} & \mathbf{0}^T & \mathbf{0}^T \\ \mathbf{O} & \mathbf{1} & -\mathbf{1} & \mathbf{O} & \mathbf{O} \\ \mathbf{0}^T & \mathbf{0}^T & \mathbf{r}_3^T\mathbf{E} & \mathbf{b}_3^T\mathbf{E} & \mathbf{0}^T \\ \mathbf{O} & \mathbf{O} & \mathbf{1} & -\mathbf{1} & \mathbf{O} \\ \mathbf{0}^T & \mathbf{0}^T & \mathbf{0}^T & \mathbf{r}_4^T\mathbf{E} & \mathbf{b}_4^T\mathbf{E} \\ \mathbf{O} & \mathbf{O} & \mathbf{O} & \mathbf{1} & -\mathbf{1} \end{bmatrix}$$

The joint forces consist of an X and a Y component and are assembled into a new $\boldsymbol{\phi}$ matrix.

$$\mathbf{f}_{01} = \begin{bmatrix} f_{01x} \\ f_{01y} \end{bmatrix}, \qquad \mathbf{f}_{12} = \begin{bmatrix} f_{12x} \\ f_{12y} \end{bmatrix}, \qquad \mathbf{f}_{23} = \begin{bmatrix} f_{23x} \\ f_{23y} \end{bmatrix}, \qquad \mathbf{f}_{34} = \begin{bmatrix} f_{34x} \\ f_{34y} \end{bmatrix}, \qquad \mathbf{f}_{40} = \begin{bmatrix} f_{40x} \\ f_{40y} \end{bmatrix}$$

$$\boldsymbol{\phi}_1 = \begin{bmatrix} \mathbf{f}_{01} \\ \mathbf{f}_{12} \end{bmatrix}, \qquad \boldsymbol{\phi}_4 = \begin{bmatrix} \mathbf{f}_{34} \\ \mathbf{f}_{40} \end{bmatrix}$$

$$\boldsymbol{\phi} = \begin{bmatrix} \boldsymbol{\phi}_1^T \\ \mathbf{f}_{23}^T \\ \boldsymbol{\phi}_4^T \end{bmatrix}^T$$

The matrices can be assembled into the following form as a system of equations.

$$\mathbf{w} = (-\mathbf{B}\boldsymbol{\phi})^T$$

This system of equations can then be rearranged to the matrix form $\mathbf{Ax} = \mathbf{B}$, where $\mathbf{x}$ is the column vector of the variables that are to be solved for, and in this case is therefore equal to $\mathbf{x} = \begin{bmatrix} \boldsymbol{\phi}^T & \tau_4 & \tau_1 \end{bmatrix}^T$. After which the equations for the joint loads and motor torques can be obtained by solving the linear system of equations for $\mathbf{x}$ ($\mathbf{x} = \mathbf{A^{-1}B}$). These equations will be functions of the stance of the mechanism ($\theta_1, \theta_2, \theta_3$ and θ_4), and known constants (such as L_a, L_b, m_{EE} and g).

6.1.2.4. Motor Angular Step Size

The grid of X,Y coordinates that spans the margined WS has some resolution. Ideally this resolution would be 25 µm in both X and Y. That way the performance of the mechanism is calculated in every position the mechanism could find itself in. However this is too computationally expensive. So a compromise must be made. Initially this resolution is coarse, as there are more triplets to search

through. As the knowledge of the problem grows, the design space can be reduced, and the resolution increased. Initially a coarse grid with steps of 1000 µm was used. When using such a coarse grid, it is still desirable to extract information regarding the angular steps the motor would need to be able to take if asked to take a step of 25 µm (instead of 1000 µm). This is motor angular step size: the angular step required by the motor, in order to produce the required 25 µm step in the position of the LVF, in either X or Y direction. Once again, due to the symmetry of the system, this requirement is the same for both motors. The requirement for one motor in the top left position, will be the same for the other motor when the mechanism is in the top right position (position mirrored around the $L_c/2$ line). Each X,Y point in the WS has an associated θ_1, and this motor step requirement can be calculated using finite difference in each point on the grid.

$$required\ motor\ step\ x = \frac{\mathrm{d}\theta_1}{\mathrm{d}x}\ desired\ LVF\ step\ x$$
$$required\ motor\ step\ y = \frac{\mathrm{d}\theta_1}{\mathrm{d}y}\ desired\ LVF\ step\ y$$

Where *required motor step* will be the required angular step of the motor in that position in the WS to move the LVF in either X or Y direction, dx or dy is the difference between the X or Y coordinate in a given position in the WS and the X or Y coordinate in adjacent positions, dθ_1 is the difference between the θ_1 value in a given position in the WS and the θ_1 value in adjacent positions, and *desired LVF step x* is equal to 25 µm.

A convergence and sensitivity study was done for the different WS sweep calculations to determine that the 1000 µm grid resolution was sufficient for the preliminary discovery. However, the motor step calculation was discovered to be quite sensitive to the lower resolution grid, and was also computationally expensive. A different method to calculate the motor step was developed in an attempt to aid these shortcomings. Motor step can also be calculated analytically and derived from the inverse kinematic equations. The equation for θ_1 as a function of EE X,Y coordinate is known. Taking its derivative to x and to y will result in two equations, one for *required motor step x* and one for *required motor step y*. However this equation is large and complex and did not reduce the computation time significantly. Additionally it suffered equally from sensitivity to lower resolution grids. Due to the importance of calculating an accurate motor step requirement, and its sensitivity to low resolution grids, the decision was made to run the finite difference motor step calculation at 25 µm resolution for every triplet and save the results. These results could then later be loaded, avoiding long computations and poor quality results. The finite difference method was chosen because it was deemed to be the most robust and correct. The mechanism is put into every stance it could possibly find itself in, and the angular change in θ_1 required for the LVF step of 25 µm can be directly calculated by simply comparing θ_1 to the θ_1 in its neighboring positions. Triplets that pass inequalities 1, 2, 3, 4 and the motor step requirement will be called 1234ms-viables. Motor step calculations depend only on the lengths of the links, and the dimensions of the margined WS. Furthermore, being able to take 25 µm steps is only required within the optical WS of the mechanism. For example, when the LVF is put in the OOB position by the mechanism, step size is not critical.

6.1.2.5. Optical Obstruction Distance

Optical obstruction is calculated for every link of the mechanism (including the parallelogram arm and the horizontal parallelogram link). The position and orientation of every link in every stance over the WS is known. While the LVF is within its optical WS, meaning that its optical area is being scanned, there may be no obstruction of the focused beam. When in the OOB position, there must be at least one stance where there is no obstruction of the cryostat's optical window. Additionally, for the collimated mode, when the LVF is placed centrally over the window of the cryostat, there may be no obstruction of any part of the optical area of the LVF. The calculations for all three are done in the same manner: calculating the shortest distance from a line segment to a point. Each link of the mechanism is treated as an infinitesimally thin line segment, and the point is positioned in the center of the cryostat's window. This distance can then be required to be larger than $link\ width/2 + beam\ spot\ diameter/2$ in the optical WS, or larger than $link\ width/2 + cryostat\ window\ radius$ in the OOB position.

6.2. Optimal Triplet

A detailed description of the process of finding the optimal triplet is provided in Appendix F. A summary of key findings is provided below in bullet-form.

- The torque of smallest VSS stepper motor is sufficient for all of the 123ms-viable triplets.
- The application of flexpivots in all, or even only some, of the joints of the mechanism is infeasible.
- The possibility of a series arrangement of two flexpivots was also investigated. Series flexpivots theoretically double the possible ROM of the joints, however they pose downsides regarding stiffness and load capacity, and are generally discouraged. Series flexpivots did not result in enough gains in mechanism performance and design freedom to justify their use over ball bearings. Therefore ball bearings are recommended, removing the limits on the flexion ROM of the joints, opening up design possibilities.
- Smaller L_c triplets are discovered to generally be better performers with more optical obstruction margin. L_c is set to zero, eliminating one of the three design variables.

The true WS of the mechanism is set to be equal to the optical area of the LVF (40×20 mm). The optimal triplet is found by searching in the 1234ms-viables for the triplet with the largest optical obstruction distance. This results in the triplet shown in Figure 6.9 and 6.10 ($L_a = 36$ mm, $L_b = 35$ mm, $L_c = 0$ mm). Assuming mechanism links with a 5×5 mm cross section, this triplet has an optical obstruction margin of 7 mm. Coincidentally, and advantageously, this triplet also has a generous 8 mm of ROM margin. This is the most optimal triplet for the 40×20 mm LVF. A parallelogram length of 100 mm was found to be optimal, as it places the parallelogram arm sufficiently far to the right as to not optically obstruct in the collimated measurement mode position, and sufficiently far to the left as to not optically obstruct in the OOB position. In Figure 6.9 the mechanism's origin is shown to be 27.5 mm higher than the floor of the cryostat. This *floor offset* is required to provide the necessary space for the motors, connecting material, and 10.25 mm needed for BIORAD compatibility.

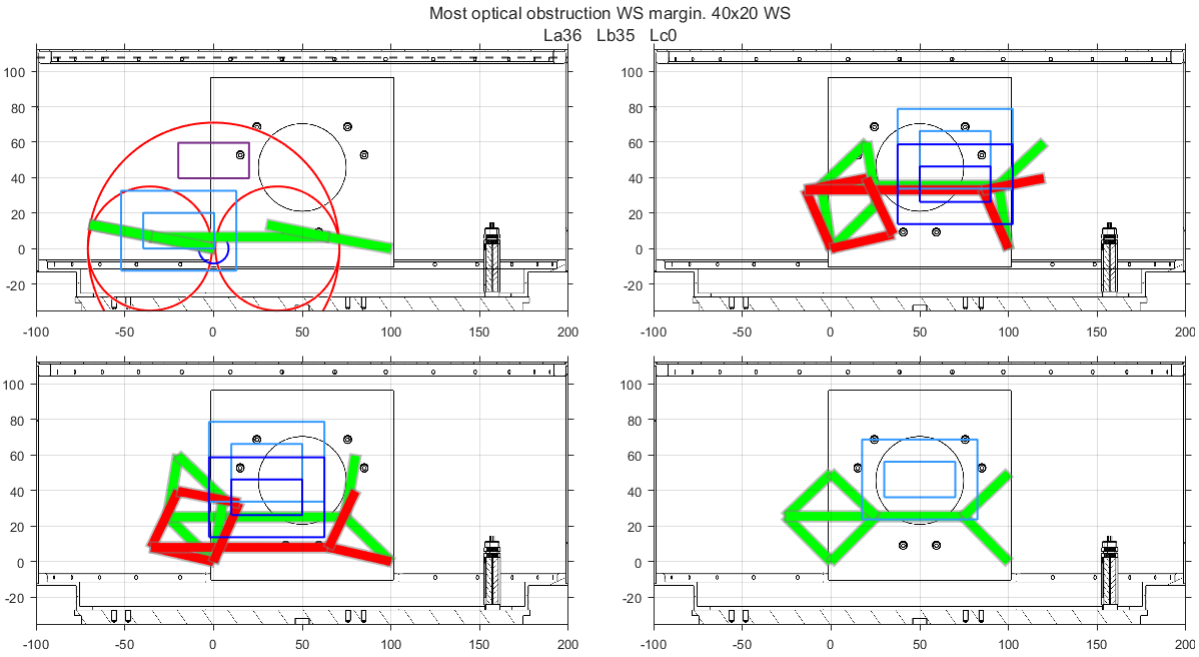

Figure 6.9: A cryostat representation of the triplet optimized for the largest optical obstruction margin over a 40×20 mm WS. The triplet has 7 mm of optical obstruction margin and 8 mm of WS margin. Shown in the top left is the mechanism in the OOB position. In the bottom right, the mechanism in the collimated measurement mode position. The top right and bottom left images show the mechanism positioned in all four corners of the true WS.

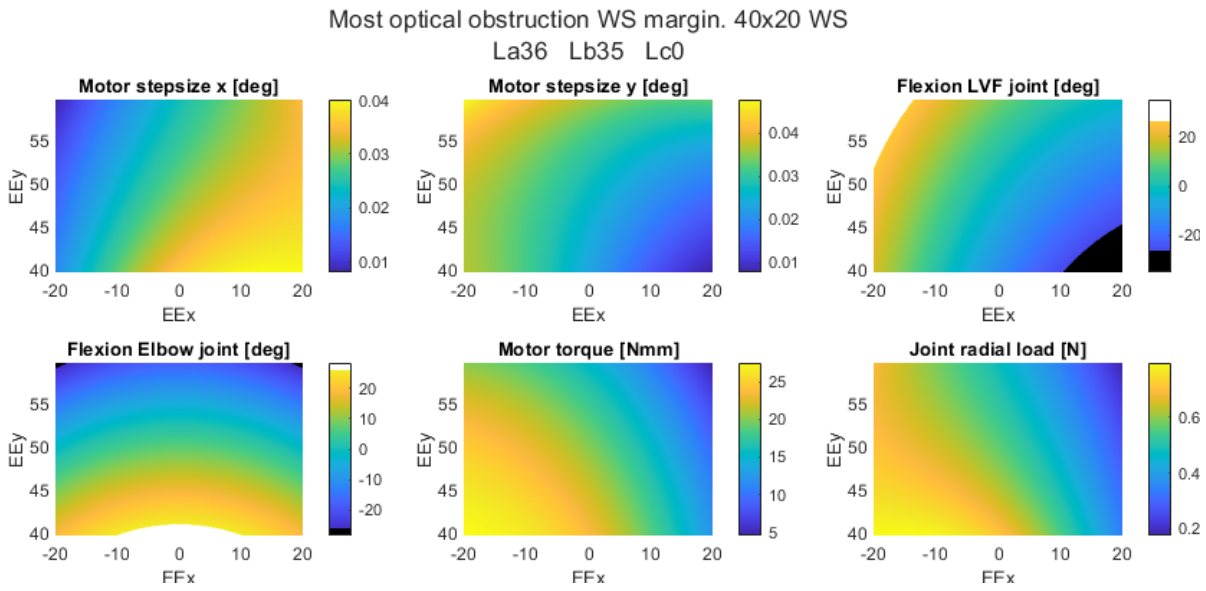

Figure 6.10: Heatplots over the true WS for the triplet optimized for the largest optical obstruction margin over a 40×20 mm WS. The triplet has 7 mm of optical obstruction margin and 8 mm of WS margin. White and black in joint flexion plots indicates joint flexion in excess of the limits of series flexpivots.

During the course of the thesis, it became evident that there may be a desire to scale up the dimensions of the LVF to 55×25 mm, thus it is valuable to asses the mechanism's ability to scan this larger 55×25 mm LVF.

Achieving 25 µm steps over this larger 55×25 mm LVF while avoiding optical obstruction is challenging. There is not a single 1234ms-viable triplet which does not obstruct in the WS. Dropping BIORAD compatibility, and thereby being able to reduce the floor offset by 10.25 mm, does not resolve this. Therefore BIORAD compatibility is maintained. The search for the most optimal triplet for the 55×25 mm LVF is conducted within the 1234ms-viable triplets, optimizing to minimize the area where the motor steps are unacceptably small. This can be visualized as minimizing the black area in the motor step size heatplot (Figure 6.13), or in other words, finding the triplet with the largest area of acceptable motor step.

The optimal triplet varies based on the minimum optical obstruction distance that is acceptable. This is illustrated in Figure 6.11, where the best performing triplets are highlighted. As the optical obstruction margin increases, so does the area of the LVF that cannot be scanned with 25 µm (or smaller) steps. This presents a balancing act. An optical obstruction margin of 3.5 mm and the accompanying 2.9 % of single-motor failing area was determined to be a good compromise. It is important to note that the failing area is in-fact $2.9 \cdot 2 = 5.8$ % due to the fact that the two motors of the mechanism fail in different parts of the workspace. The heatplot for the motorstep required of the stepper motor driving θ_1 is shown in Figure 6.13, where it it shown to fail in the top left corner of the WS. The stepper motor driving θ_4 will (due to the symmetry of the system) fail the motor step requirement in the *top right* of the WS.

This triplet, in conjunction with Phytron VSS-25 stepper motor and a 245 gearbox, is the final recommendation, and considered to be the most optimal and best performing triplet possible. It is able to scan the 40×20 mm optical area of the small LVF with the required step size of 25 µm or smaller. It is optimized to be able to scan the maximum area of the 55×25 mm with 25 µm (or smaller) steps while still maintaining a margin of 3.5 mm to optical obstruction. The maximum joint load is a fraction of the maximum acceptable joint load, and the maximum occurring motor torque is a factor 12.6 times smaller than the detent torque of the VSS-25 stepper motor with a 245 gearbox. It is worth noting that if it is desired to scan the black area of the motor step graph with 25 µm (or smaller) steps it is still possible through microstepping of the stepper motor. This however comes at the cost of dissipation, as detent torque is not able to be used when in between full steps, and therefore the motor can not be depowered. Figure 6.12 shows that the triplet (with 5×5 mm cross-section links) shows no optical

obstruction in the WS, in the OOB position, or in the collimated position. Figure 6.13 shows that the motor torque and joint load are acceptable at every point within the optical WS, and that the upper left corner of the WS is where the motor step size is unacceptable.

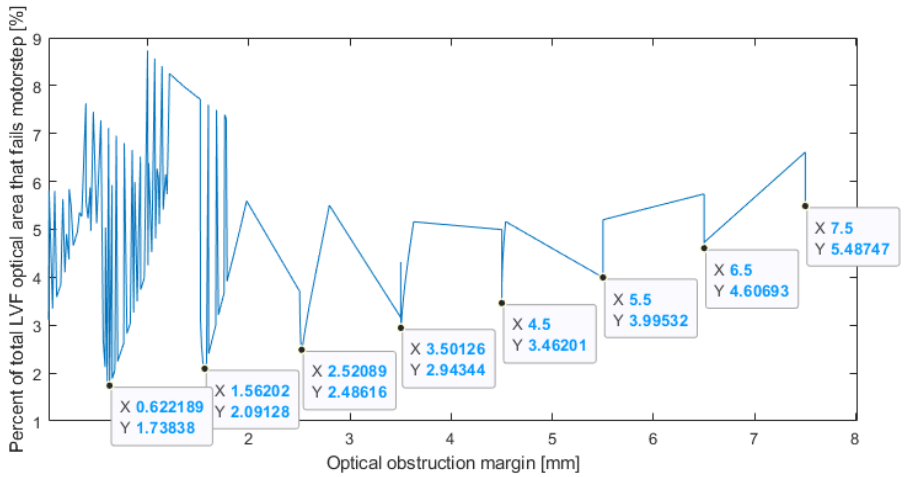

Figure 6.11: A plot showing, for all remaining triplets, the percent of total LVF area that fails the motor step requirement vs. the optical obstruction margin.

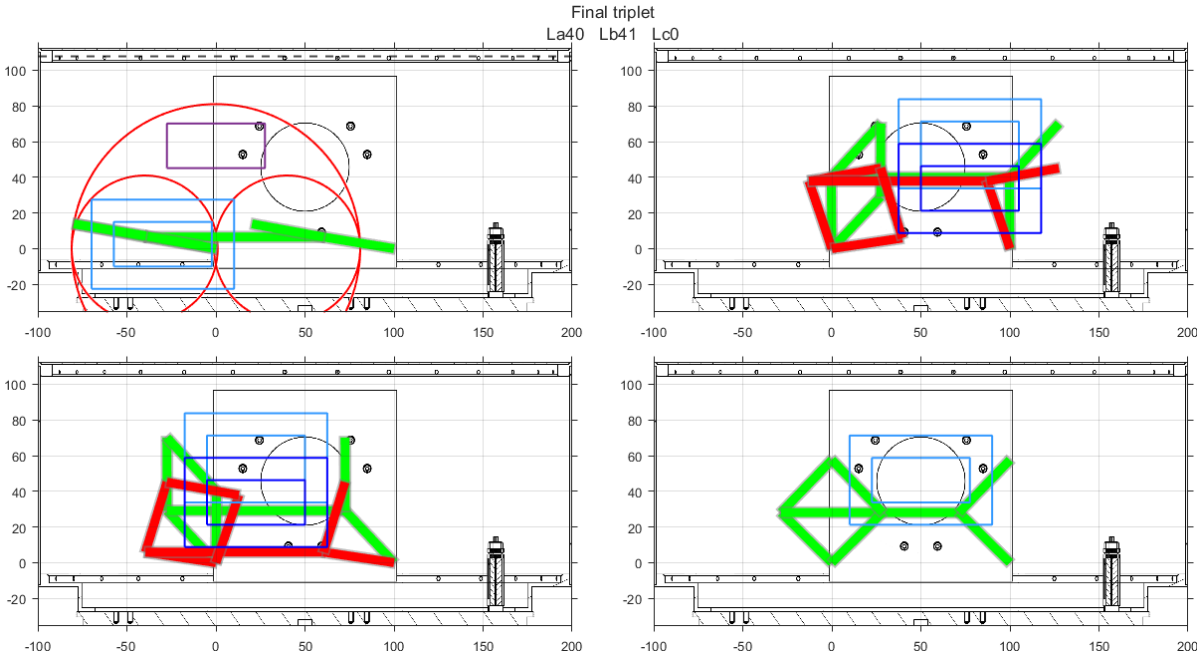

Figure 6.12: Cryostat representation of the final triplet.

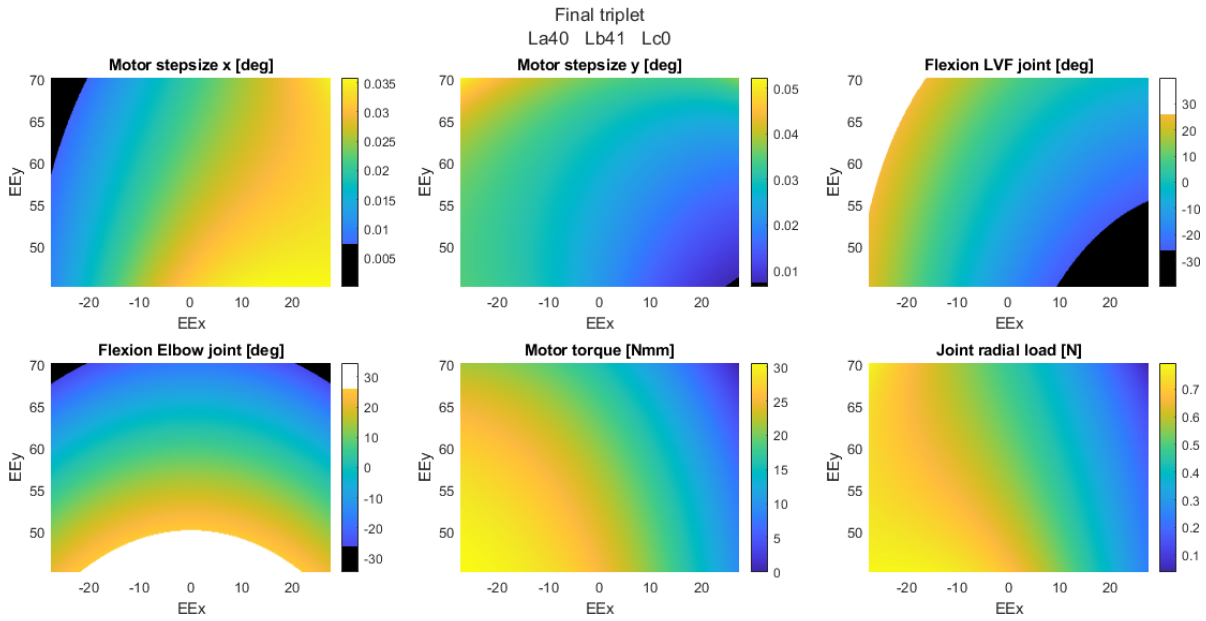

Figure 6.13: Heatplots for the final triplet.

6.3. Phytron Motor and Gearbox Selection

Phytron VSS stepper motors are recommended for the mechanism driving stepper motors as they have been use before, and tested extensively within SRON. The specific VSS stepper motor and gearbox recommend is the Phytron VSS 25.200.0.6 with standard backlash VGPL22 (245) gearbox.

The VSS-25 is preferred over the VSS-19 due to its twice as large detent torque (2 Nmm) providing a large safety factor of 12.6. The increase in motor diameter has no impact on the mechanism as it is the gearbox diameter which plays the limiting role, and is equal for both. Additionally, the VSS-25 has a larger motor constant (13.3 $\frac{\text{N mm}}{\text{A}}$) than the VSS-19 (5.67 $\frac{\text{N mm}}{\text{A}}$). An increase of a factor of 2.35. The motor constant data is sourced from private communications with Morskate [20], the distributor of Phytron stepper motors in the Netherlands. A larger motor constant means that for the same torque, the VSS-25 motor will require less electrical power, and therefore also dissipate less heat. Furthermore, as denoted by the last two digits in the product code, the 0.6 A version of the stepper motor is preferred over the standard 1.2 A version. This is because for an electrical wire $P = I^2R$, where P is the power dissipated as heat in Watts, I is the current through the wire in Amps and R is the resistance of the wire in Ohms. Therefore, for low dissipation, it is the lower amperage version of the motor that is desired. Lastly, the price difference between the two motors is very small, around €200.

The 245 gearbox is the largest ratio gearbox available for the VSS-25. The next significantly larger ratio gearbox available is 400. However this gearbox requires a VSS-52, who's diameter is roughly twice as large as the chosen VSS-25. This increase in diameter would result in a raising of the base of the arms of the mechanism, and would result in more challenges with optical obstruction and limitations imposed by the ceiling of the cryostat. The standard backlash version of the 245 gearbox is chosen. This is because the reduced backlash version still has an unacceptable amount of backlash. Therefore in both cases a backlash elimination system must be designed, and the reduced backlash gearbox poses no benefit.

The drive angles θ_1 and θ_4 range from approximately 90° to 170°; a stroke of 80°. [21] states that within private communications with Phytron it was recommended not to exceed a motor speed of 100 rpm at cryogenic temperatures. Using this, an estimate for the worst case cycle-time can be made. 100 rpm is 600 deg/s, which becomes 2.45 deg/s after the 245 gearbox. This results in a maximum cycle-time of 32.7 s; approximately 5.5 times slower than the target requirement. The mean of all the drive angles is 133°, resulting in an average stroke of 37°, which consequently results in an average cycle-time of 15 s; 2.5 times slower than the target requirement. This results in an achieved duty-cycle of $\frac{movement\ time}{measurement\ time+movement\ time} = \frac{15}{60+15} = 20\,\%$, two times larger than the target.

Within the mechanism, the maximum torque required is in the OOB position, and is approximately equal to 30 Nmm. Expected dissipation can be estimated using results from [21], where a VSS 19.200.0.6 with 196 gearbox (resulting in a detent torque of 176.4 Nmm and a max torque of 666.4 Nmm) was thoroughly tested at 4 K. Tests were preformed at 100rpm. When delivering a torque of 60 Nmm the motor dissipated 49 mW of heat, and the wiring 405 mW, leading to a total dissipation of 454 mW. Assuming linearity (which is a considerable assumption), if this test was conducted at a torque of 30 Nmm the total dissipation would have been 227 mW. Knowing that the motor constant of the VSS-25 is 2.35 times larger than that of the VSS-19, and once again making the assumption that dissipation scales linearly, a VSS-25 producing 30 Nmm at 4 K is estimated to dissipate 97 mW of heat. Assuming the worst case, that when the motor is powered (in order to move the mechanism), it is continuously asked for the maximum expected torque, and taking into account the 10 % duty cycle of the mechanism, the worst case average dissipation of one motor is estimated to be 19.4 mW. There are two motors in the system, and both are required to be powered to move the mechanism, bringing the total estimated dissipation to 38.8 mW. This is approximately four times larger the stated requirement. However, there is no lower dissipation actuator available than a stepper motor where the detent torque is sufficient to support the mechanism in every position. So while the order of magnitude estimation for the expected dissipation is out of spec, no steps taken along the way could have resulted in a significantly lower dissipation system than what has been recommend.

7 Detailed Design Phase

7.1. Tolerance Analysis

7.1.1. Method

Theoretical ideal nominal link lengths have been established, however in reality the manufactured links will have some error in their dimension. Those perturbations in the lengths of the links will have some effect on the accuracy of the measurement of the mechanism's position. The way the position of the LVF is determined is through the measurement or knowledge of the input angles θ_1 and θ_4. Any uncertainties in the chain from input angles to LVF will therfore reduce the certainty in LVF position. Uncertainties in the chain come from the lengths of the links, and the runout of the ball bearings. A tolerance analysis must be performed in order to provide a requirement for the manufacturing tolerance of the link lengths and the runout of the ball bearings, and to be able to make statements regarding the expected performance of the mechanism given these tolerance requirements. The mechanism is defined by 9 lengths as shown in Figure 7.1a where *L, R* and *P* respectively stand for *left, right* and *parallelogram*. Errors in the lengths of these dimensions result in errors in the X,Y position of the LVF and its angle, as shown in Figure 7.1b. The abs or absolute error in position is also calculated as $\sqrt{X^2 + Y^2}$.

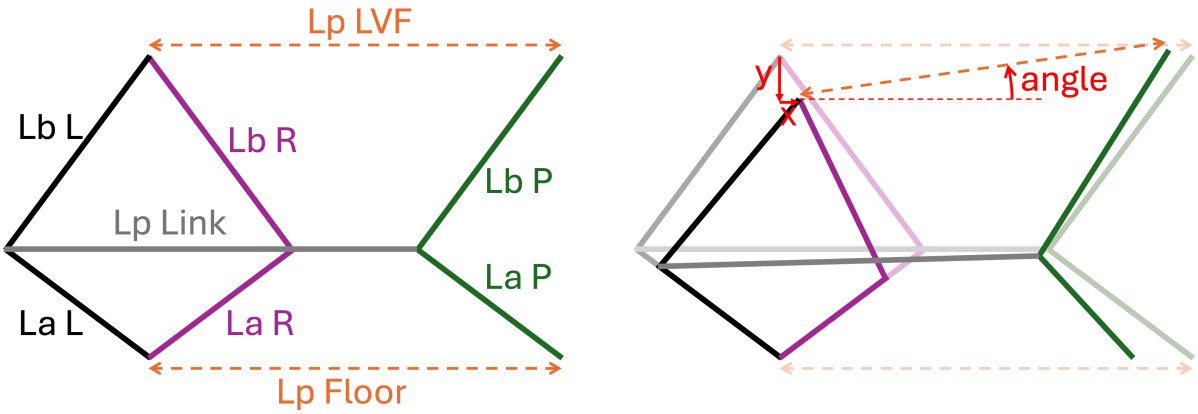

(a) Naming of the 9 dimensions that define the mechanism.

(b) How perturbations in link lengths effect cause errors in the position and angle of the LVF.

Figure 7.1: Conventions used in the tolerance analysis of the mechanism.

The tolerance analysis is performed as a Monte Carlo simulation. The nominal length of each link is known.

$$\begin{aligned} L_{aL} = L_{aR} \quad &= L_{aP} \quad &= L_a \\ L_{bL} = L_{bR} \quad &= L_{bP} \quad &= L_b \\ L_{p\ floor} = L_{p\ link} &= L_{p\ LVF} &= Parallelogram\ length \end{aligned}$$

For this nominal, or ideal, mechanism, the required input angles θ_1 and θ_4 are calculated for a grid of X,Y point in the optical WS. This step is performed only once. Next, each of the 9 lengths that define the mechanism are each individually perturbed by different random values which are generated according to a normal distribution where there is a 99.7% chance that the perturbation value will fall within $\pm max\ tolerance$. This perturbed mechanism is then driven by the already calculated ideal θ_1 and θ_4. The X,Y position and angle of the LVF resulting from driving this non-ideal perturbed mechanism with ideal inputs is then compared to the ideal X,Y position and angle (which is always 0°). The error in X position, Y position and angle of the LVF can then be calculated as the difference

between the perturbed position and the ideal position. This process repeats for a sufficient number of perturbed mechanisms to ensure convergence of the Monte Carlo simulation. Convergence was tested via trial-and-error by comparing lower iteration and lower WS resolution results to a reference result derived from an ideal 25 µm resolution WS grid and 5e5 Monte Carlo iterations. Trial-and-error found that grid steps of 10·25 µm and 1e5 iterations was sufficient. Furthermore, as shown in Figure 7.5, it is expected that the largest errors in LVF position occur at the edges of the WS. No matter the resolution of the grid, the edges are always included. Therefore emphasis was placed on a higher number of simulation iterations, rather than a higher WS resolution.

In-house manufacturing at SRON is capable of fabricating parts with a tolerance of approximately ±100 µm with ease. Additional precision and care is required to achieve tolerances of approximately ±50 µm. The maximum achievable tolerance is approximately ±10 µm. Additionally, measurements can be made with an accuracy of approximately ±2 µm. Furthermore, as detailed in Appendix A.2, ball bearings of ISO class 2 have a radial runout of 1.5 µm (or ±0.75 µm) [22]. Each link is given a normally distributed random perturbation with a 99.7 % chance that the perturbation value will fall within $max\ tolerance = \pm(manufacturing\ tolerance + 2 \cdot bearing\ runout)$. Bearing runout is multiplied by 2 because there is a bearing at both ends of a link.

7.1.2. Results

The mechanism manufacturing method that results in the least possible position error is to manufacture the links together, at the same time. The length of a link is defined by the distance between the centers of its two holes. Normally, each link would be manufactured individually. Therefore each link has its own, individual, perturbation on its nominal dimension. However, the links can be manufactured at the same time, like shown in Figure 7.2. Here one hole is drilled through a blank of material, after which the individual links can be separated from each other. This results in the lengths of all the links in the stack being defined by the same hole, and therefore being equal. The lengths of the links in the stack are all perturbed from the nominal dimension by the exact same amount. This can be done for all the L_a and L_b links, however is not feasible for the three different parallelogram lengths. To implement this in the Monte Carlo simulation, all L_a links receive the exact same perturbation resulting from the manufacturing or measurement tolerance. The same occurs for the L_b links. The parallelogram lengths each receive an individual manufacturing or measurement perturbations. Finally, each link receives an individual perturbation as a result of the ball bearing runout, as this is not something that can be made equal between the links. Applying the tightest possible ±2 µm measurement tolerance leads to the Monte Carlo results shown in Figure 7.3, 7.4 and 7.5. Tolerance analysis results for looser tolerances with individual link length perturbations are discussed in Appendix G.

Figure 7.3 shows histograms of the perturbation values for each of the different links, for each of the 1e5 Monte Carlo iterations. Figure 7.4 shows histograms of the maximum error that occurs anywhere within the WS of the 1e5 different perturbed mechanisms. The vertical lines drawn denote the 95 % confidence interval. This allows for the statement to be made that if the mechanism is manufactured with the specified tolerances, it is 95 % certain that the worst error that occurs anywhere in the WS will be in between A and B, where A and B are the error values displayed along those vertical lines. The errors in the X and Y position of the LVF are of the most interest, as these are the errors upon which the critical ±2.5 µm requirement is placed. Lastly, Figure 7.5 presents heatplots. The errors are often mirrored around $x = 0$. Therefore plotting, at each point in the WS, the mean of the error for the different Monte Carlo iterations does not result in informative plots. The positive and negative errors cancel each other out. Therefore it is the mean of the *absolute value* of the error at each point point in the WS that is plotted in the heatplots. These plots give insight into where in the WS the largest errors occur, but obscure the information regarding whether that error is positive or negative. The largest error within a heatplot will be approximately equal to the error value at its histogram's positive peak.

Using Figure 7.4, the conclusion can be made that manufacturing the L_a and L_b links at the same time, and measuring their length with an accuracy of ±2 µm results in a mechanism that is almost satisfies the requirement of ±2.5 µm error for both X and Y. The 95 % certain maximum error in X is approximately ±2.5 µm and the error in Y is approximately ±2.9 µm. Notably this stacked method of manufacturing also eliminates the issues detailed in Appendix G, where 18 of the 1e5 mechanisms failed to be able to reach every point in the WS when manufactured with the ±100 µm tolerance. Manufacturing with

this stacked method therefore allows for very loose $\pm 100\,\mu m$ manufacturing tolerances, followed by an accurate $\pm 2\,\mu m$ measurement. The manufacturing effort should be placed into measuring the perturbed lengths of the links as accurately as possible. Accurately knowing the length of a link is far more important than its length being close to nominal.

The shape of the histograms in Figure 7.4 is expected. Zero error is highly unlikely. This would require either a mechanism with zero perturbations for each of it links, or a mechanism where the different perturbations cancel each other out. Both of which are unlikely to occur. Similarly, large errors necessitate a mechanism with large perturbations which are all in the same direction (either all + or all −). This is also unlikely. The symmetry of the histograms about $x = 0$ is expected, as the perturbations themselves are symmetric about $x = 0$. Given the mechanism's symmetry, and the equal likelihood of perturbations being either positive or negative; it is expected that the positive and negative error distribution are the same. The skewness of the distribution could be due to the fact that a large positive error requires all links to be perturbed in the positive direction; which is less likely. It is more probable for a mix of positive and negative perturbations to occur, potentially leading to some cancellation, resulting in a mean that is skewed towards zero.

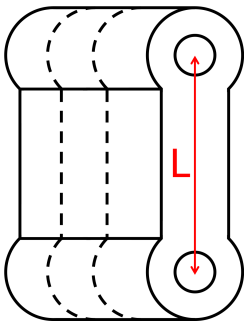

Figure 7.2: Manufacturing links at the same time, in a stack, results in their dimensions being perturbed by the exact same amount.

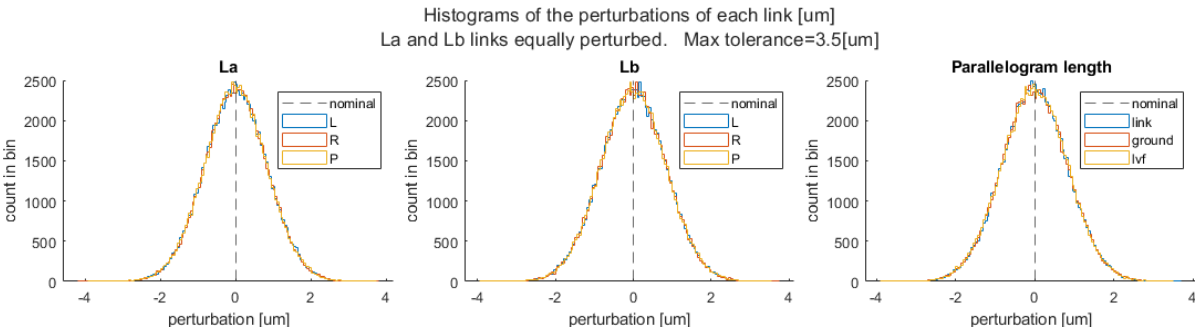

Figure 7.3: Histograms showing the perturbation values for each of the different lengths of the mechanism for a measurement tolerance of $\pm 2\,\mu m$.

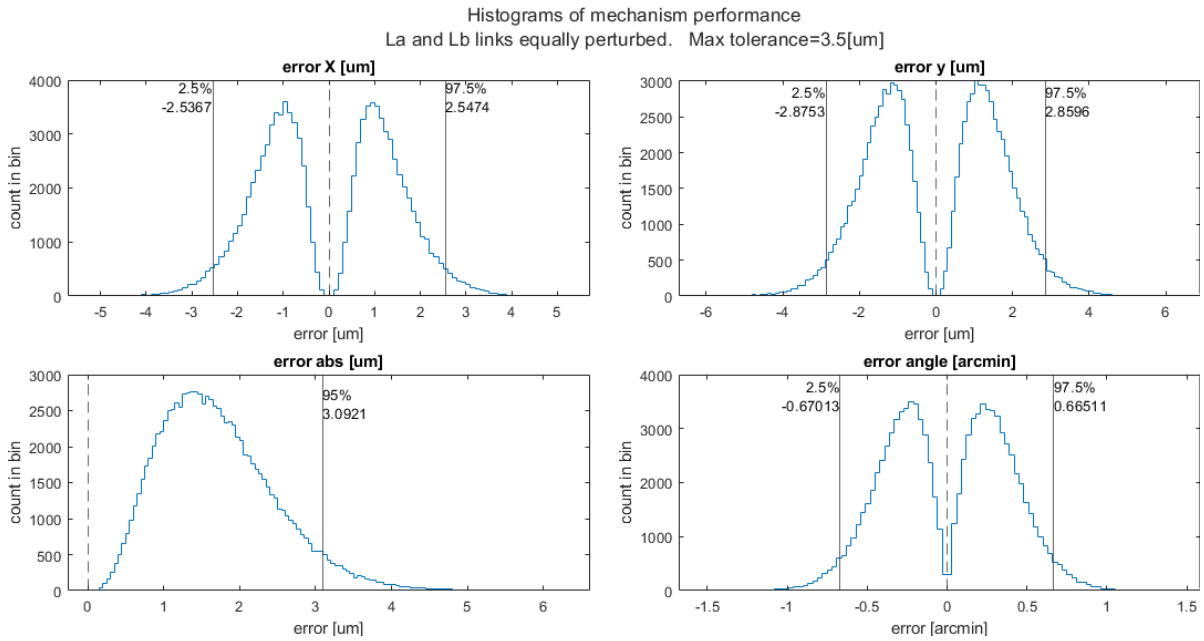

Figure 7.4: Histograms showing the performance of the different perturbed mechanisms for a measurement tolerance of $\pm 2\,\mu m$. The largest error that occurs anywhere within the WS of a given perturbed mechanism is plotted.

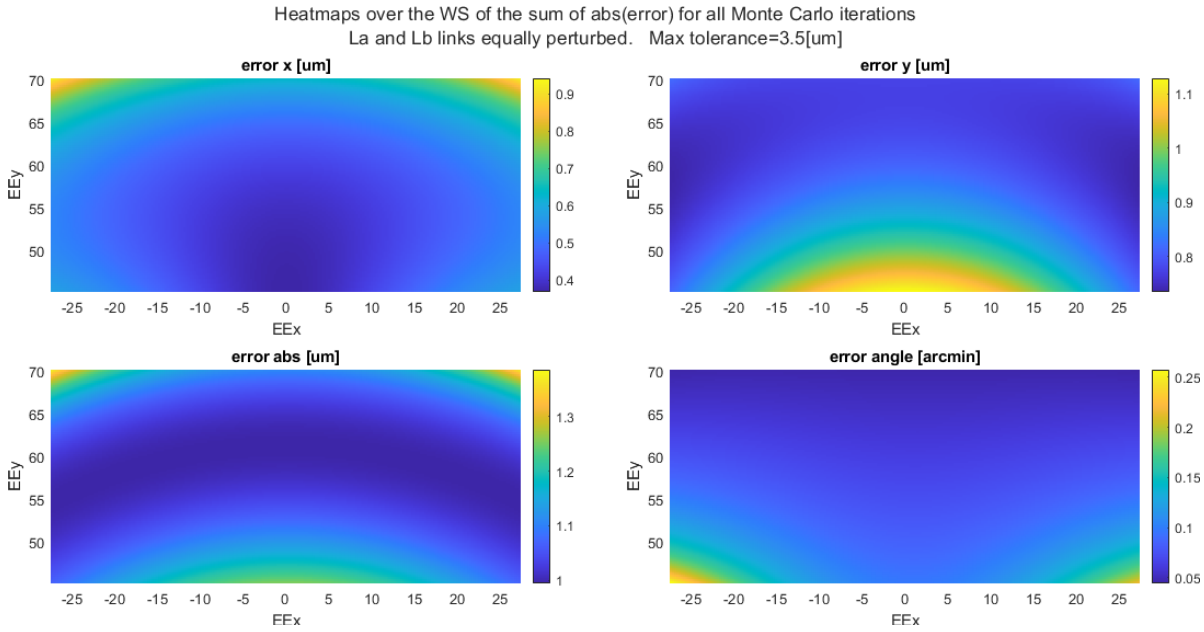

Figure 7.5: Heatplots showing where in the WS the largest errors occur for a measurement tolerance of $\pm 2\,\mu m$. The heatplots are made by summing the absolute value of the errors over the WS of the different perturbed mechanisms from the Monte Carlo simulation.

Uncertainties in the drive angle of the links have not been taken into account in this tolerance analysis. The input angles θ_1 and θ_4 are taken to be known with absolute certainty, which in reality will not be the case. The VSS stepper motor has a step accuracy of $\pm 5\,\%$ on its 1.8° steps [8], resulting in an uncertainty of $\pm 0.09^\circ$. After the 245 gearbox this becomes ± 1.271 arcseconds of uncertainty in θ_1 and θ_4. The effects of this uncertainty on the error in X and Y position of the LVF has not been investigated over the WS, however a worst case estimation can be made. The motorstep constraint requires that an angular step of $1.8/245 = 26.45$ arcseconds produces a 25 um step in LVF position, or $25/26.45 = 0.945$ µm/arcsecond. Therefore, in the worst case, the uncertainty of ± 1.271 arcseconds in the drive angle results in an LVF position uncertainty of $\pm 0.945 \cdot 1.271 = \pm 1.2\,\mu m$. Multiplied by two because there are two motors results in a total uncertainty due to the uncertainty in drive link angle of $\pm 2.4\,\mu m$. Summing the 95 % certain largest error within the WS due to link length uncertainty, and the worst case error due to the motor drive angle, results in a total 95 % certain worst case error of $\pm 4.9\,\mu m$ in X, and $\pm 5.3\,\mu m$ in Y; approximately two times larger than the target requirement.

Furthermore ISO class 2 bearings have been shown to be necessary. Said more precisely, a maximum bearing runout of $\pm 0.75\,\mu m$ has been shown to be necessary. In the sourcing of bearings it is important to discuss with the manufacturer on how to achieve the smallest runout possible, or an acceptable amount of runout. Many factors play a role in determining the uncertainty that a bearing injects into the system. For example preloading a bearing, as shown in Figure 7.6, increases its running accuracy [23]. Additionally, it was mentioned in private communications with HQW [24], a precision miniature ball bearing manufacturer, that the tolerance on the roundness of the hole that a bearing gets press-fitted into may play a larger role in the running accuracy of the bearing than the fact that it is ISO class 2. The manufacturers found that claimed to be capable of producing small ISO class 2 ball bearings are: HQW [24], New Hampshire Ball Bearings [25], National Precision Bearing [26], Carter bearings [27], UNASIS International [28], Cerobear [29], Myonic [30], Barden [31] and Fridman [32]. Some manufacturers claim to be able to produce bearings for 4 K cryogenic environments, and some manufacturers also work together or fall under the same parent company.

Lastly, when used at low temperatures, the links will shrink due to thermal expansion/contraction. Over a range from 20 C to 4 K, this thermal expansion is $-0.004\,154\,5\,\frac{m}{m}$ for aluminum 6061 [33]. Leading to the following ΔL for Link A (40 mm), link B (41 mm), and the parallelogram link (100 mm): $-166.18\,\mu m$, $-170.33\,\mu m$, $-415.45\,\mu m$. These changes in length are significant and must be accounted for by adjusting the link length accordingly in the kinematic equations used in the feed forward controls of the mechanism. If not done, it would result in an 'uncertainty' in link length on the order of 100s of microns, which would result in a significant error in LVF position.

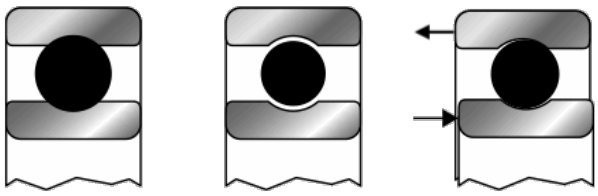

Figure 7.6: A series of three images showing how bearing preload plays an important role in determining the running accuracy of a bearing. **Left:** A bearing with no play (or an interference fit) has all rolling elements loaded and wears and heats up excessively. **Center:** A bearing with standard play in the free state has low rigidity and rolling elements can slide instead of rotating. **Right:** A standard bearing with proper preload applied will provide system rigidity, optimal bearing life, and reduced vibration. [34]

7.2. CAD

The CAD model of the mechanism is made in a parametric manner. A certain set of parameters are established (like L_a, L_b, parallelogram length, ball bearing inner and outer diameter, link width, etc.) so as to define all the the dimensions of the different parts of the mechanism. Modifying the values of these parameters will therefore update the model to reflect the changes. This ensures congruence between the MATLAB model and the CAD model, and enables quick and accurate iteration of the link lengths or model parameters with the goal of reaching optimal link lengths while taking into account the new constraints or opportunities that become apparent when modelling the mechanism in CAD.

Experience within SRON says that aluminum is the most suitable material for links and brackets. Copper could be used due to its higher thermal conductivity however the ball bearings in the joints have a low thermal conductivity and act as the limiting link in the chain, whereby the copper no longer provides benefit. Flexible copper braids called *thermal straps* will likely have to be attached to different parts of the mechanism to serve as the thermal interface. Steel could also be considered, however aluminum is strong enough and results in a lighter weight mechanism and therefore also lower torque requirements.

The mechanism presented within this chapter has: parallelogram length 100 mm, L_a 40 mm, L_b 41 mm, 5×5 mm link cross section, ball bearing outer diameter (OD) 7 mm and 3 mm inner diameter (ID), 3 mm of material surrounding the OD press fit of the bearings, and 0.5 mm of spacing in between the links to avoid scraping. The MATLAB model shows that the L_a, L_b and link dimensions applied lead to a WS with 5 mm margins and an optical obstruction margin of 6 mm over the 55×25 mm optical WS. As the CAD model of the 55×25 mm LVF does not exist, the CAD model of the 40×20 mm LVF is used.

7.2.1. Overview

Shown in Figure 7.7a is an overview of the mechanism and how it fits into the cryostat. The cryostat is shown with a section view, its ceiling removed, and representations of the focused F/20 and collimated beams. Figure 7.8 shows an overview of the mechanism and how it fits within the BIORAD. The CAD model of the mechanism consists of: the 7 links of the mechanism (3 L_a links, 3 L_b links and one parallelogram link), 4 axles for in the three elbow joints and the joint at the base of the parallelogram arm, a floor bracket which serves as the interface between the floor of the cryostat and the connection points of the bases of the different arms of the mechanism, and an LVF bracket which serves as the interface between the LVF and it holder and the mechanism.

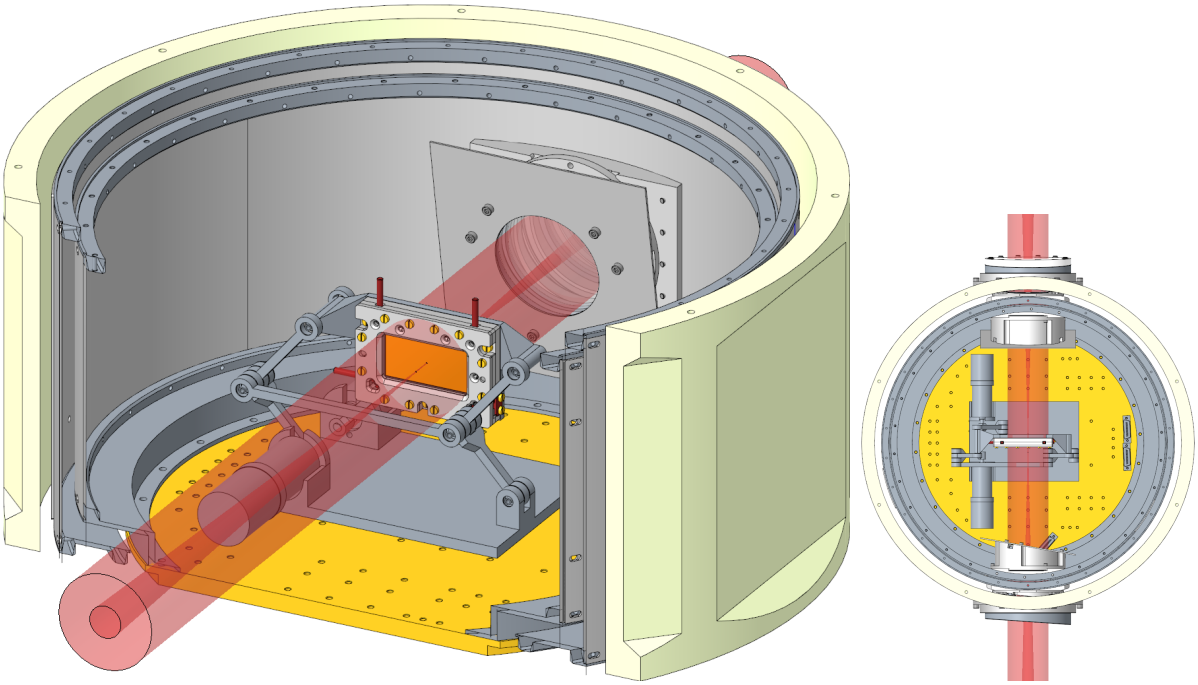

(a) A view into the cryostat.

(b) A top view of the cryostat.

Figure 7.7: Overviews of the mechanism within the cryostat.

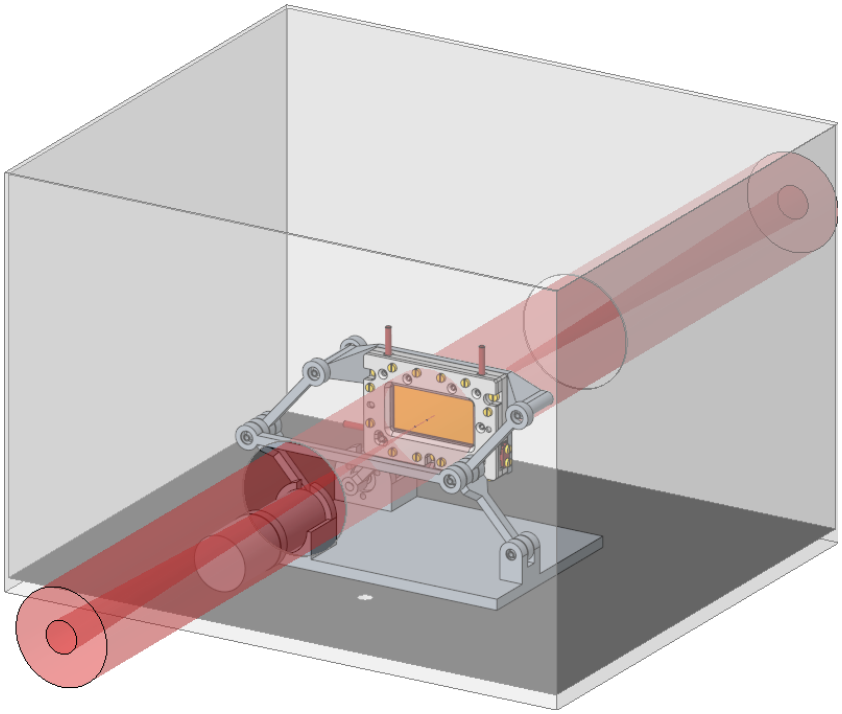

Figure 7.8: A view into the BIORAD

The mechanism is capable of scanning the 40 × 20 mm optical area of the LVF (Figure 7.9), provide an unobstructed position centered over the window to complete the collimated measurement (Figure 7.10a), and is able to provide an unobstructed OOB position (Figure 7.10b).

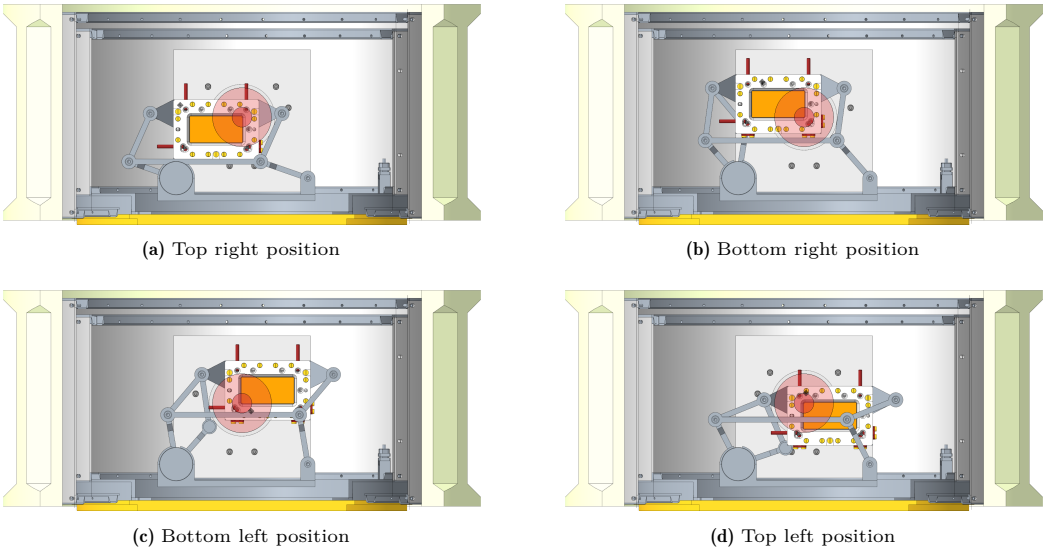

(a) Top right position

(b) Bottom right position

(c) Bottom left position

(d) Top left position

Figure 7.9: The scanning of the 40 × 20 mm optical area of the LVF.

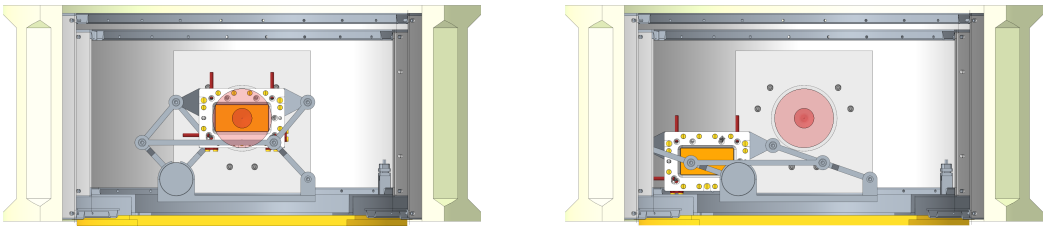

(a) Collimated position

(b) OOB position

Figure 7.10: The collimated and OOB positions of the mechanism.

7.2.2. LVF Bracket

The LVF bracket interfaces with the 3 bolts that make up the mechanical interface of the LVF holder, shown in Figure 7.11. Those three bolts pass through the LVF holder, and screw into the holes in the LVF bracket that are tapped, or are secured with a nut on the other side of the LVF bracket. On the sides of the LVF bracket are the three points where the arms of the mechanism connect. These connection points are brought sufficiently far out to avoid crashing between the arm joints (as they are the thickest part of the mechanism) and the LVF holder. The distance between these connection points must also be equal to the parallelogram length. The parallelogram length of 100 mm was chosen to ensure no optical obstruction in the centered collimated position, however it was also ensured that this parallelogram length was sufficient to be able to fit the large LVF within while still keeping sufficient room on the sides for the material required to create arm connection points.

The ball bearings get their ID pressed over the pins that extend from the bracket. These pins have a shoulder at their base which act as the end-stop of the bearing press-fit. These shoulders ensure that the OD of the pressed ball bearing does not rub against the bracket when the mechanism moves, and are essential to allow for preloading of the bearing. After the ID of the bearing is pressed onto the LVF bracket, the link is pressed over the OD of the bearing. Once again, a shoulder present in the link acts as an end-stop for the press-fit. Subsequently, a bolt with a washer is fastened into the tapped hole that is present in the pin of the bracket. Fastening this bolt ensures that the bearing and link are kept captive, and ensure preloading of the bearing. As the bolt is tightened, the shoulder on the OD presses

the bearing into the ID shoulder. This preloads the bearing and ensures greater running accuracy, as shown earlier in Figure 7.6. This bolt must be vented as to allow the gas trapped in the blind hole to easily escape when then vacuum is pulled in the cryostat. The washer can be a spring washer to ensure reliable force.

An intermediate bracket should still be made. Due to a shortage of time, this must be left as a recommendation. The bracket shown (which will be called the main bracket) should be dimensioned to interface with the large LVF. The small LVF must then interface with this larger main bracket through an intermediate bracket, which acts as the bridge between the interface of the small LVF and the interface of the LVF bracket. This is more favourable than designing two main brackets and alternating between those when a different sized LVF needs to be tested because the arms of the mechanism and the bearings are mounted onto the main bracket. Therefore, if the main bracket must be exchanged every time a differently sized LVF needs to be tested, the arms must be de-mounted from the bracket, resulting in unnecessarily complex work. Using an intermediate bracket allows the mechanism to remain in-tact at all time, where only the LVF with its intermediate bracket needs to be de-mounted.

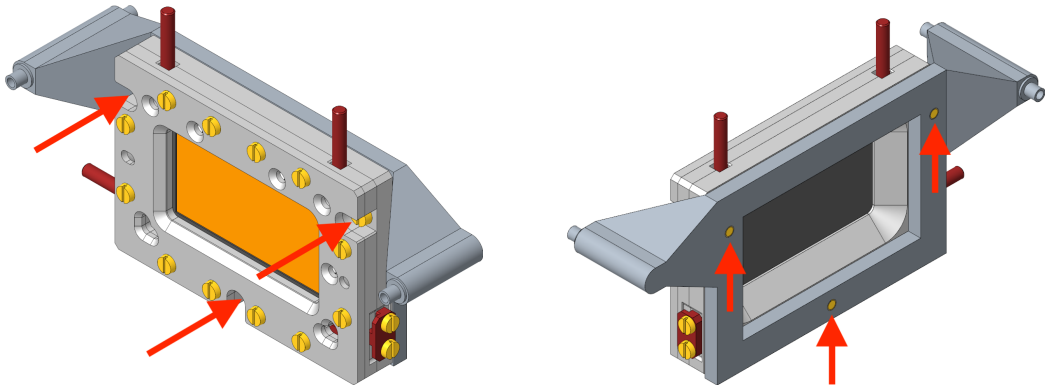

(a) Front **(b)** Rear

Figure 7.11: Isometric views of the LVF bracket, with the 3 bolts that form the mechanical interface between the LVF holder and the bracket marked with red arrows.

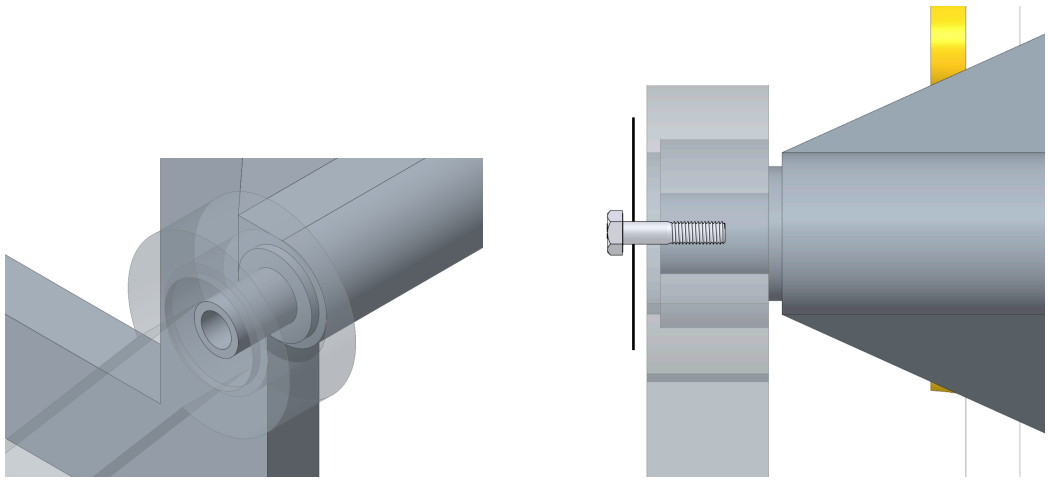

(a) Isometric view.

(b) Side view showing how the bolt screws into the tapped hole in the bracket. Bolt image retrieved from [35]

Figure 7.12: Detailed views of the ball bearing mounting point on the LVF bracket, and how the B-link of the mechanism (displayed with reduced opacity) interfaces with the mounted ball bearing.

7.2.3. Floor Bracket

The floor bracket is the interface between the floor of the cryostat and the base of the three arms of the mechanism. The base of the parallelogram arm is supported using a fork-head containing two press-fitted bearings. The motors are mounted using the manufacturer specified mechanical interface consisting of three holes tapped into the the motors. The motor body does not come in contact with the surrounding (circular) bracket material. This ensures that the motor's position and orientation are determined solely by the contact surface of the mechanical interface and the three securing bolts. The central axis of parallelogram arm base is at the same height as the central axis of the motors. The distance between the two in X-direction is one parallelogram length. The fork-head of the parallelogram arm base has a similar ball bearing solution as shown earlier in the LVF bracket: shoulders and a bolt to capture and preload the bearing. However, in this case an axle must be designed and incorporated. The design of this axle is similar to what will be detailed in the subsection below.

The floor bracket is unfinished, and improvements must be left as recommendations. Currently the floor bracket contains excess material. The large rectangular base serves only to rigidly connect the two motor brackets to the parallelogram arm bracket. This material poses no clear downside, and only serves to stiffen the connection between the motors and the parallelogram arm bracket. However, if desired, this material may be removed, given that the connection between the motor brackets and the parallelogram arm bracket remains sufficiently stiff.

Furthermore, as mentioned earlier, the system should have drop-in compatibility with both the cryostat and the BIORAD. The difference in optical height means that the floor bracket must be raised 10.25 mm off of the cryostat's floor. This offset should be created by mounting the floor bracket to the cryostat floor by means of leaf springs, which pose the additional benefit of mounting the floor in a near perfectly constrained manner. Figure 7.14 shows a schematic of how the leaf springs could be mounted to the floor of the cryostat and the floor bracket. A piece of spring steel (orange) is clamped to two solid blocks (blue) by means of bolts (green). This method of producing a mountable leaf spring is more cost effective than, for example, wire EDM, as it allows for the use of bulk sheet spring steel. The two solid blocks are consequently mounted by means of bolts to the floor (lower grey rectangle) and the top of the floor bracket (upper grey rectangle). Mounting to the *top* of the floor bracket (as opposed to the side or bottom) allows for longer leaf springs and therefore a higher compliance. Two possibilities exist for the configuration of the leaf springs. The most preferred method is to mount the bracket on 3 leaf springs situated in a circle around the center of the cryostat, positioned 120° apart from each other, and with their faces pointing towards the center. This is preferred due to the fact that, when in use and under vacuum, the floor of the cryostat will bulge slightly. Positioning the leaf springs symmetrically around this bulging will minimise its effect on the mechanism. Another mounting option is to position the leaf springs all pointing towards the thermal center of the bracket. The last mounting method is to mount one point of the bracket in a rigid, fixed, manner to the cryostat floor, and mount two leaf springs pointing towards this fixed point. This fixed point could be chosen to be placed in a location where it poses some benefit, like for example centered below the WS of the mechanism, to ensure this does not move with respect to the cryostat when it is cooled down.

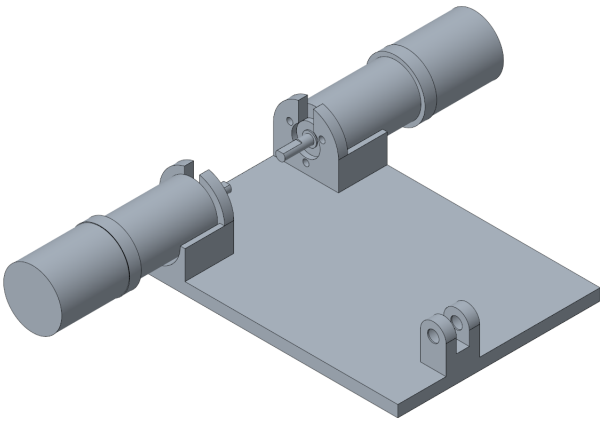

Figure 7.13: Isometric view of the floor bracket with the VSS stepper motors mounted.

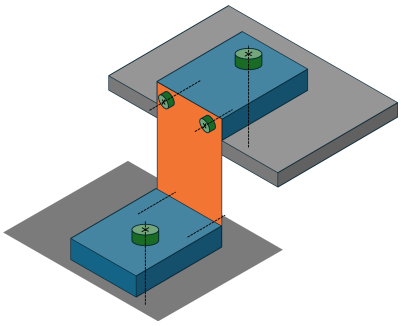

Figure 7.14: A schematic of how the leaf springs could be mounted to the floor bracket and the floor of the cryostat.

7.2.4. The Links

The L_a links are given a fork-head, or clevis, shape to increase the mechanisms stiffness into the plane. Due to there being a bearing situated in each side of the forked-head, the stiffness of the axle that passes through all the ball bearings is greatly increased against moments around the X-axis as it is supported on two sides. The design of the bearing housing is the same as previously, only repeated multiple times. The OD's of the four bearings are pressed into the housings in the links, where they encounter a shoulder. Subsequently the axle is pressed onto the ID's of the bearings, where once again there are shoulders present. As before, as the bolt is tightened the bearings are kept captive and are preloaded. The current design however possesses numerous drawbacks that make it not suitable.

The axle is made as a stepped axle to avoid needing to press an axle all the way though so many bearings. A stepped axle only requires each section of the axle to be pressed into its accompanying bearing. However, this would require the boring out of the ID of every bearing except the right most bearing, or selecting bearings with differing IDs. The boring out of the ID severely limits the possible height of the ID shoulders, and also effects the structural integrity of the bearings. A possible solution for this is to allow for bearings to be pressed over the entire axle. The ID of the bearings and the diameter of the axle can be iteratively bored and machined until they mate near perfectly, allowing for a very light press fit. The ID shoulders can be provided for by external snap (or retaining) rings that are installed after the pressing of the bearings over the axle.

The OD shoulders in the fork head are challenging to manufacture. The shoulder on the left can not be reached by a drill (or similar tool) without that same drill removing the material of the OD shoulder on the right. A possible way to manufacture this part is to use a boring bar, where the cutting head is sufficiently offset in order to be able to reach through the right shoulder and cut away at the surface where the beating's OD would sit. Depending on the height of the shoulder, this tool may have to be custom made. After drilling and boring the smaller diameter hole through the entire fork-head, this tool can be used to bore out the material in both heads of the fork to the OD of the bearing, leaving the shoulders in tact, as shown in Figure 7.17. Another solution is to create the shoulder by means of an internal snap ring. An internal groove must then be cut for the snap ring to be seated in.

The location of the B-link (the link inside the fork-head) is not defined. Imagine that press fit of the axle onto the bearing in the B-link is loose. The B-link is able to walk to the left, over its axle section. This is not the case for any other link: the fork head acts as the fixed world and does not move, and the parallelogram link is held captive by its ID shoulder on the axle and the washer which is connected to the fixed world through the axle. One possible solution for this is to install an external snap ring around the axle in the space between the B-link, and the left head of the fork. This snap ring could be installed at the end of the assembly process. A groove would need to be cut in the axle to serve as the seat for the snap ring. This snap ring ensures the capture of the B-link.

Interference between the parallelogram link and the motor axle or motor bracket may be a concern or limitation. When in the OOB position the parallelogram link must be able to reach a low position, as shown in 7.10b. This poses several interference challenges. Currently the parallelogram link is placed outside the fork-head as to avoid interference with the left A-link: the further OOB the mechanism goes, the more horizontal the arms become. If the parallelogram link was inside the fork-head of the left A-link, at a certain point there would be interference. However, when placed outside the fork-head, the parallelogram link may crash into the motor bracket. Looking at the elbow joint in Figure 7.16, the wider the arms are and the wider the bearings are, the more the parallelogram link is pushed to the left, and more over the motor and motor bracket. Therefore, if the parallelogram link is placed outside the fork-head, a limitation is placed on the the thickness of the links and bearings. Placing the parallelogram link inside the fork-head is recommended, as the limitation placed on the total width of the elbow joint is to severe. A relief channel may need to be cut in the trapezoidal widening section of the A-link, or the A-link can be given a U-shape as shown in Figure 7.18. This allows the A-link to be near horizontal without interference from the parallelogram link. The most horizontal reachable position is then limited only by interference between the parallelogram link and the motor axle (shown as a black circle).

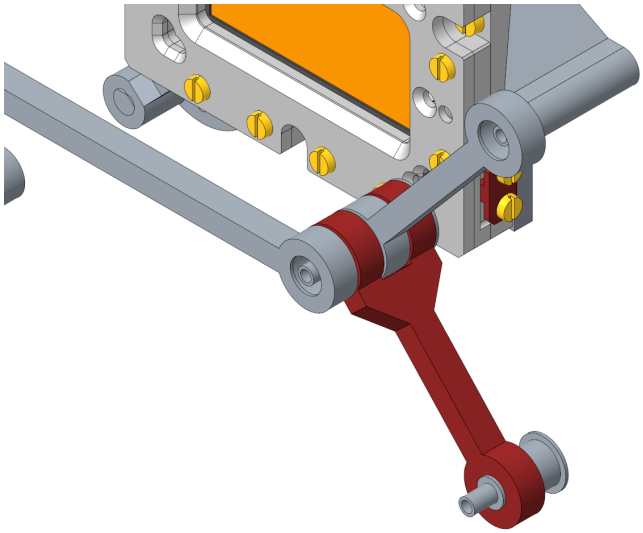

Figure 7.15: An example of the fork-head, or clevis, shape of the A-links. The A-link is highlighted in red.

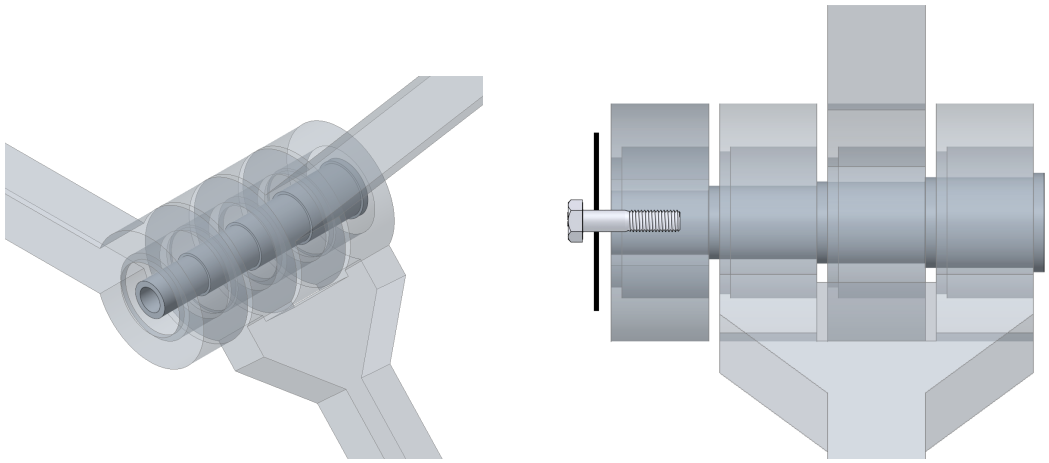

(a) Isometric view.

(b) Side view showing how the bolt screws into the tapped hole in the axle. Bolt image retrieved from [35]

Figure 7.16: Detailed views of how the ball bearings mount within the links, and how the axle sits within the ball bearings.

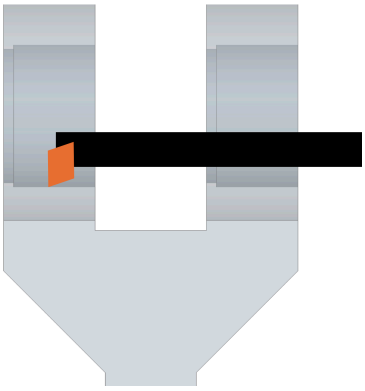

Figure 7.17: A boring bar may be able to cut the OD seat of the bearing while leaving the right shoulder in tact.

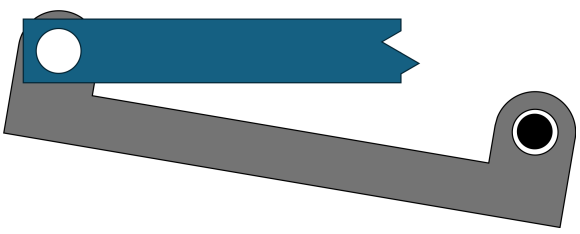

Figure 7.18: A U shape of the A-link can eliminate interference between it and the parallelogram link. Allowing the most horizontal reachable position to be limited only by interference of the parallelogram link and the motor axle (shown as a black circle).

8 Conclusion

In conclusion, a mechanism was designed based on a 5-bar linkage with a parallelogram to constrain the rotation of the LVF. The mechanism is driven by two stepper motors to ensure the lowest possible dissipation. The recommended stepper motor is a Phytron VSS 25.200.0.6 motor with attached VGPL22 (245 ratio, standard backlash) gearbox, who's detent torque is 12.6 times greater than the largest torque requirement of the mechanism. An estimation for the expected dissipation was made based on [21], placing the estimate at 38.8 mW, approximately four times larger than the target requirement. While the target requirement was not met, no design exists that is lower dissipation than a stepper motor where the detent torque is sufficient to support the mechanism. No steps taken along the way could have resulted in a significantly lower dissipation system than what has been recommend.

A MATLAB model was used to search through the design space to reach an optimal combination of link lengths. The use of flexpivots was discovered to be infeasible, and therefore ball bearings must be employed in the joints. The final link length combination (L_a 40 mm, L_b 41 mm, L_c 0 mm), paired with a parallelogram length of 100 mm is capable of all three (focused, collimated, and position-scan) measurement modes. The mechanism is able to scan the entire surface of a 40×20 mm LVF with a step size smaller than or equal to the target requirement of 25 µm. This was not feasible for the larger 55×25 mm LVF. The final link length combination was optimized as to maximise the area of the larger LVF for which small enough steps were able to be taken. In total 5.8 % of the surface of the larger LVF can not be stepped at 25 µm while using full steps of the stepper motor. 25 µm steps can still be achieved within this failing region through the use of microstepping, however this comes at the cost of increased dissipation. Furthermore, the time required to move the mechanism from the out-of-the-beam position to the furthest away position, is approximately 32 s; 5.5 times slower than the target requirement of 6 s. The time required to move from the out-of-the-beam position to the average position, is 15 s; 2.5 times slower than the target requirement.

A Monte Carlo tolerance analysis was conducted, resulting in the conclusion that using ball bearings with a maximum runout of ±0.75 µm, measuring the lengths of the links to ±2 µm, and manufacturing the links together, in a stack, is required to be 95 % confident that the manufactured mechanism will approach the ±2.5 µm metrology requirement. With the mentioned tolerances, it is 95 % confident that, while scanning the optical surface of the LVF, the uncertainty in its position will not exceed ±2.5 mm in X direction, and ±2.9 mm in Y direction. Additionally, the stepper motor has an uncertainty of ±5 % on its full steps, leading to a worst case uncertainty in LVF position due to uncertainty in the motor angle of ±2.4 µm. This results in a total 95 % certain worst case position uncertainty of ±4.9 µm in X, and ±5.3 µm in Y.

The theoretical mechanism was materialised into a CAD model which verifies the results from the MATLAB model, demonstrating that the mechanism is capable of a sufficient range of motion to scan the optical area of the LVF and move the LVF and mechanism arms out of the collimated beam. The mechanism is compatible with both the cryostat and BIORAD: it fits within both, and addresses the 10.25 mm difference in optical height by mounting the mechanism on leaf springs when inside the cryostat. Lastly, the bearing housings in the joints of the mechanism are designed as to allow for preloading of the bearings to increase running accuracy.

Given the design goals, targets and constraints, the mechanism identified in this thesis shows significant promise, and meets or nears the different target requirements. The design was thoroughly analyzed, considering performance, tolerances and manufacturability. Necessary trade-offs were made in prioritizing certain functions or requirements over others. The design presented within this thesis is believed to reach an optimum, striking the balance between cost, simplicity, performance, and manufacturability, forming an optimal design that satisfies the maximum requirements possible within the constraints set.

9 Recommendations

9.1. MATLAB Model

Two improvements can be made to the MATLAB model to facilitate a more comprehensive optimization of the triplets.

Firstly, the parallelogram length was picked via trial-and-error. Making the parallelogram length a design variable (like L_a, L_b, and L_c) would allow for it to be optimized like the rest, thereby eliminating the need for manual intervention and a trial-and-error approach.

Secondly, implementing the WS calculations (like motor torque, joint flexion, and optical obstruction) within the pink OOB area from Figure F.17 would allow the heatplots to extend into the OOB area and enable the optimization process to consider the OOB position. Currently, OOB obstruction is evaluation manually. However, if the WS sweep is implemented for the pink OOB area, this would no longer be necessary. Series flexpivot compatibility could also still be evaluated. This would allow for the generation of an UpSet plot showing whether or not series flexpivots were made viable due to the reduction in rectangular ROM, and whether or not the flexpivot compatible triplets intersect with the other requirements.

Incorporating these two improvements ensures a thorough evaluation and optimization of the mechanism, leading to an comprehensive optimization process that looks into every aspect of the design space and mechanism performance for potential optima.

A more comprehensive investigation into series flexpivots compatibility may be beneficial. This is particularly relevant considering the potential drawbacks of cryogenic high-accuracy ball bearings, which may be costly and have a limited lifespan. Additionally, flexpivot range of motion could be increased beyond the limits explored in this thesis. Allowing for a non-infinite life expectancy (as shown in Figure F.8) increases the allowable angular stroke of the flexpivot.

9.2. Tolerance Analysis

Convergence of the Monte Carlo simulation was evaluated through trial-and-error. Convergence of the Monte Carlo simulation is a function of both the WS grid resolution, and the number of Monte Carlo iterations. While confidence in the convergence of the Monte Carlo simulation is high, a more comprehensive convergence analysis could be conducted. This analysis would involve the generation of surface plots, where the X and Y axes represent the WS resolution and the number of iterations. The Z-axis would correspond to the error in the X, Y and angle of the LVF. This approach would provide a more detailed understanding of the simulation's convergence behavior.

Currently, in the tolerance analysis, the same tolerance is applied to every link. However, this approach does not allow for the investigation of the influence of a single link's tolerance on the error in LVF position. The mechanism may exhibit greater sensitivity to tolerances and perturbations in some links than others. Investigating the per-link sensitivity could allow for the imposing of different tolerances for the different links, allowing for larger tolerances to be applied on the less sensitive links.

The effect that the 5 % uncertainty in motor drive angle has on the error in LVF position, has only been calculated for the worst-case-scenario: perturbed by the maximum 5 % at the point in the WS that is the most sensitive to motor drive angle. However, similarly to the manufacturing tolerances, the effect it has on the error in LVF position will vary over the WS. Furthermore, the error in drive angle will not always be the worst case 5 % error, but may follow a normal distribution. Therefore, to more accurately calculate the expected error in LVF position at each point within the WS, the error due to a normally distributed perturbed drive angle must be calculated across the WS, and summed with the existing error in LVF position caused by manufacturing and ball bearing tolerances.

In the current Monte Carlo tolerance analysis, only the largest error within the WS has been investigated. It may be interesting to investigate the average error over the WS, and the standard deviation of the errors over the WS. This may help to provide more insight into the errors in the system, providing information beyond only the worst-case scenario.

9.3. Design

Some recommendations for the design have been addressed previously in Chapter 7.2. These include: the addition of an intermediate bracket for LVF mounting; improvements to the floor bracket and the addition of the leaf springs to mount it on; changes to the axle design; changes to the design of the OD shoulders to aid the challenging manufacturing; the undefined location of the B-link; and interference between the parallelogram link and motor bracket or A-link. Aside from these recommendations, there are other additions that may prove beneficial to implement in the design of the mechanism which will be addressed below.

A backlash elimination system may be necessary to implement. A common method to mitigate the effect of backlash is to always approach a position from the same side. For instance, when positioning the LVF in the WS, to always approach that position from the left. This is the case within this mechanism. Between every measurement, the LVF is moved to the OOB position, whereafter it is once again brought into the WS, thereby always approaching from the same side. However, this method of backlash mitigation only works if there are no external forces present, of if the net external force works to push the object back to where it came form. In the case of the LVF, there is the external gravitational force, and this force does not work to bring the LVF to it's OOB position. Therefore this method of backlash mitigation may not result in the desired results, and a backlash elimination system may need to be implemented. This system can be as simple as attaching a constant force coil spring to the A-links of the left and right arms. The force provided by the spring should be tuned as to be sufficient to overcome any backlash while still remaining minimal, as to not absorb too much of the torque budget. The minimum torque required to overcome backlash in the stepper motor-gearbox combination may be retrieved from Phytron. The maximum torque required by the mechanism is known, as is the maximum detent torque of the stepper motor. Therefore, the torque exerted by the spring must not exceed the difference between these two values, as to not exceed the motor torque budget.

A rotary encoder or resolver can be applied to the two driving A-links of the mechanism in order to increase the positioning accuracy. This would bypass the ± 1.271 arcseconds uncertainty in link angle caused by the 5 % tolerance on the motor step angle. Additionally, this would bypass any backslash in the system, as the angle of the links is directly measured. Furthermore, currently the position of the mechanism is determined by counting the steps taken by the stepper motor. However, if the stepper motor misses a step, the mechanism will no longer be where it is believed to be. A stepper motor missing a step may be caused by insufficient torque, or a too rapid acceleration/deceleration. Due to the very large safety factor on the torque of the motor over the maximum torque required by the mechanism, and the low maximum allowable speed of 100 rpm, the stepper motor missing steps is not seen as a very large threat. However it may still occur, and employing an encoder or resolver eliminates any possibility of this threat by directly measuring the angle of the links.

It may be possible that during testing of the mechanism it is discovered that the errors in LVF position are larger than predicted within this thesis. This may be due to sources of error that were not accounted for within this thesis. If the errors are unacceptably large, and reducing them is infeasible, the implementation of feedback control may become necessary. A potential solution for the precise and direct measurement of the X,Y position of the LVF may be a 2-DOF planar interferometry setup. However, very little research has been conducted into this for this thesis, thus it remains merely a preliminary suggestion.

It may be desirable to implement physical end-stops for the driving A-links. In the case of a malfunction, physical end-stops would act to limit the angular range of the A-links, thereby preventing (or at least minimizing) potential collisions or damage to the LVF or other vital components.

Lastly, the into-the plane stiffness of the final design should be evaluated in order to validate the tip, tilt, and piston requirements.

9.4. General

After the mechanism has been manufactured and assembled, its performance must be verified and characterized in order to be able to commission it. In essence, the X, Y location of the LVF must be measured, and compared to the expected location. The accuracy of this measurement must be approximately on the order of 1 µm, as it must be significantly smaller than the ±2.5 µm metrology requirement of the mechanism. A non-contact technique capable of measurements of this accuracy is laser interferometry. Linear encoders or Linear Variable Differential Transformers (LVDTs) can also be used. However, these would require mounting to the LVF (or a dummy LVF) and to the fixed world, with some intentional slack as to not effect (and overconstrain) the positioning of the mechanism. For this reason, an interferometric setup is preferred.

Plain bearings may prove to be a suitable alternative to ball bearings, due to their reduced cost and smaller size. Plain bearings are typically only suitable to low-speed applications, which is the case for the mechanism presented within this thesis. Research into the accuracy or runout of plain bearings proved to be challenging, and the accuracy that can be expected from a plain bearing remains uncertain. If the accuracy falls within the ±0.75 µm range required, plain bearings could prove to be a cost-effective and space-efficient alternative to ball bearings.

In hindsight, concept 3.4, series mounting of two Onnes piezo stages, may have been the simplest, smallest and most accurate concept. Onnes piezo stages offer a positioning repeatability of 10 nm, with built-in position sensing and feedback [36]. Implementing a constant force spring to gravity balance the LVF would alleviate potential shortcomings in the actuator's maximum force. The dissipation may also be low, stated on the website to be 10 µW, however this is likely to be a best-case value and would need to be verified for this application. Onnes piezo stages are however fragile, as well as costly; more costly than Phytron stepper motors. However, the price of the high accuracy and cryogenically compatible ball bearings should not be neglected; it may lead to the total cost of the two systems being comparable.

References

[1] Jason Glenn et al. *PRIMA: The PRobe far-Infrared Mission for Astrophysics*. Tech. rep. 2023. URL: https://ntrs.nasa.gov/api/citations/20230000090/downloads/Glenn_PRIMA_AAS_Poster.pdf.

[2] PRIMA Team. *PRIMA: The PRobe far-Infrared Mission for Astrophysics*. URL: https://prima.ipac.caltech.edu.

[3] Weibo Chen et al. "PRIMA space telescope cryocooling system". In: *Infrared Sensors, Devices, and Applications XIII*. Ed. by Ashok K. Sood, Priyalal Wijewarnasuriya, and Arvind I. D'Souza. SPIE, Oct. 2023, p. 6. ISBN: 9781510665880. DOI: 10.1117/12.2675697.

[4] Arvin Emadi et al. "Design and implementation of a sub-nm resolution microspectrometer based on a Linear-Variable Optical Filter". In: *Optics Express* 20.1 (Jan. 2012), p. 489. ISSN: 1094-4087. DOI: 10.1364/OE.20.000489.

[5] D.W. Ball. *Fabry-Perot Interferometer*. 2006. URL: https://spie.org/publications/spie-publication-resources/optipedia-free-optics-information/fg08_p32_fabry-perot_interferometer.

[6] Mark O. Kimball and Eric A. Silk. *Introduction to Liquid Helium*. 2014. URL: https://cryo.gsfc.nasa.gov/introduction/liquid_helium.html.

[7] IRLabs. *LN2 Dewars and Dewars for Other Liquid Cryogens*. URL: https://www.irlabs.com/products/cryostats/liquid-cryogen-dewars/.

[8] Phytron. *VSS/VSH Stepper motors for operation in vacuum or space or for cryogenic application*. URL: https://www.phytron.eu/products/motors-actuators/vss-vsh/.

[9] THORLABS. *Voice Coil Actuators*. URL: https://www.thorlabs.com/newgrouppage9.cfm?objectgroup_id=14116.

[10] THK. *Features of the Ball Screw*. URL: https://tech.thk.com/en/products/pdf/en_b15_006.pdf.

[11] The University of Utah. *Ball Screw Selection and Calculations*. URL: https://my.mech.utah.edu/~me7960/lectures/Topic4-BallscrewCalculations.pdf.

[12] C-Flex. *Pivot Bearing Design Guide*. Tech. rep. URL: https://c-flex.com/pivot-bearings/design-guide/.

[13] K. G.P. Folkersma et al. "A 2-DOF Large Stroke Flexure Based Positioning Mechanism". In: *Proceedings of the ASME Design Engineering Technical Conference* 4.PARTS A AND B (Sept. 2013), pp. 221–228. DOI: 10.1115/DETC2012-70377.

[14] Lucas Campos et al. "Development of a Five-Bar Parallel Robot With Large Workspace". In: *Volume 2: 34th Annual Mechanisms and Robotics Conference, Parts A and B*. ASMEDC, Jan. 2010, pp. 917–922. ISBN: 978-0-7918-4410-6. DOI: 10.1115/DETC2010-28962.

[15] Jong-Won Kim, TaeWon Seo, and Jongwon Kim. "A new design methodology for four-bar linkage mechanisms based on derivations of coupler curve". In: *Mechanism and Machine Theory* 100 (June 2016), pp. 138–154. ISSN: 0094114X. DOI: 10.1016/j.mechmachtheory.2016.02.006.

[16] Eric W. Weisstein. *Circle-Circle Intersection*. URL: https://mathworld.wolfram.com/Circle-CircleIntersection.html.

[17] Paul Bourke. *Circles and spheres: Intersection of two circles*. URL: https://paulbourke.net/geometry/circlesphere/.

[18] Tuong Hoang, Trung Vuong, and Bang Pham. "Study and Development of Parallel Robots Based On 5-Bar Linkage". In: *National Conference on Machines and Mechanisms*. Ho Chi Minh City, 2015. URL: https://www.researchgate.net/publication/283356024.

[19] Djana Ilia and Rosario Sinatra. "A novel formulation of the dynamic balancing of five-bar linkages with applications to link optimization". In: *Multibody System Dynamics* 21.2 (Mar. 2009), pp. 193–211. ISSN: 1384-5640. DOI: 10.1007/s11044-008-9134-2.

[20] Morskate. *Morskate | Drive Technology | Morskate Aandrijvingen BV*. URL: https://www.morskatedrivetechnology.com/.

[21] C de Jonge et al. "Cryogenic actuator testing for the SAFARI ground calibration setup". In: *Modern Technologies in Space- and Ground-based Telescopes and Instrumentation II*. Ed. by Ramón Navarro, Colin R Cunningham, and Eric Prieto. Vol. 8450. SPIE, 2012, p. 84504D. DOI: 10.1117/12.927095.

[22] ISO 492:2023(E). *Rolling bearings - Radial bearings - Geometrical product specifications (GPS) and tolerance values*. Tech. rep. Sept. 2023.

[23] GMN Bearing. *What is Bearing Preload?* URL: https://www.gmnbt.com/resources/guides/ball-bearing/ball-bearing-preload/.

[24] HQW. *HQW Precision: Super precision miniature ball bearings*. URL: https://www.hqw.gmbh/.

[25] Inc. New Hampshire Ball Bearings. *Miniature & Instrument Ball Bearings*. URL: https://www.nhbb.com/products/miniature-instrument-ball-bearings.

[26] National Precision Bearings. *Miniature Bearings*. URL: https://www.nationalprecision.com/products/c/miniature-bearings/.

[27] Carter Manufacturing. *Cryogenic Bearings*. URL: https://www.carterbearings.co.uk/bearings/cryogenic-bearings#enquiry-form.

[28] UNASIS. *Custom Cryogenic Bearings*. URL: https://www.unasisbearings.com/industries/cryogenics.

[29] CEROBEAR. *Upgrade your pump performance*. URL: https://www.cerobear.com/applications/cryogenic-industry/.

[30] Myonic GmbH. *Ball Bearings*. URL: https://myonic.com/ball-bearings/.

[31] Barden Bearings. *Super Precision, Superior Performance*. URL: https://www.bardenbearings.co.uk/.

[32] Fridman Mekanik. *High precision miniature ball bearing*. URL: https://www.fridman.com/en/product/593/.

[33] National Institute of Standards and Technology (NIST). *Material Properties: 6061-T6 Aluminum (UNS A96061)*. URL: https://trc.nist.gov/cryogenics/materials/6061%20Aluminum/6061_T6Aluminum_rev.htm.

[34] National Precision Bearing. *Bearing Preload*. URL: https://www.nationalprecision.com/info-library/technical-data/bearing-preload/.

[35] pngkey. *Hex bolt*. URL: https://www.pngkey.com/maxpic/u2r5y3q8y3y3u2r5/.

[36] Onnes Technology. *arQtika LCW: Cryogenic nanopositioner utilizing walking piezo technology for low temperature environments*. URL: https://onnestechnologies.com/products/arqtika/.

[37] Amro Shafik and Ridha Ben Mrad. "Piezoelectric Motor Technology: A Review". In: *Nanopositioning Technologies*. Cham: Springer International Publishing, 2016, pp. 33–59. DOI: 10.1007/978-3-319-23853-1{_}2.

[38] PiezoMotor. *The PiezoMotor Technology*. URL: https://piezomotor.com/technology/.

[39] Johan H. Pragt et al. "Piezo-driven adjustment of a cryogenic detector". In: ed. by Eli Atad-Ettedgui and Dietrich Lemke. July 2008, 70184N. DOI: 10.1117/12.788396.

[40] S Mohith et al. "Recent trends in piezoelectric actuators for precision motion and their applications: a review". In: *Smart Materials and Structures* 30.1 (Jan. 2021), p. 013002. ISSN: 0964-1726. DOI: 10.1088/1361-665X/abc6b9.

[41] Michail E. Kiziroglou et al. "Micro Motion Amplification–A Review". In: *IEEE Access* 8 (2020), pp. 64037–64055. ISSN: 2169-3536. DOI: 10.1109/ACCESS.2020.2984606.

[42] Johann Tang and Oriental Motor. *Stepper Motor Basics: PM vs VR vs Hybrid*. 2021. URL: https://blog.orientalmotor.com/stepper-motor-basics-pm-vs-vr-vs-hybrid.

[43] Dietrich Lemke et al. "Cryomechanisms for positioning the optical components of the mid-infrared instrument (MIRI) for NGST". In: *https://doi-org.tudelft.idm.oclc.org/10.1117/12.461498* 4850.5 (Mar. 2003), pp. 544–555. ISSN: 0277786X. DOI: 10.1117/12.461498.

[44] Jan Kragt et al. "MATISSE selection mechanism development". In: ed. by Ramón Navarro, Colin R. Cunningham, and Eric Prieto. Sept. 2012, 84504E. DOI: 10.1117/12.926602.

[45] Oriental Motor. *Basics of Stepper Motors*. URL: https://www.orientalmotor.com/stepper-motors/technology/stepper-motor-basics.html.

[46] M Eggens et al. "Optimization and verification of a brushless DC-motor for cryogenic mechanisms". In: *15th European Space Mechanisms and Tribology Symposium*. Sept. 2013. URL: https://esmats.eu/esmatspapers/pastpapers/pdfs/2013/eggens.pdf.

[47] Miles Budimir. *Comparing stepper and brushless dc motors*. URL: https://www.motioncontroltips.com/comparing-stepper-and-brushless-dc-motors/#:~:text=Steppers%20lack%20the%20ability%20to,across%20a%20wide%20speed%20range..

[48] E. Favre et al. "European electric space rated motors handbook". In: *8th European Space Mechanisms and Tribology Symposium*. 1999, pp. 159–164. URL: https://www.esmats.eu/esmatspapers/pastpapers/pdfs/1999/favre.pdf.

[49] InTraSys. *The principle of a linear motor*. URL: https://intrasys-gmbh.com/english/linear-drive-engineering/motors-principle/.

[50] Ahmet Okyay, Mir Behrad Khamesee, and Kaan Erkorkmaz. "Design and Optimization of a Voice Coil Actuator for Precision Motion Applications". In: *IEEE Transactions on Magnetics* 51.6 (June 2015), pp. 1–10. ISSN: 0018-9464. DOI: 10.1109/TMAG.2014.2381160.

[51] Guanqiao Shan et al. "Contributed Review: Application of voice coil motors in high-precision positioning stages with large travel ranges". In: *Review of Scientific Instruments* 86.10 (Oct. 2015). ISSN: 0034-6748. DOI: 10.1063/1.4932580.

[52] Xeryon. *Voice coil actuators vs Linear Motors vs Ultrasonic piezo actuators*. URL: https://xeryon.com/voice-coil-actuators-vs-linear-motor-vs-ultrasonic-piezo-actuators/.

[53] Power Transmission Engineering. *What is a Voice Coil Actuator?* 2018. URL: https://www.powertransmission.com/blogs/4-editors-choice/post/Voice-Coil-Actuator.

[54] R Navarro et al. "Precision mechanisms for optics in a vacuum cryogenic environment". In: *https://doi-org.tudelft.idm.oclc.org/10.1117/12.2309124* 10565 (Nov. 2017), pp. 407–413. ISSN: 1996756X. DOI: 10.1117/12.2309124.

[55] E.W. Roberts. "Thin solid lubricant films in space". In: *Tribology International* 23.2 (Apr. 1990), pp. 95–104. ISSN: 0301679X. DOI: 10.1016/0301-679X(90)90042-N.

[56] JPE. *JPE Precision Point: 2 Leaf springs in parallel*. URL: https://www.jpe-innovations.com/precision-point/2-leaf-springs-parallel/.

[57] NIST. *Material Properties: 304 Stainless (UNS S30400)*. URL: https://trc.nist.gov/cryogenics/materials/304Stainless/304Stainless_rev.htm.

[58] C. R. Anoop et al. "A Review on Steels for Cryogenic Applications". In: *Materials Performance and Characterization* 10.2 (June 2021), pp. 16–88. ISSN: 2379-1365. DOI: 10.1520/MPC20200193.

[59] D. Farhadi Machekposhti, N. Tolou, and J. L. Herder. "A Review on Compliant Joints and Rigid-Body Constant Velocity Universal Joints Toward the Design of Compliant Homokinetic Couplings". In: *Journal of Mechanical Design* 137.3 (Mar. 2015). ISSN: 1050-0472. DOI: 10.1115/1.4029318.

[60] Larry L. Howell. "Compliant Mechanisms". In: *21st Century Kinematics*. London: Springer London, 2013, pp. 189–216. DOI: 10.1007/978-1-4471-4510-3{_}7.

[61] Larry L. Howell, Spencer P. Magleby, and Brian M. Olsen, eds. *Handbook of Compliant Mechanisms*. Wiley, Feb. 2013. ISBN: 9781119953456. DOI: 10.1002/9781118516485.

[62] Ellen I. Williams, Richard T. Summers, and Miroslaw A. Ostaszewski. *Flexure bearing*. URL: https://commons.wikimedia.org/wiki/File:Flexure_pivot.png.

[63] SmarAct. *Cryogenic Linear Stages - SmarAct*. URL: https://www.smaract.com/en/cryogenic-linear-stages.

[64] JPE. *Cryo Linear Drive*. URL: https://www.jpe-innovations.com/cryo-uhv-products/cryo-linear-drive/.

[65] Universal Cryogenics. *Universal Cryogenics*. URL: https://www.ucryo.com.

[66] Physik Instrumente. *M-414 Precision High-Load Linear Stage*. URL: https://www.physikinstrumente.com/en/products/linear-stages/stages-with-stepper-dc-brushless-dc-bldc-motors/m-414-high-load-precision-stage-701755.

[67] Niels Tromp et al. "MATISSE cold optics opto-mechanical design". In: 7734.21 (July 2010), pp. 617–628. ISSN: 0277786X. DOI: 10.1117/12.856973.

[68] Gabby Aitink-Kroes et al. "Realization and performance of cryogenic selection mechanisms". In: 9151 (July 2014), pp. 139–156. ISSN: 1996756X. DOI: 10.1117/12.2056803.

[69] Lorenza Ferrari et al. "Development and performance validation of a cryogenic linear stage for SPICA-SAFARI verification". In: ed. by Ramón Navarro, Colin R. Cunningham, and Allison A. Barto. July 2014, 91510E. DOI: 10.1117/12.2056567.

[70] P. Dieleman et al. "Development of a low background test facility for the SPICA-SAFARI on-ground calibration". In: ed. by Wayne S. Holland. Sept. 2012, 84521U. DOI: 10.1117/12.926873.

[71] Robert M Warden. "Cryogenic Nano-Actuator for JWST". In: *38th Aerospace Mechanisms Symposium*. May 2006, pp. 239–252. URL: https://esmats.eu/amspapers/pastpapers/pdfs/2006/warden.pdf.

[72] Jaroslav Hricko and Štefan Havlík. "Compliant Mechanisms for Motion/Force Amplifiers for Robotics". In: *Advances in Intelligent Systems and Computing* 980 (2020), pp. 26–33. ISSN: 21945365. DOI: 10.1007/978-3-030-19648-6{_}4/COVER. URL: https://link-springer-com.tudelft.idm.oclc.org/chapter/10.1007/978-3-030-19648-6_4.

[73] Fangxin Chen et al. "A review on the flexure-based displacement amplification mechanisms". In: *IEEE Access* 8 (2020), pp. 205919–205937. ISSN: 21693536. DOI: 10.1109/ACCESS.2020.3037827.

[74] Physik Instrumente. *Piezoelectric Actuators, Piezo Transducers*. URL: https://www.pi-usa.us/en/products/piezo-actuators-stacks-benders-tubes.

[75] Philipp Gräser et al. "High-precision and large-stroke XY micropositioning stage based on serially arranged compliant mechanisms with flexure hinges". In: *Precision Engineering* 72 (Nov. 2021), pp. 469–479. ISSN: 0141-6359. DOI: 10.1016/J.PRECISIONENG.2021.02.001.

[76] Shorya Awtar. "Synthesis and analysis of parallel kinematic XY flexure mechanisms". PhD thesis. Massachusetts Institute of Technology, 2003. URL: http://hdl.handle.net/1721.1/17945.

[77] Yunzhuang Chen, Leijie Lai, and Limin Zhu. "Structural design and experimental evaluation of a coarse-fine parallel dual-actuation XY flexure micropositioner with low interference behavior". In: *The Review of scientific instruments* 94.9 (Sept. 2023), p. 95006. ISSN: 10897623. DOI: 10.1063/5.0160760/2910843.

[78] J.L. Herder. "Energy-free systems: Theory, conception, and design of statically balanced spring mechanisms". PhD thesis. 2001. ISBN: 90-370-0192-0. DOI: 10.13140/RG.2.1.3942.8966. URL: http://resolver.tudelft.nl/uuid:8c4240fb-0315-462a-8b3b-efbd0f0e68b6.

[79] Teunis Van Dam, Patrice Lambert, and Just L. Herder. "Static Balancing of Translational Parallel Mechanisms". In: *Proceedings of the ASME Design Engineering Technical Conference* 6.PARTS A AND B (June 2012), pp. 883–889. DOI: 10.1115/DETC2011-47525. URL: https://dx-doi-org.tudelft.idm.oclc.org/10.1115/DETC2011-47525.

[80] Sangamesh R. Deepak and G. K. Ananthasuresh. "Static balancing of a four-bar linkage and its cognates". In: *Mechanism and Machine Theory* 48.1 (Feb. 2012), pp. 62–80. ISSN: 0094-114X. DOI: 10.1016/J.MECHMACHTHEORY.2011.09.009.

[81] Ezekiel G. Merriam et al. "The Design of a Fully Compliant Statically Balanced Mechanism". In: *Proceedings of the ASME Design Engineering Technical Conference* 6 A (Feb. 2014). DOI: 10.1115/DETC2013-13142. URL: https://dx-doi-org.tudelft.idm.oclc.org/10.1115/DETC2013-13142.

[82] Juan Li, Yanjie Liu, and Lining Sun. “A novel 2-DOF planar parallel robot with high accelerate / high precision”. In: *2007 IEEE International Conference on Robotics and Biomimetics (ROBIO)*. IEEE, Dec. 2007, pp. 2189–2193. ISBN: 978-1-4244-1761-2. DOI: 10.1109/ROBIO.2007.4522509.

Appendices

This page is intentionally left blank.

A Literature Review: Fundamental Cryogenic Components

This section provides an overview of the fundamental components of a cryogenic positioning system such as actuators, bearings and compliant joints, and evaluates their applicability to the LVF positioning system.

A.1. Actuators

A.1.1. Piezoelectric Actuators

Piezoelectric actuators convert electrical energy into displacement through using the piezoelectric strain effect. Typical strains are on the order of 0.1–0.2 % and therefore an amplification mechanism is often used to convert the small expansion of the piezoelectric material into larger displacements. Typically the maximum force ranges from single newtons to 100s of Newtons while some piezostacks can reach 10s of kilonewtons. Piezo actuators are backlash-free and sub-micrometer or sub-nanometer resolution is common [37]. This resolution is limited by the drive electronics, not the piezo actuator itself [38].

Amplification mechanisms can be structure-based, like shown in Figure A.1a, where a small elongation of the piezostack is amplified into a larger displacement at the output. Though, more interestingly, amplification can also be step-based using a stick-slip or walking principle like shown in Figure A.1b and A.1c. In stick-slip piezo amplification, during the stick phase, the actuator slowly extends, and the friction between the moving shaft and the floor causes the inertial mass to move forwards. Then, in the slip phase, the actuator rapidly contracts. The inertia of the mass allows the moving shaft to slide over the floor and move forwards. Walking-type piezos operate by using specific a arrangement and actuation cycle of multiple piezo actuators, resulting in a series of piezo-'legs' that grip and move a shaft in a sequence. Their working principle is best explained visually and is shown in Figure A.1c. These actuation principles are theoretically capable of infinite stroke, as long as the shaft being propelled has an infinite length. When compared to walking actuators, stick-slip actuators theoretically have higher power usage and heat generation due to their parasitic drag [21]. Furthermore, while piezo actuators exhibit low dissipation at room temperature compared to traditional electrical motors, this changes at cryogenic temperatures. The copper losses in electrical motors reduce by several orders of magnitude while piezo actuators only reduce by a factor of 5 [21]. Additionally the expansion of the piezo elements, as well as the force they can deliver, reduces as the temperature drops; at 4 K the remaining expansion capacity is around 5 % [39]. This results in the piezo actuator requiring a higher voltage (and therefore also higher dissipation) to produce the same performance [39]. Step-based amplification methods are capable of operating at cryogenic temperatures, but have been shown to be fragile, sensitive to jamming, and lacking in terms of repeatability performance; showing a scatter of around 25 % [39].

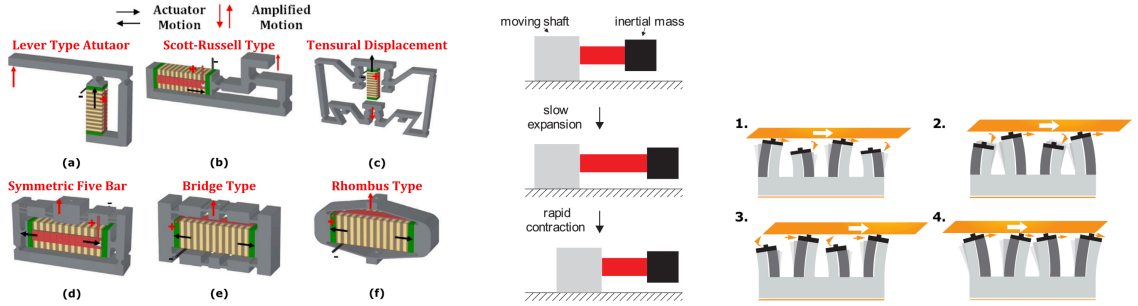

(a) Examples of flexure structures for piezo motion amplification; adapted from [40]

(b) Stick-slip piezo principle [41]

(c) Walking piezo principle [38]

Figure A.1: Three types of piezo amplification.

A.1.2. Stepper Motor

Hybrid stepper motors are a type of brushless DC electric motor that rotate in increments rather than continuously. They consist of two toothed permanent magnet rotors (one magnetized as the north pole, and the other as the south), which are surrounded by toothed stator poles wrapped in multiple phases of copper windings. Typically stepper motors take steps of 1.8°. Energizing the windings turns the stator poles and their teeth into electromagnets (north or south depending on the direction of the current through the winding) which in turn repel and attract the permanent magnet rotor to its next stable step. Energizing the windings in a specific sequence will result in the the motor taking consecutive steps. Figure A.2c shows the north pole magnetized rotor and phase A excited as a south pole. As phase A becomes deexcited and phase B becomes excited as a south pole, the rotor steps 1.8° to its next position as shown in Figure A.2d. This process repeats for $\overline{A}$ and $\overline{B}$ and so forth [42].

A key characteristic of stepper motors is their *detent torque*; their ability to produce a torque even while not powered, due to the permanent magnet rotor. This detent torque is generally many times less than the powered holding torque of the motor, however it is not zero and can still be used. If a system is designed as such that the detent torque is sufficient to hold position, the motor can be de-powered, resulting in an extreme reduction in average dissipation. Specifically regarding the LVF positioning system, for which a low duty cycle of 10 % is targeted, this means that the average dissipation of the motor will only be 10 % of its rated powered dissipation. Furthermore; detent torque can be used to aid the motor in making steps. If detent torque is sufficient, the motor can be powered during the first half of the step, allowing the self-restoring detent torque to finish the second half, resulting in even more dissipation gains [43]. Stepper motors are therefore very well suited for low duty cycle applications. Stepper motors are also capable of microstepping. This is where a single 1.8° step is split into up to multiple (often 256) microsteps through controlling the current in the windings. In microstep mode detent torque can not be used and the motor can not be de-powered as the motor is forcefully held in between its magnetic equilibrium positions through controlling the current in the windings. Within SRON, Phytron's VSS line of commercially available cryogenically rated stepper motors have been tested and used extensively. These motors can be purchased with a cryogenically rated gearbox to improve step resolution. Phytron's VSS steppers were the preferred actuator for a low duty cycle flipmirror used at SRON for the 4 K cryogenic on-ground calibration setup of the SAFARI instrument [21], and for the low duty cycle selection mechanisms for MATISSE developed by NOVA-ASTRON [44].

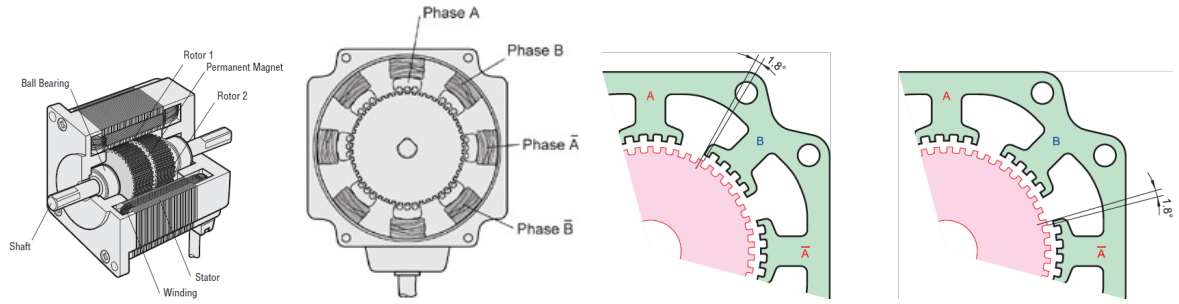

(a) A cutaway view [42] **(b)** A head on view [45] **(c)** Phase A excited position [42] **(d)** Phase B excited position [42]

Figure A.2: Detail of a stepper motor.

A.1.3. Brushless Direct Current Motor (BLDC)

BLDC motors are simple in their construction and have been researched, optimized and manufactured in house at SRON for SAFARI [46]. BLDC motors are capable of large torques, large range of speeds with low dissipation, high efficiency and high position accuracy and were the preferred motor to drive the ballscrew stages in SRON's on-ground calibration setup for the SAFARI instrument [21].

The construction of a BLDC involves a permanent magnet rotor and a set of stationary windings (the stator). The stator windings are energized in a sequence to create a rotating magnetic field, which interacts with the magnetic field of the rotor to generate torque. The position of the rotor in a BLDC is continuously monitored, often using Hall effect sensors. This feedback is used to adjust the timing of the stator winding energization. [47]

BLDC motors and stepper motors are both brushless DC rotary motors, and therefore invite comparison. Stepper motors operate in discrete steps and have detent torque, while BLDCs rotate continuously and require feedback for control. BLDC motors are preferred in high speed and/or high duty cycle applications, whereas stepper motors are preferred in low speed low duty cycle applications [21]. BLDCs reach performances out of the working range of stepper motors, however are less efficient in the same working range [48]. The built-in position feedback of a BLDC is a benefit, as a stepper can only infer its position by counting steps. To be able to determine the absolute position of the shaft of a stepper motor, a separate measurement device must be added.

A.1.4. Linear Synchronous Motor (LSM)

Unrolling a BLDC motor results in a Linear Synchronous Motor (LSM). Both BLDCs and LSMs operate on the same principles, and hence their properties are similar. Similar to BLDCs, LSMs are also preferred in high speed and/or high duty cycle applications and are often the preferred actuator for use in high acceleration precision systems. While a BLDC often comes with pre-mounted bearings, an LSM is typically purchased as two separate mover and stator pieces. The user must provide the linear guidance between these two components.

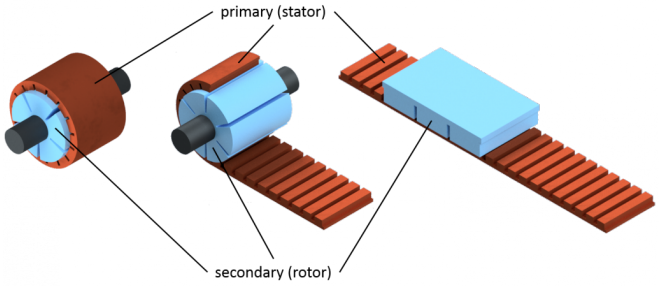

Figure A.3: The rolling out of a BLDC into a LSM [49]

A.1.5. Voice Coil Actuator (VCA)

VCAs are a type of linear electromagnetic actuator without contact between the stator and mover. A permanent magnet resides in the stator, around which the mover consists of a copper coil. Powering the coil generates a force moving the mover in or out [21]. Advantages of VCAs for cryogenic applications are their simplicity, contactless operation, reliability, efficiency, and good control properties due to linearity between drive current and generated force. These motors are dynamic and suited for high duty cycle applications with a typical stroke in the range of several centimeters [21][48]. The length of the mover is typically around 6–13 mm longer than the stroke of the VCA [9]. VCAs have been shown to be capable of positioning accuracy of 0.5 nm [50], and [51] describes a 2-DOF planar VCA driven stage with an accuracy of 200 nm over a 10 mm stroke. At SRON, there is a lot of in-house experience designing and building low-dissipation VCAs for mechanisms at cryogenic temperatures less than 10 K. VCAs developed at SRON have successfully flown in space on the SWS and HIFI instruments of the ISO and Herschel missions respectively [21].

VCAs and LSMs are both linear electromagnetic motors and invite comparison. Generally speaking; VCAs are smaller and lighter, have higher efficiency at low speeds, and are easier to control. LSMs provide a higher force, speed, and stroke but are larger. VCAs are therefore more suited to applications where volume is paramount, and force and velocity less so [52].

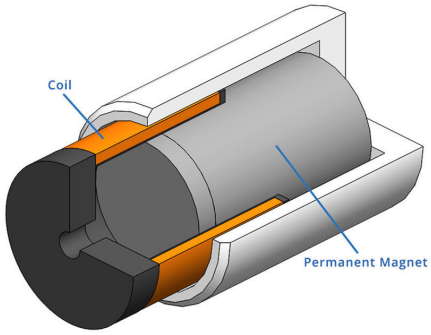

Figure A.4: Cutaway view of a VCA [53]

A.1.6. Actuator Feedthrough

It is also possible to opt for keeping the motors outside the cryostat and use vacuum feedthroughs to pass the mechanical power through into the cryostat and to the mechanism. This potentially saves space within the cryostat and removes the dissipation of the motors from the dissipation budget. However this method is generally not preferred and imposes several drawbacks. Thermally decoupling the ambient motor from the cold mechanism is required to avoid heat injection in the cryostat. Additionally, a reliable mechanical coupling between cryogenic mechanism and motor must be established which allows for shrinkage in all directions between the warm and cold side [54].

A.1.7. Conclusion

There are many different types of cryogenically compatible actuators, each with pros and cons. Low duty cycle, low dissipation, and compact size are the main factors when it comes to evaluating actuators for use within LVF positioning system. Three actuator types stand out: piezoelectric actuators, stepper motors and VCAs. Piezoelectric actuators excel in terms of size, and the walking principle stands out as being the most applicable. It is a better performer than stick-slip based piezos, and piezos with structure based motion amplification are only suitable for use in the fine stage of a dual stage design (described later in Chapter C.3). Stepper motors have excellent average dissipation performance due to their detent torque, and are preferred over BLDCs for this reason. VCAs are preferred over LSMs due to their smaller size and higher efficiency at low speeds. Out of these three types of actuators, no single one is so dominant in its performance as to warrant designing the system around it. That is to say: the design of the mechanism has priority, after which, the most suitable actuator will be applied. Below is a table summarizing the relative performance of the actuators discussed above. Among the different piezoelectric actuators, walking-type actuators are the most suitable, therefore it is only their performance that is represented in the table, and not the other piezo actuation types.

Table A.1: Tabular summary of cryogenically compatible actuators and their relative performance.

		Stroke	Step size & Accuracy	Force	Size	Dissipation	Extras
Linear	Walking piezo	✓	✓	maybe	+ + +	–	+ Stages with built-in linear guides – fragile
	Linear synchronous motor	✓	✓	✓	–	+	
	Voice coil actuator	✓	✓	✓	+ +	+ +	
Rotary	Stepper motor	✓	✓	✓	+	+ + + +	+ Detent torque
	Brushless DC motor	✓	✓	✓	+	+ +	

A.2. Ball Bearings

Ball bearings are classed according to the ISO 492 tolerance classes. The highest precision class (class 2) has an outer diameter radial runout of 1.5 µm (for bearings with an outer diameter of 18 mm or less) [22]. Having two consecutive ball bearings in the kinetic chain from measurement to LVF would result in an uncertainty in the LVF position of 3 µm. As stated in Chapter 2.1.2, the metrology performance goal is 2.5 µm, meaning that this configuration would be out of spec. Furthermore, using grease for lubrication of ball bearings at temperatures as cold as 4 K is not an option. Solid lubricants such as polytetrafluoroethylene (PTFE) or molybdenum disulfide (MoS_2) must be used [55]. Experience within SRON shows that these solid lubricated bearings are more prone to wear-and-tear and binding. As a result, flexures are heavily preferred.

A.3. Flexures and Compliant Joints

A common replacement for a ball bearing is a flexure pivot bearing or a flexpivot, shown in Figure A.5a, which is a type of a compliant joint. Flexpivots are frequently used within SRON and within high-tech and space applications. Benefits of compliant joints are: lubrication free, friction free, backlash free, high repeatability, and small size. This comes at the cost of range of motion; an unloaded flexpivot has a maximum unlimited-lifetime stroke of ±15° [12]. However, when loaded, this unlimited-lifetime stroke reduces. Within SRON a rule-of-thumb for designing with flexpivots is a maximum stroke of ±10°. For more precise values, graphs showing the relationship between load magnitude and maximum angular stroke can be found on C-Flex's website [12]. A flexpivots limited angular stroke can be sufficient for many applications, however it is still a limitation that has to be taken into account, especially in the case of the LVF positioning system where a large ROM is required. Additionally, flexpivot joints exhibit centershift of approximately 1 % of the diameter of the flexpivot [12], however due to the highly repeatable nature of compliant joints this centershift can be accounted for in calibration. SRON commonly sources flexpivots from C-Flex [12].

Another common example of a compliant joint is a prismatic joint created by a series connection of two sets of two parallel leaf springs, shown in Figure A.5b. The maximum stroke δ_{max} of the joint is given by $L^2 = 3Et\delta_{max}/\sigma_{0.2}$, where L is the length of a single leaf spring, E is the Young's modulus of the leaf spring's material, t the thickness of the leaf spring, and $\sigma_{0.2}$ the yield stress of the material [56]. AISI 304 stainless steel is commonly used material for cryogenic leaf springs, for which a common thickness is 100 µm. The Young's modulus and yield stress of 304 steel at 4 K are 210e3 MPa [57] and 405 MPa [58] respectively. This allows for an order of magnitude estimation of the required leaf spring length (in mm) for a given desired stroke (in mm); $L \approx 12.5\sqrt{\delta_{max}}$.

[59] provides a concise review on the most commonly used compliant joints, and two books written by L. Howell ([60] and [61]) serve as the most complete source of information on compliant mechanisms.

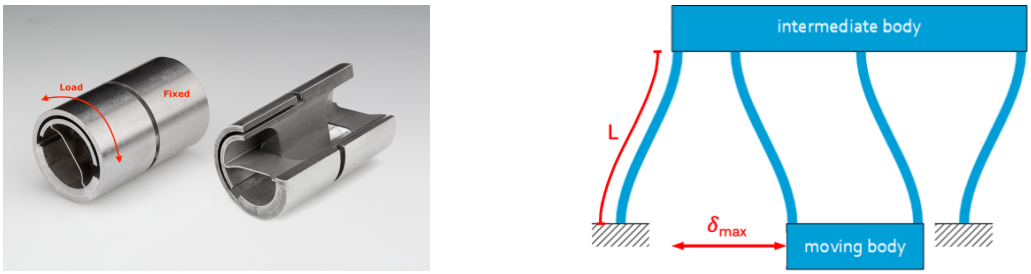

(a) Side by side depiction of a flex-pivot bearing and its cutaway view; adapted from [62].

(b) Diagram of a double parallel leaf spring stage; adapted from [56].

Figure A.5: Two different types of compliant joints.

B Literature Review: State-Of-The-Art Cryogenic Positioning Solutions

This chapter explores existing cryogenic industry solutions and literature in order to identify viable options for use in the LVF positioning system. State-of-the-art solutions are investigated and evaluated on their ability to fulfill the requirements of the LVF positioning system. This evaluation will determine whether off-the-shelf solutions, or those documented in literature, can be directly applied to meet the stated requirements of the LVF motion system.

B.1. Industry

High precision, large stroke 2-DOF cryogenic positioning systems rarely exist as off-the-shelf solutions. Usually these systems are designed specifically for a given problem to enable a high degree of integration. There are however some existing solutions. These are 1-DOF stages for which two can be mounted serially to enable 2-DOF motion. SmarAct SLC stick-slip piezo stages offer up to 51 mm of travel and sub-nanometer resolution within a very compact volume [63]. These stages are cost effective, however due to the stick-slip piezo principle, the dissipation is likely to be unacceptably high for application within the LVF positioning system. Onnes produce a piezo-walking based stage called the arQtika LCW. The stated travel range is 12 mm. In private communications it was stated that this can simply be increased by lengthening the axle. The arQtika also exhibits sub-nanometer resolution and further states a repeatability of 10 nm [36]. These stages are very promising for application within the LVF positioning system. The JPE cryo linear drive offers sub-nanometer stepsize over a range of 51.5 mm [64]. Furthermore there are also linear ballscrew stages. This is a very common type of linear stage and can be sourced from multiple suppliers, an example being UCryo [65]. Both have a significantly larger volume than the SmarAct and Onnes stages, but offer capability to handle larger loads and driving forces.

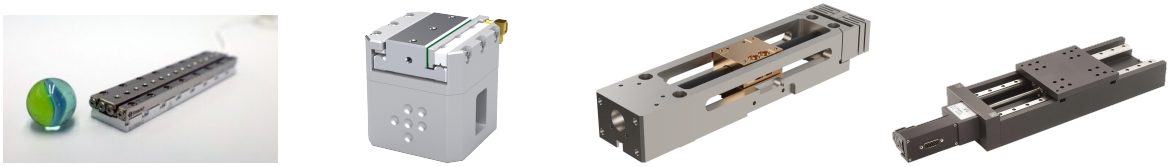

(a) SmarAct SLC [63] **(b)** Onnes arQtika LCW [36] **(c)** JPE cryo linear drive [64] **(d)** Ballscrew linear stage [66]

Figure B.1: Existing large stroke cryogenic off the shelf 1-DOF positioning systems.

B.2. Literature

Purpose built precision large stroke cryogenic mechanisms are found in literature, although the available literature is limited. Described in [44] and [67], and shown in Figure B.2, is the principle of an indented slider mechanism designed by NOVA-ASTRON for use in MATISSE. Five pairs of kinematically located ball bearings are used to perfectly constrain 5 DOFs of the slider, leaving one unconstrained translational DOF. Each bearing pair consists of a fixed bearing and a spring loaded bearing placed opposite it to guarantee accurate and play free motion. One of the spring loaded bearings is made to run over V-shaped indents. The mechanism actuator (a Phytron stepper motor) pushes (or pulls) the slider from one indent to another, each time selecting a different position with a high level of position repeatability and accuracy. Deliberate slack between the actuator and the slider is implemented to ensure accurate positioning by the indent rather than by the actuator. Notably, for the indents to be useful in positioning,

the actuator in the system must be capable of smaller steps than the spacing in between the indents. If the actuators steps are larger than the distance between the indents, a single step of the actuator will potentially skip over an indent. Test results showed that the positioning accuracy and reproducibility of this mechanism is at the level of less than 2 µm in all directions. This inaccuracy is partially caused by inevitable surface roughness of the track and V-indents, and primarily caused by the unavoidable runout of the ball bearings as stated in Chapter A.2. The slider has a stroke of 72 mm and this can be simply increased or decreased by adjusting the design. Wear has been experimentally verified to be essentially non-existent [68]. For the application within the LVF positioning system the indents are not a viable solution, however the principle of the 5 pairs of kinematically located ball bearings is promising. Indents every 25 µm are not feasible due to manufacturing tolerances and wear and tear. Additionally the actuator would have to be capable of 25 µm steps, in which case the actuator could simply be used to directly drive the LVF, and the implementation of the indents only adds potential repeatability improvements to the system.

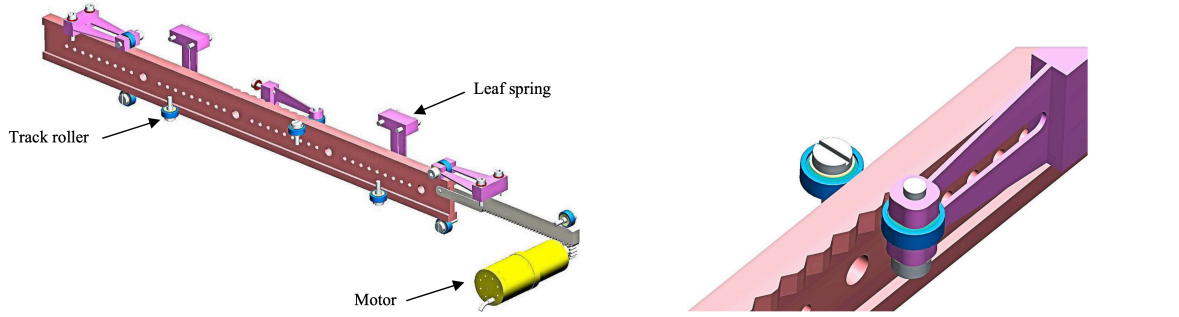

(a) Overview of the indented slider mechanism

(b) Detail view of the ball bearing running over the V-shaped indents

Figure B.2: The principle of an indented slider mechanism with five kinematically located pairs of ball bearings [67]

Secondly, [69] and [70] describe the SRON designed on-ground test setup for SAFARI which utilized three UCryo linear ballscrew stages mounted serially to enable 3 DOF motion driven by BLDC motors. The setup was able to reach a position accuracy of ±3 µm and repeatability of ±1 µm over a range of 50 mm. The cryostat in which this test setup was constructed was many times larger than the cryostat available for the LVF positioning system. Serially mounting two ballscrew stages in infeasible for application in the LVF positioning system due to the space restrictions. Furthermore, in private communications with Martin Eggens, it was mentioned that relatively soon after being put into operation the ballscrew stage began to suffer from binding issues due to wear and tear. This is due to the inability to grease and lubricate moving parts at the low temperatures of a cryostat, and the fact that the ballscrew stages are overconstrained, causing extra internal stresses and making them extremely sensitive to proper alignment of the linear bearings within the slider.

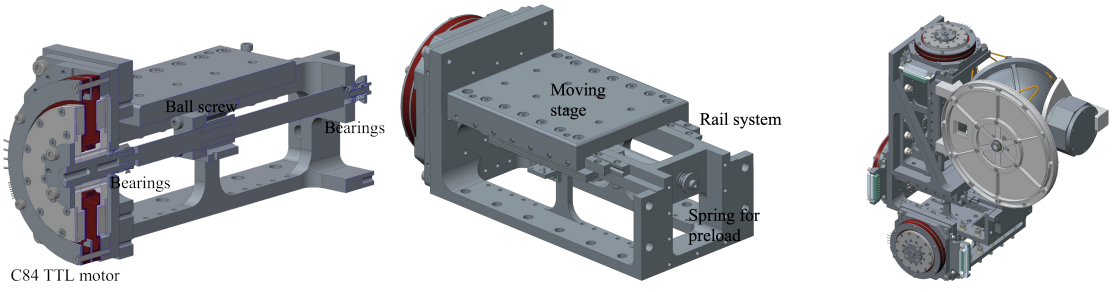

(a) A cutaway view of a single ballscrew stage

(b) One ballscrew stage

(c) The entire 3 DOF stage with the device under test also mounted

Figure B.3: Three serially mounted ballscrew stages enabling 3 DOF motion of the device under test [69]

Lastly, [71] describes the the mechanisms flown on JWST for mirror alignment designed to function at 20 K. The mechanism consists of a coarse and fine stage (a concept which is explained in further

detail in Chapter C.3) and notably achieves this dual-stage design using only a single actuator. The fine stage consists of an eccentric cam and a flexure mechanism. The coarse stage consists of a ballscrew on which the entire assembly is mounted. The switching between coarse and fine stage is handled by a drive shaft coupler. The coupler has a backlash of approximately 320°. When the coupler is engaged, the coarse stage is driven, and the entire assembly moves up or down the ballscrew. When the coupler is disengaged, nothing actuates the ballscrew, and therefore it is the fine stage that dominates displacement. The design excels at deforming the mirrors of the JWST, where the dominant external force is on-axis and only present in the translational up and down direction in Figure B.4. Therefore the mechanism possesses a high supporting stiffness in the translational up and down direction, and can tolerate lower supporting stiffness in the other DOFs. However within the LVF motion system a relatively high supporting stiffness in other DOFs is desired.

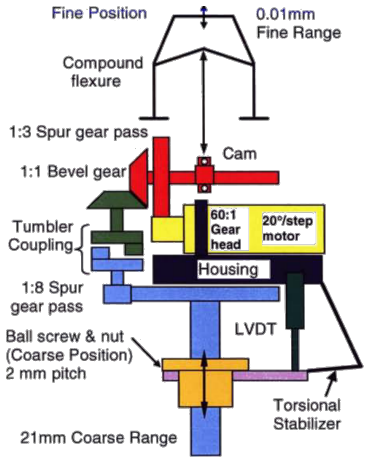

Figure B.4: Schematic depiction of a the Ball Aerospace dual-stage mechanism with one actuator [71]

C Literature Review: Non-cryogenic Literature

No solution found within industry or cryogenic literature in Chapter A meets all the requirements set for the LVF positioning system without modification. Therefore it is necessary to develop a custom solution. This custom solution can potentially implement components found in Chapter A or draw inspiration from the discussed literature. In this section further research will be done into solution paths that are not directly cryogenically compatible. The step from not-cryogenically compatible to cryogenically compatible can be trivial, and therefore it is still feasible to extract inspiration from these solutions. The literature discussed within this chapter is based on compliant mechanisms, where simply substituting materials and actuators with those rated for cryogenic conditions can render the concepts cryogenically compatible.

C.1. Piezo Amplification

As stated in Chapter A.1.1, piezoelectric actuators are often combined with amplification mechanisms due to their low stroke but high force. These amplification mechanisms are often compliant as to maintain the backlash-free benefits of piezos. [72] and [73] provide a review on compliant piezo amplification mechanisms. Shown in Figure C.1a is a selection of simple amplification mechanisms. Amplification mechanisms often rely on a lever or a nonlinearity to amplify motion and amplification ratios typically don't exceed 100 (as shown in Figure C.1b). To form a best-case-scenario frame of reference for the required amplification ratio in the LVF motion system; take the largest travel (non cryo rated) PI piezostack actuator (0.18 mm) [74], the smallest possible ROM (20 mm) within the LVF motion system requirements, and the fact that at 4 K only 5 % of a piezo's room-temperature expansion remains. This leads to a best-case-scenario required amplification ratio of $\frac{20}{0.18 \cdot 0.05} = 2222.2$, which is an order of magnitude larger than the largest amplification ratio mentioned within [73]. Due to the large strokes required for the LVF positioning system, piezo amplification is more suited to a potential fine stage mechanism; not as a standalone full-stroke stage.

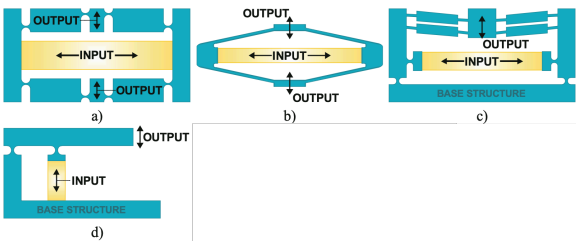

(a) Examples of simple compliant piezo displacement amplification mechanisms [72]

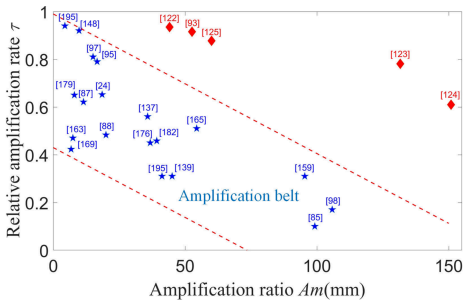

(b) Relations between amplification ratio and amplification rate of some classical multistage amplifiers. Mechanisms in the upper right hand region are the better performers. [73]

Figure C.1: Piezo amplification

C.2. Compliant Stages

In parallel planar 2-DOF compliant stages, actuating the end-effector (EE) in one DOF (ideally) does not move the location of the force application point of the other DOFs actuator. In Figure C.2a, actuating the EE in positive Y-direction causes 'flexure B' to flex upwards, while the position of the force application point of the X-direction actuator ('intermediate stage 1') remains largely unaffected (it will move slightly towards the center). The same is the case in Figure C.2b: actuating the EE in

positive Y-direction results in flexing of the light-grey stage while the dark-grey stage remains unaffected (and therefore also the force application point of the X-actuator). This allows for the actuators to be mounted to the fixed world leading to increased stiffness and dynamic performance. As a result these stages excel at providing fast and precise motion capabilities. However, due to the connected nature of the flexures that govern the two DOFs, actuating the EE in one DOF almost certainly results in some parasitic motion of the EE in the other DOF. This is called cross axis coupling and in the design of these compliant stages substantial effort is directed towards minimising this.

The connected nature of the two DOFs limits the ROM of these types of stages, and typically the workspace-footprint ratio is orders of magnitude too small for application in the LVF positioning system. [75] describes a motion stage with a workspace-footprint ratio of 0.007. As a result this type of mechanism is not well suited for use in the LVF positioning system. Making such a stage suitable for the LVF positioning system would require significant modifications and necessitate pushing the limits of flexure joint ranges, likely at the cost of accuracy and cross axis coupling.

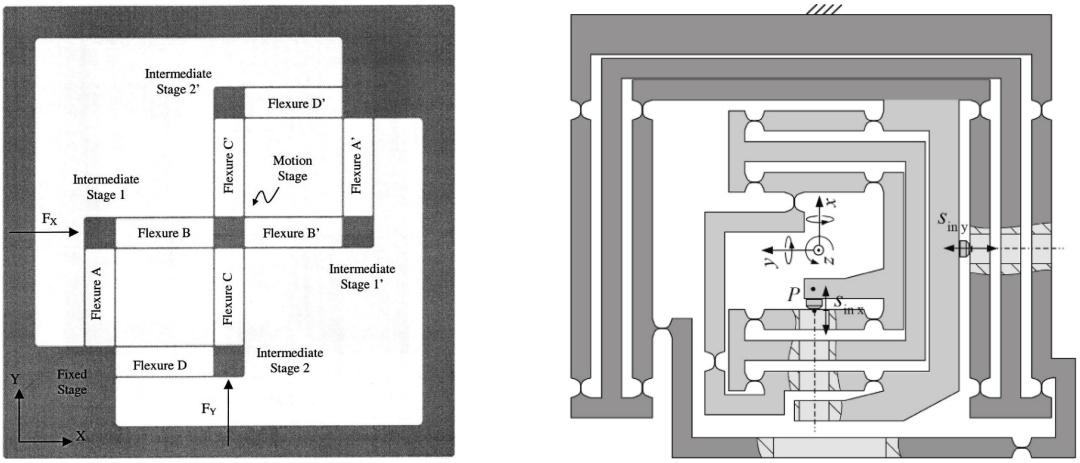

(a) Simple XY monolithic piezo stage [76]

(b) More complex XY monolithic compliant motion stage [75]

Figure C.2: Two examples of a monolithic 2-DOF motion stages.

C.3. Coarse-Fine Stage

Dual-stage, or coarse-fine stage, mechanisms allow for the combination of large strokes and high accuracies. These mechanisms typically use two actuators to control a single DOF. [77] describes a planar 2-DOF dual-stage positioning system with a resolution of 40 nm and a stroke of approximately 3 mm in both X and Y. Specifically the mechanism described takes action to decouple crosstalk between the two actuation axes, and reduce interference between the coarse and fine actuators of a single DOF. The coarse stage is driven by a VCA and the fine stage by a piezo stack. The mechanism itself (excluding VCAs) has a footprint of approximately 181×181 mm. That results in a workspace-footprint ratio of approximately 0.000275. The mechanism is shown in Figure C.3. Just as in Chapter C.2, this is a parallel stage and actuating the EE in one DOF does not move the location of the force application point of the other DOFs actuator. The VCAs act as the coarse positioning actuators and provide a large stroke with low accuracy and the piezos act as the fine positioning actuators providing a small stroke with high accuracy.

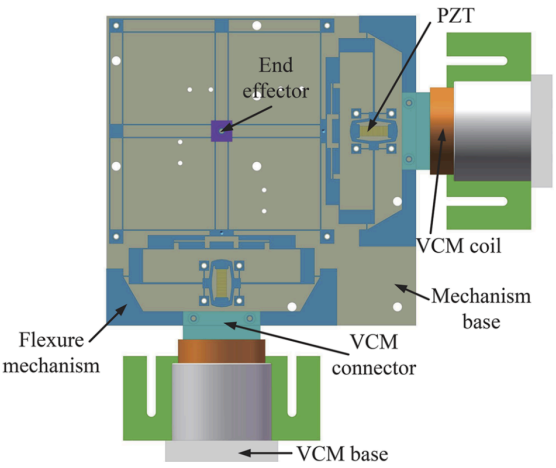

Figure C.3: A parallel dual-stage 2-DOF compliant mechanism [77]

C.4. Static Balancing

A statically balanced system is a system which is in static equilibrium throughout its range of motion. Consequently, quasistatic motion requires no operating effort [78]. In reality, friction, acceleration, and imperfections in the static balancing of the system are inevitable, and therefore some operating effort is required. The benefit static balancing can bring to the LVF positioning system is reduced dissipation due to reduced operating effort as a result of gravity compensation.

Static balancing of linkage mechanisms and parallel manipulators tends to result in a considerable amount of added complexity which makes their application and implementation challenging [79]. However, there are examples where static balancing is attainable without excessive complexity. A statically balanced parallelogram linkage is shown in [80]; a statically balanced fully compliant parallel 5-bar mechanism is shown in [81]; and parallel 5-bar mechanism with a parallelogram statically balanced with tension springs is shown in [79]. These simply statically balanced mechanisms show promise for applicability in the LVF positioning system. [78] contains an abundance of information on statically balanced mechanisms and methods for static balancing.

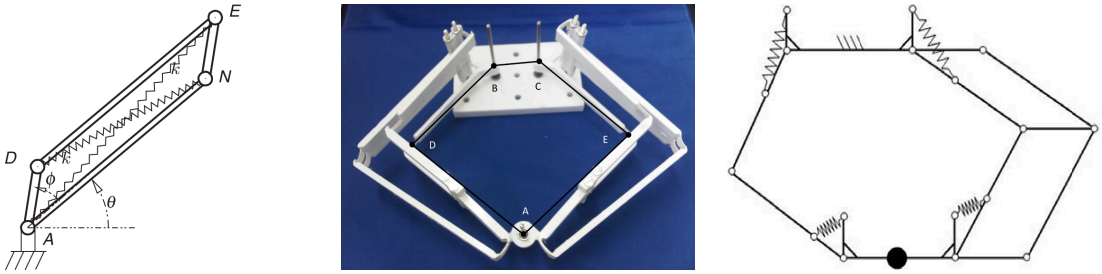

(a) A statically balanced parallelogram linkage [80]

(b) A statically balanced fully compliant parallel 5-bar mechanism [81]

(c) A statically balanced parallel 5-bar mechanism with a parallelogram [79]

Figure C.4: Examples of statically balanced mechanisms.

C.5. Compliant Linkage Mechanisms

[82] shows a concept for a parallel 2-DOF mechanism driven by two VCA's. The paper focuses on design for high accelerations, which is not required in the case of the LVF positioning system. However the precision and stiffness benefits of a parallel mechanism are still applicable. A repeatability of 1.5 µm is reached over the workspace of 55×55 mm. No explicit mention of the joint type is made; however, flexure joints can be easily applied. The fact that the actuators are at 90 degrees from one another is a disadvantage in the eyes of the LVF positioning system. The configuration necessitates having one of the actuators positioned floating in the middle of the cryostat making it harder to mount stiffly and

harder to thermally strap. Additionally, due to the limited height budget in y-direction in the cryostat, it is unlikely that there is sufficient space for the actuator to be positioned directly below the LVF.

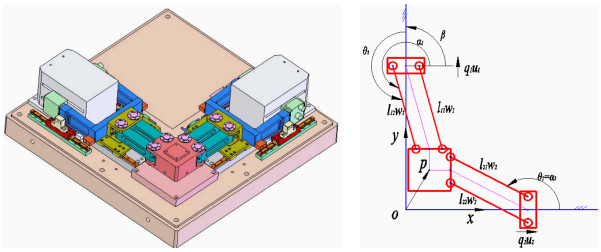

Figure C.5: The parallel 2-DOF VCA driven mechanism [82].

Secondly, in [13] a 2-DOF LSM driven fully flexure based mechanism is developed for use in vacuum applications. The paper tackles the problem that to maintain high stiffness over the range of motion, flexure based positioning mechanisms often have a short end-effector stroke due to stress limitations and a decrease in stiffness in supporting directions of the compliant joints when deflected. A cited reference large stroke flexure mechanism has a workspace-footprint ratio of 0.000278. This small workspace-footprint ratio makes flexure based mechanisms impractical for use in confined spaces, like vacuum chambers for this paper, or cryostats in the case of the cryogenic positioning system. The solution presented in the paper achieves a workspace-footprint ratio of 0.03125 with a 60×60 mm workspace.

The proposed mechanism is designed to be perfectly constrained in order to avoid build-up of internal stresses due to misalignment. To achieve this perfectly constrained design the 'forearms' of the mechanism require notches to be cut in them to release two rotational DOFs (shown in Figure C.6c). The 'upper arms' have no notches cut and are actuated by LSMs modified to be curved (Figure C.6b). Linkage G requires the unique design shown in Figure C.6d as to only constrain the singular DOF of the end-effector's rotation about its Z-axis. The design consists of a compliant a ball joint at each end of the linkage. However, this makes the design underconstrained, as there are 6 released DOFs, not 5. This results in an internal vibration mode, however the frequency of this mode is sufficiently high as to not interfere with the dynamics at the EE.

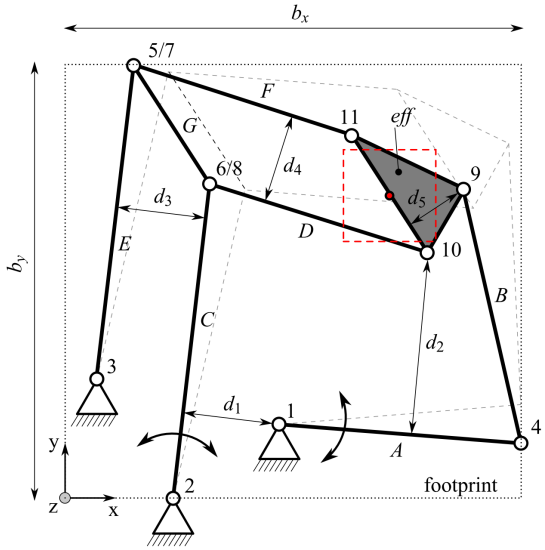

(a) Conceptual layout of the mechanism.

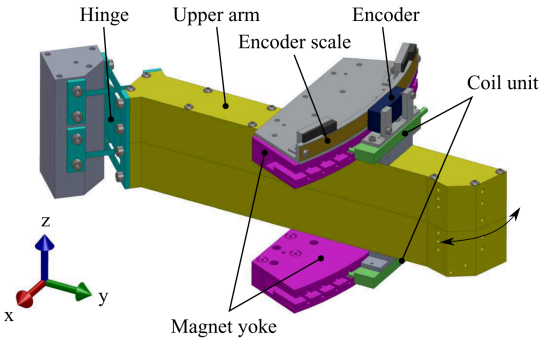

(b) The 'upper arms' driven by curved LSMs.

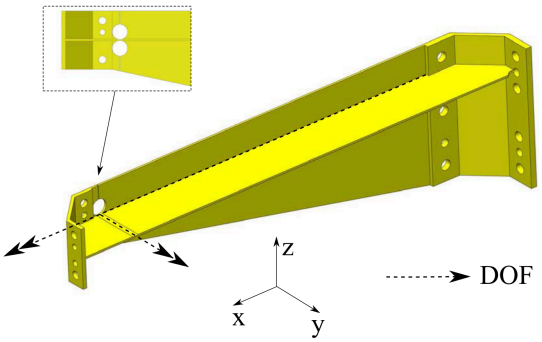

(c) Design of the 'forearms' with the DOFs shown as arrows.

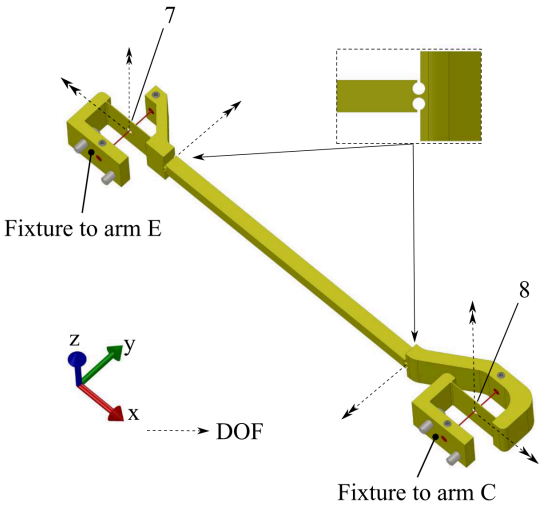

(d) Design of linkage G with the DOFs shown as arrows.

Figure C.6: 2-DOF parallel compliant mechanism described in [13]

C.6. Conclusions

Piezo amplification does not show potential to function as a standalone full-stroke stage within the LVF positioning system due to the order of magnitude discrepancy in amplification ratio between what is available in literature and what is required. Though it is the best choice for the fine-stage actuator of a dual-stage mechanism. However, dual-stage mechanisms are excessive, as the coarse actuator itself (a VCA for example) will likely be capable of achieving sufficient resolution, therefore rendering the fine stage useless. Parallel planar 2-DOF compliant stages are more promising, though due to their lacking workspace-footprint ratio and likelihood of cross axis coupling at the large ranges of motion required by the LVF positioning system, they are considered inferior to linkage mechanisms. Linkage mechanisms show the most promise. This is in large part due to their ability to reach larger workspace-footprint ratios than the other mechanism types, while still providing sufficient supporting stiffness. Static balancing of a linkage mechanism would reduce the required actuator force and therefore reduce dissipation.

This page is intentionally left blank.

D Brainstorm Concepts Scans

Shown below are scans of the 1:1 scale drawings made during the brainstorm phase of concept creation. Initially 3 different versions of the 5.1 concept are shown, where the LVF exits the bundle in different directions, and the LVF is oriented in different directions. After this, the real concepts are shown. First the concept is displayed within the cryostat, after which some calculations and pros and cons of the concept are shown.

5.1

- Vertical LVF
- rom x 45 (ad d bundle)
- rom y 40
- max positions are when arms are (nearly) vert/horiz
- means that a = little more than rom x = 45
- b as wide as possible, b = a(little more) + holder dim
  you never want singularity
- S = a from y = 85

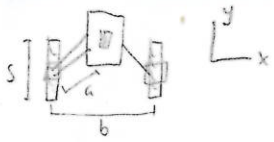

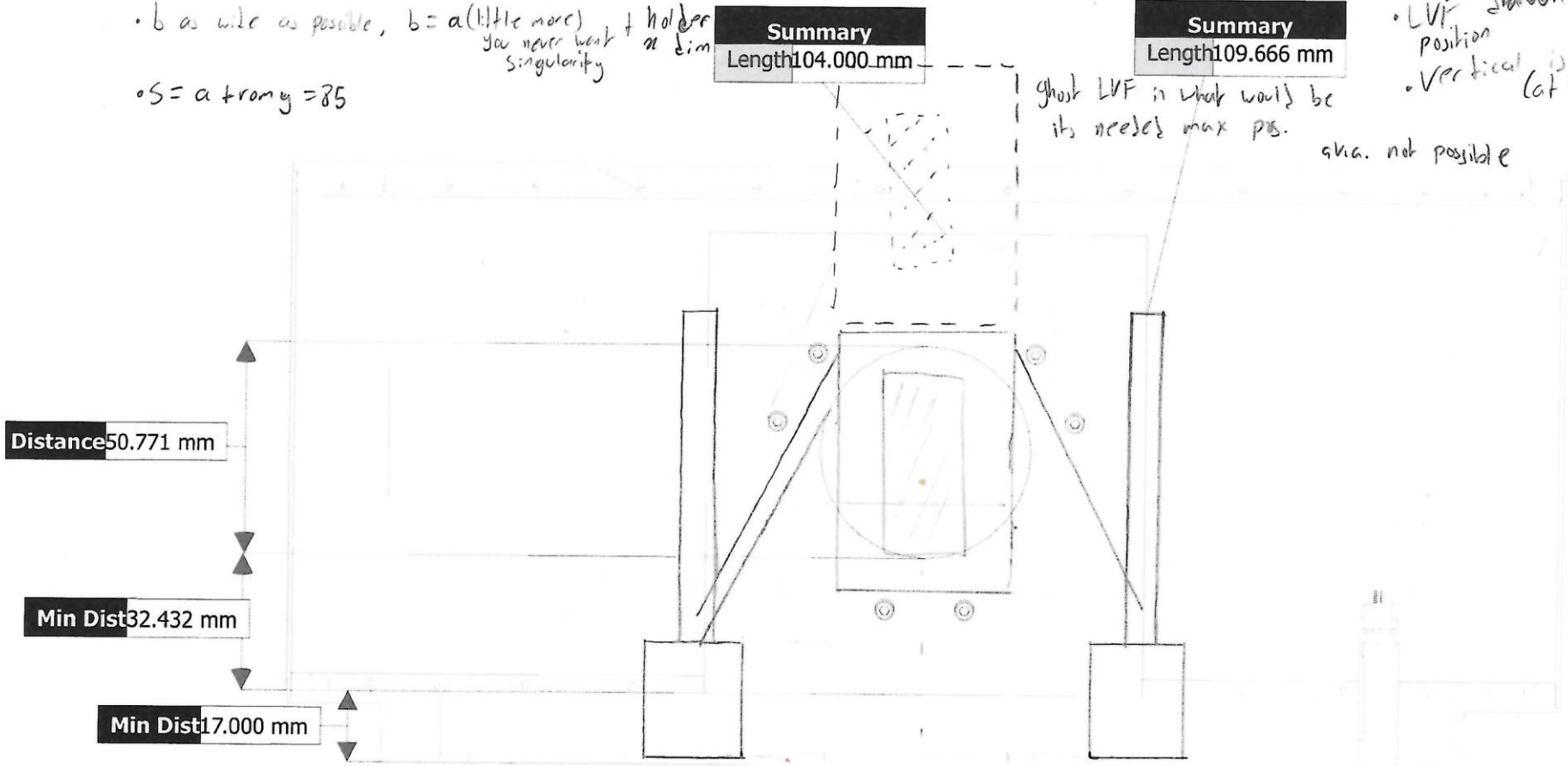

ghost LVF in what would be its needed max pos.

aka. not possible

- LVF drawn in lowest possible position
- Vertical is not possible ? (at least not in this (min.) dimensions)

5.1 horiz LVF y dir out

- rom x : 40 or 65 (y dir / x dir)
- rom y : 45 or 20

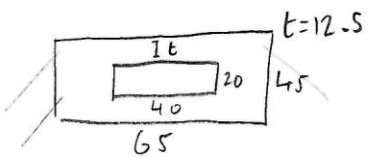

out of bundle in x dir: $a = \text{rom } x = 65$

$b = \text{rom } x + x \text{ dim of lvf} = 65 + 65 = 130$

$s = \text{rom } y + \sqrt{a^2 - x^2} = 76.3$ ($x = (b-65)\frac{1}{t}$)

the whole LVF holder must fit between middle 3 goalpost

out of bundle in y dir: $a = \text{rom } x = 40$

$b = 2x(40+t) = 105$ The whole LVF & one of its holder sides must fit inbetween center one & goal post.

$s = \text{rom } y + \sqrt{a^2 - x^2} = 79.6$ ($x = (b-65)\frac{1}{t}$)

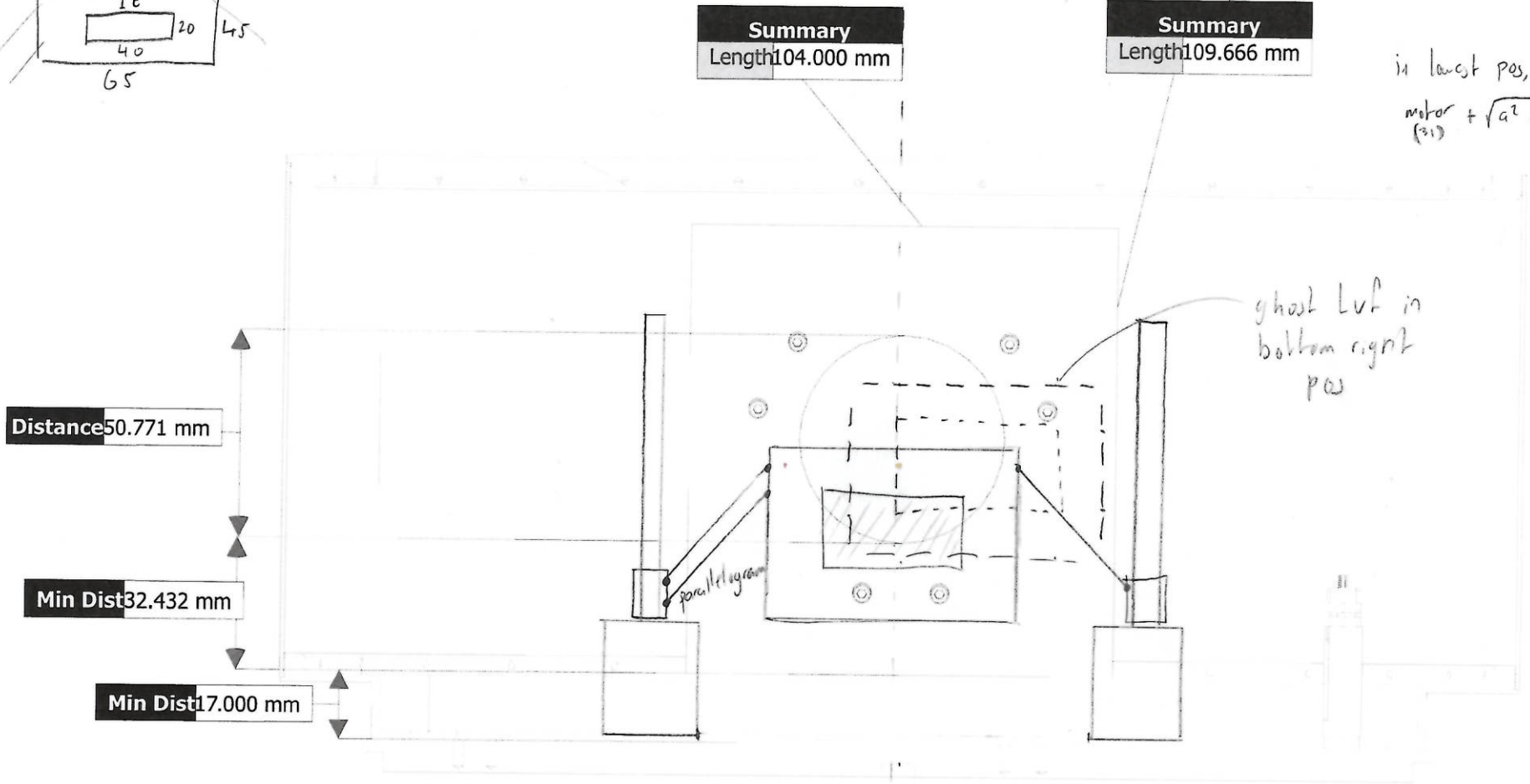

in lowest pos, top of LVF is at height of

motor (31) + $\sqrt{a^2 - x^2}$

x dir → 87.3

y dir → 65.6

+ y rom this become

x: 107.3

y: 110.6

I pick for out in y dir bec LVF can be below center of window (at 74 mm)

5.1 horiz LVF
X dir out of bundle

a = 65
b = 130
s = 76.3

lowest pos top = 97.3
highest pos top = 107.3

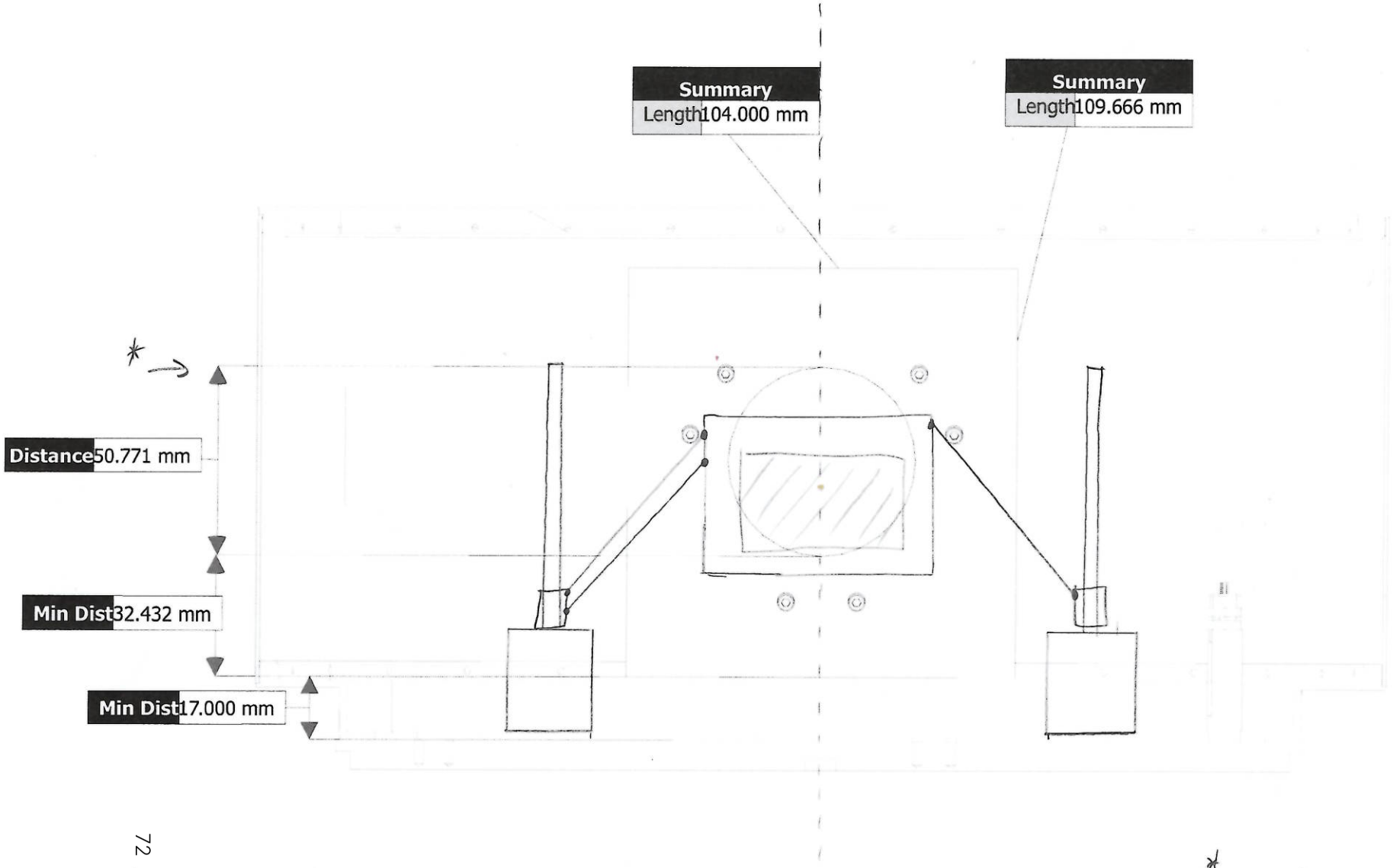

actually the lowest ⟷ x scan height achible is approx 100 mm height (*see →)
at this bottom pos there is no possibility for x scan
rendering this a non usable concept

5.1 horiz LVF

y oob

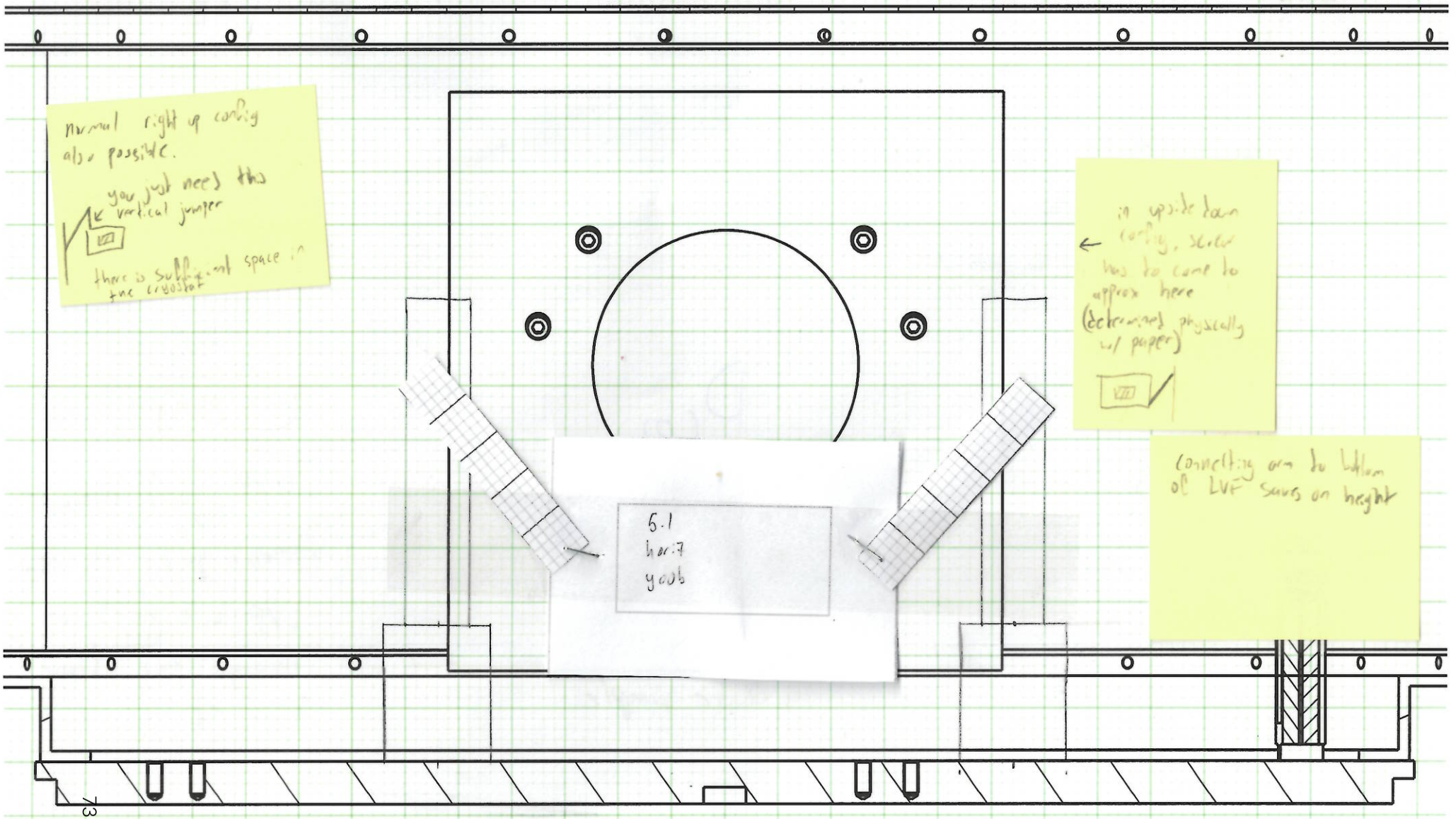

grid 2mm - bold 10mm

must be arms down because the only oob direction is -y.

y rom = radius + holder thickness + LVF short
= 25 + 12.5 + 20
= 57.5

x rom = LVF long = 40

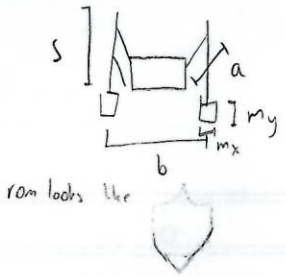

rom looks like

for stepper motor calcs see other 5.1 drawing

m_x = 19
m_y = 26.5

a = x rom = 40

b = a + holder long = 40 + 65 = 105

s = I dont need full x dexterity at oob position
= a + y rom ← not 57.5, but less only 20
= 60

Pros

- Stiff
- Stepper motor detent torque is sufficient
- Quite simple

Cons

- 90° joint flexion
- Linear guide required
- LVF will need to go through the floor bracket

4.1

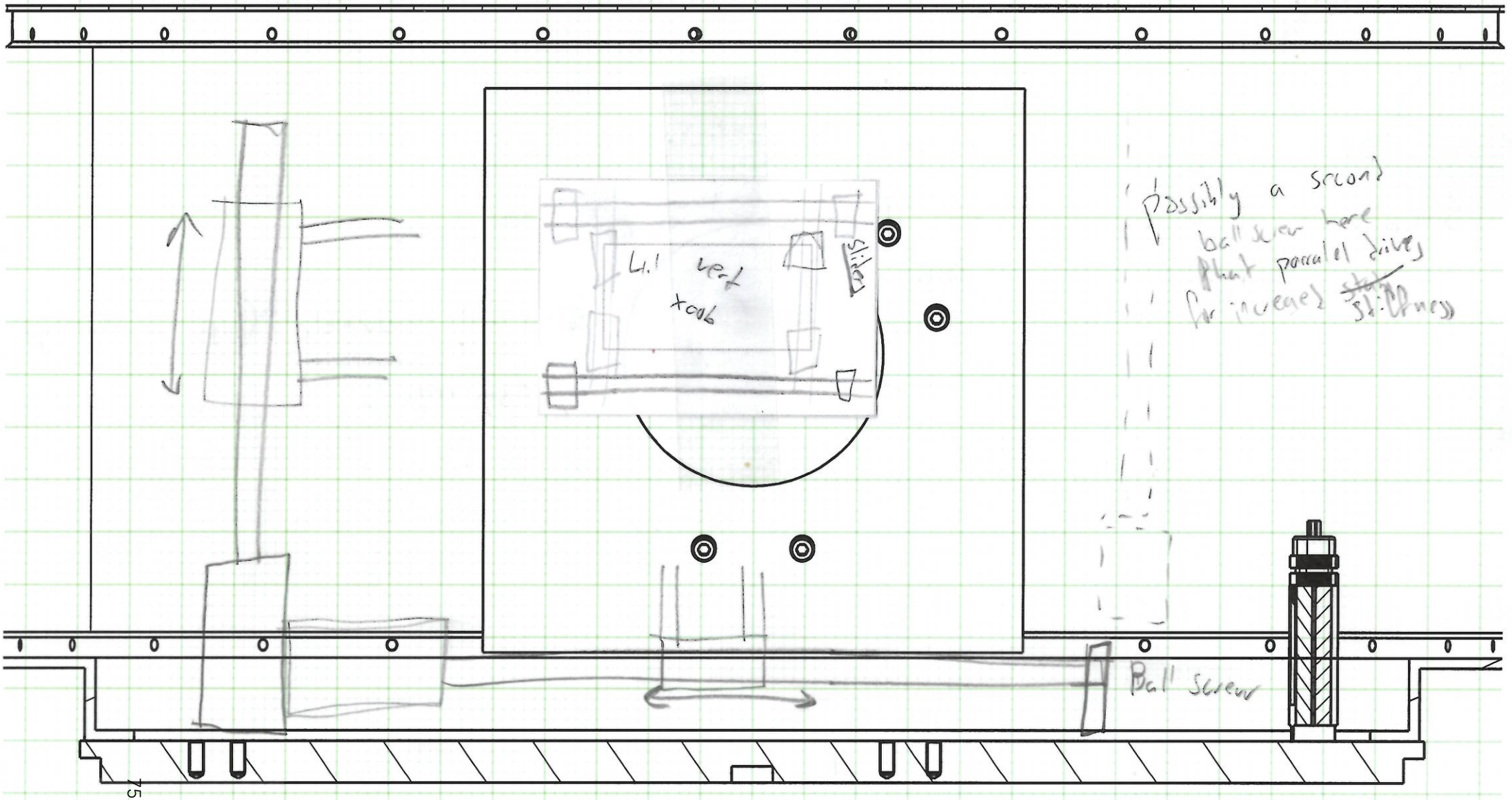

grid 2mm - bold 10mm

Pros

- Similar to an H-Drive
- Simple

Cons

- lots of bearings & lots of linear guides
- large moments
- maybe position of LVF is not so well measurable (high uncertainty)
- overconstrained & good parallelism required

#3.1 gabby slider ✓

Slider can be driven by: - VCA
- Linear ironless
- Ball screw
- Cog

remember, there must be play in all directions as to not over constrain things

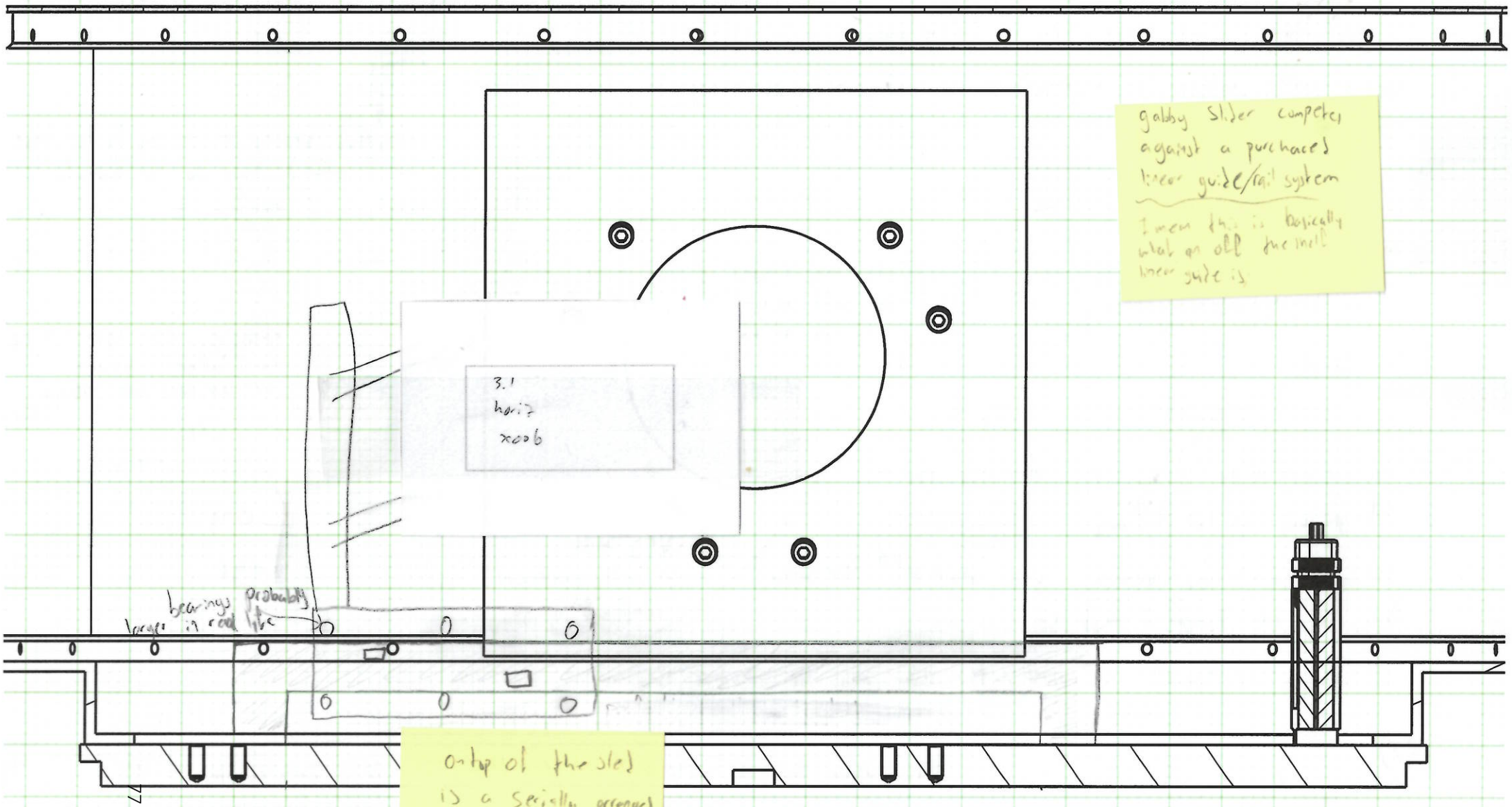

grid 2mm - bold 10mm

driven by VCA / linear motor / cogged DC or stepper

horiz LVF x oob

Put a huge room in the x dir to simplify y motion.

huge room is not a problem for a slider & linear motor / rotary motor + cog

x room = 40 + 12.5 + 25 = 77.5

y room = 20

with a gabby slider there are 2 options

a) fixed bearings & moving axle

b) fixed axle & moving bearings (sled)

the difference is the moving weight.

b has much less moving weight

also in max extension a has big moment

meaning that bearing spacing has to be larger than it would have to be for b

therefore I prefer b

we have chosen orientation b. need to how wide do we assume our sled to be?

tot len of axle = 77.5 + play + len

= lets say LVF dim, so 65

x 78 + 65

≈ 145

Steel of 10x10 square cross sec would deflect 1.45 μm w/ 1kN load over 146 mm

20x20 is 0.09 μm

you can place all the bearings right in the middle like ---

but you will have bad stiffness

the more spaced the bearings the more stiff the slider, but also the longer it must be

if bearings are spaced x apart, the slider must be 78 + x long

Pros

- Very stiff
- perfectly constrained
- compliant y-stage

Cons

- Large

ex)

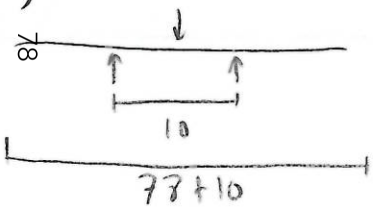

that means the most spacing I could possibly have is Diam crystal - 78

≈ 280 - 80

≈ 200

In reality the spacing will be determined by bearing force & precision data/spec

12.1 Similar to 5.3

Linear actuator/VCA/ballscrew

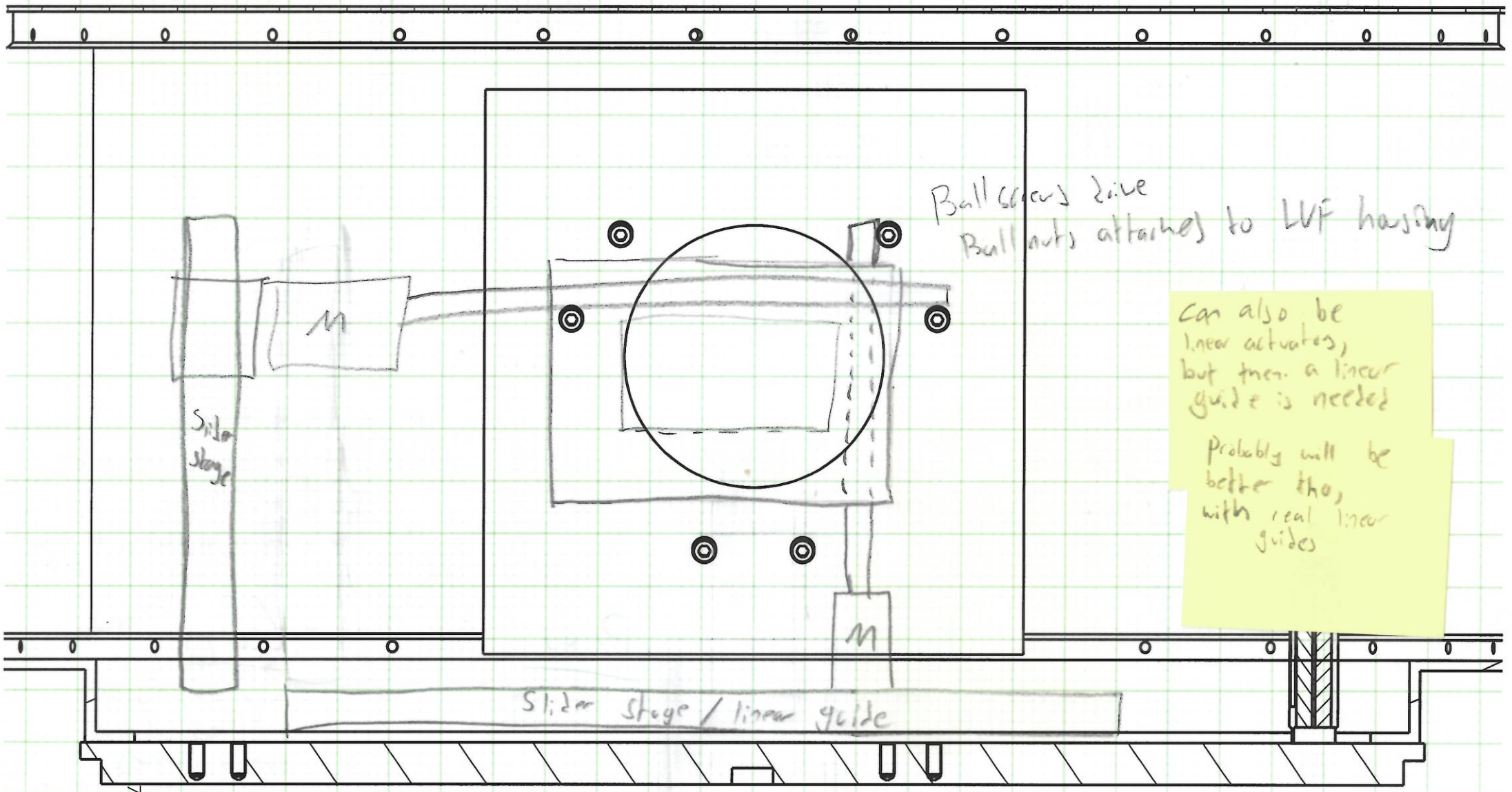

grid 2mm - bold 10mm

Simple purchased sliders eg bosch

Simply actuation range & sliding range are equal

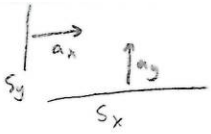

VCAs are longer than linear actuators and always required extensions

that's why switch to LA's

horiz LVF

y oob

$y_{rom} = 57.5$

$x_{rom} = 40$

x oob

$y_{rom} = 20$

$x_{rom} = 77.5$

vert LVF

x oob

$y_{rom} = 40$

$x_{rom} = 57.5$

$a_x = 40$ s_x = same

$a_y = 57.5$ s_y = same

this is the only solution that allows for y actuation voice coil to be mounted in-plane, under the LVF

this is nice and mitigates the need for extensions

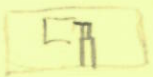

but the x does not fit it is too long. you would have to stack/fold/extend anyways

VCA vs LA vs Ballscrew

- VCA & LA needs to be linearly guided

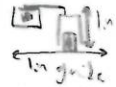

- a ball screw secured at both ends is the linear guide

Pros

Cons

- large moments on ballscrews & base
- Overconstrained
  - additional linear guides required next to the ballscrews

less good version of L.1

08

For VCA, length = 2x stroke

mat pos

For LA, length = stroke + motor dim

L x 3S transition vc

2.2 normal parallel RR flex or bearing

Possible just harder. Parallelogram cooler

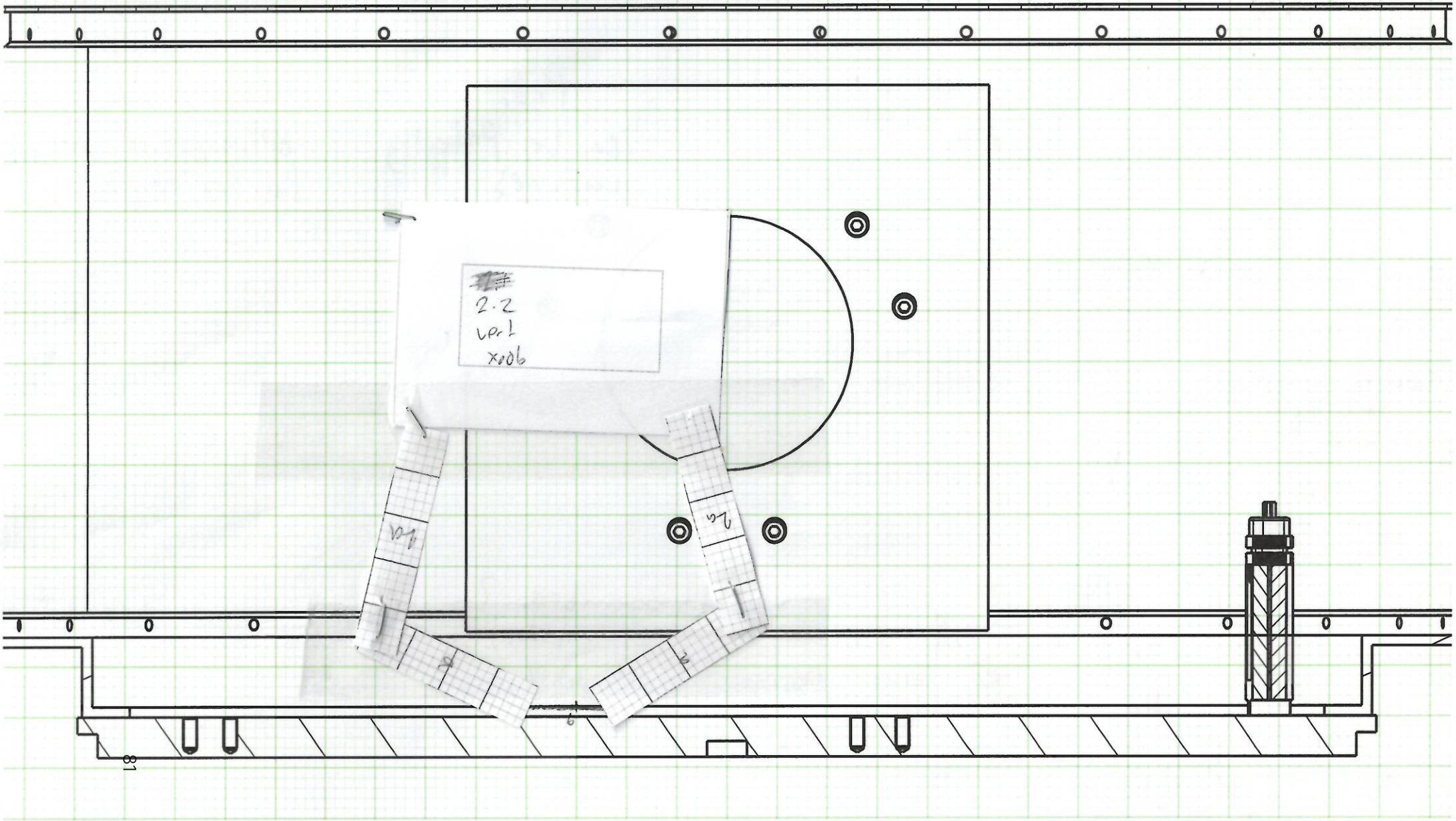

m - bold 5mm

grid 2mm

bold 5mm

++ mode

five-bar planar parallel manipulator

← allows for possibility of Howell's statically balanced } maybe the statically balanced also just works in other configs- probably

++ mode

+− mode

obs in y
horiz LVF

Pros

- Can be perfectly constrained
- Stiffer than (1.1)

Cons

- optimization needed for link lengths

Just to move on & pick something

++ mode

balanced (square) rom
- vert LVF
- x obs

xrom = 45

yrom = 40

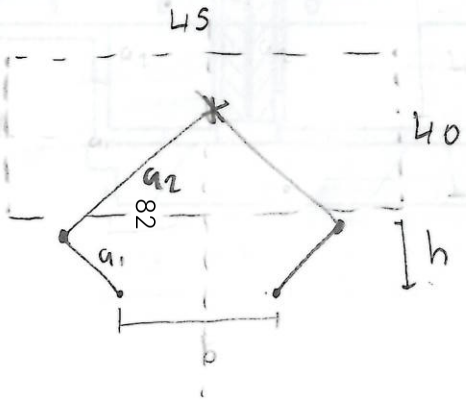

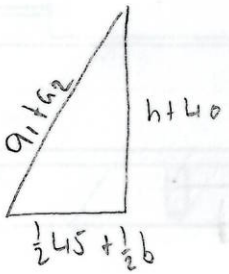

$$(a_1+a_2)^2 = (h+40)^2 + \left(\tfrac{1}{2}45+\tfrac{1}{2}b\right)^2$$

let say: $b = a_1$, $a_2 = 2a_1$ ⇒

$h \approx 12$

$$(3a)^2 = (52)^2 + \left(22.5 + \tfrac{1}{2}a\right)^2$$

$a \approx 20.5$

11.2

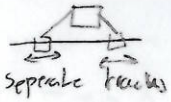

✓ x or y oob

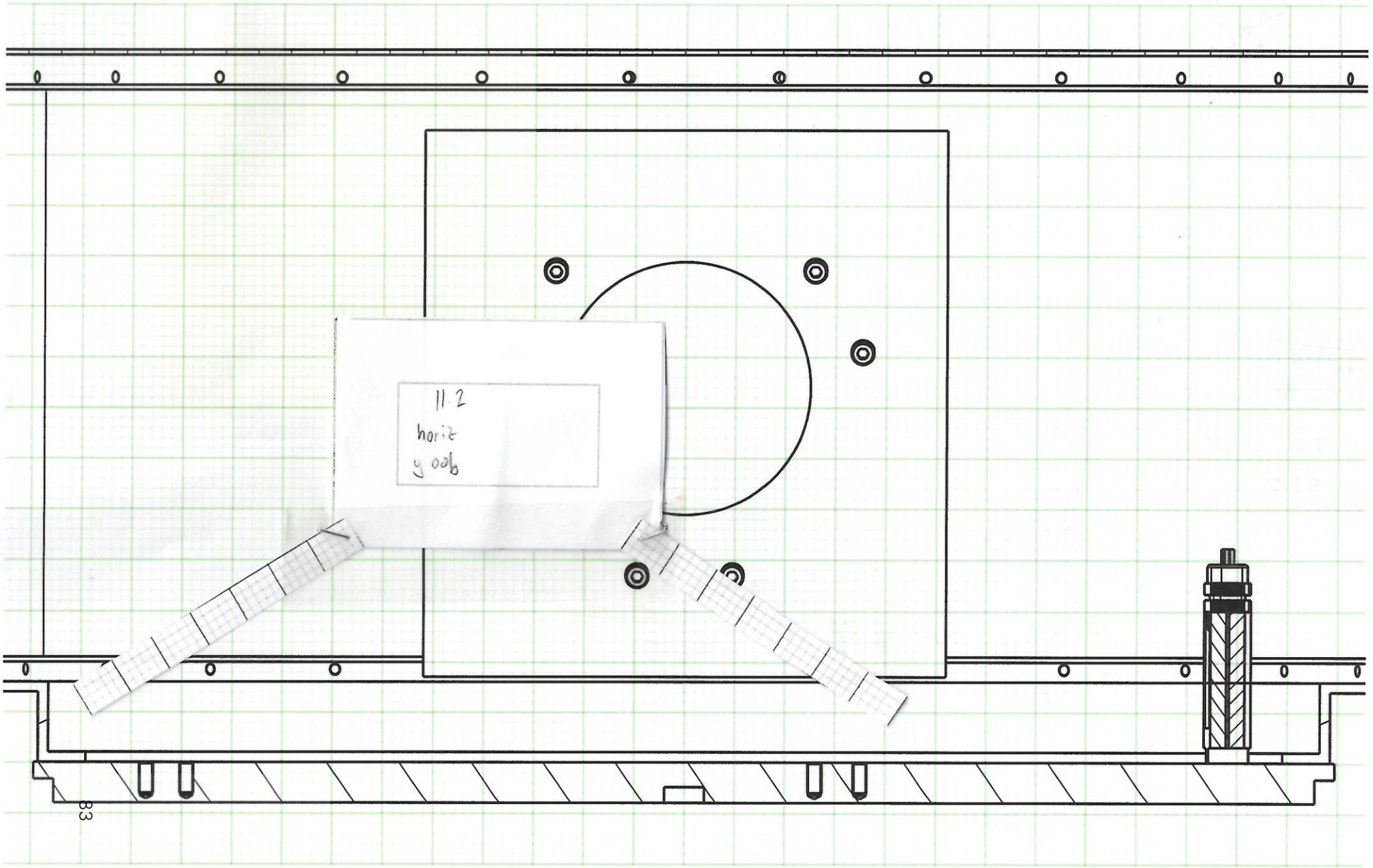

83

grid 2mm - bold 10mm

horiz y oob

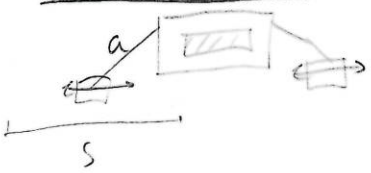

$x_{rom} = 40$

$y_{rom} = 57.5$

$a = y_{rom} = 57.5$

$s = a + x_{rom} = 97.5$

vert x oob

$x_{rom} = 57.5$

$y_{rom} = 40$

$a = 40$

$s = 97.5$

Screw overlap must be at least holder x dim − x rom

Is that true? that they are the same s?

horiz x oob

$x_{rom} = 77.5$

$y_{rom} = 20$

$a = 20$

$s = 97.5$

Pros

- Potential for stiffness
- Simple

Cons

~~Bolt~~

- Ballscrew
- very over constrained

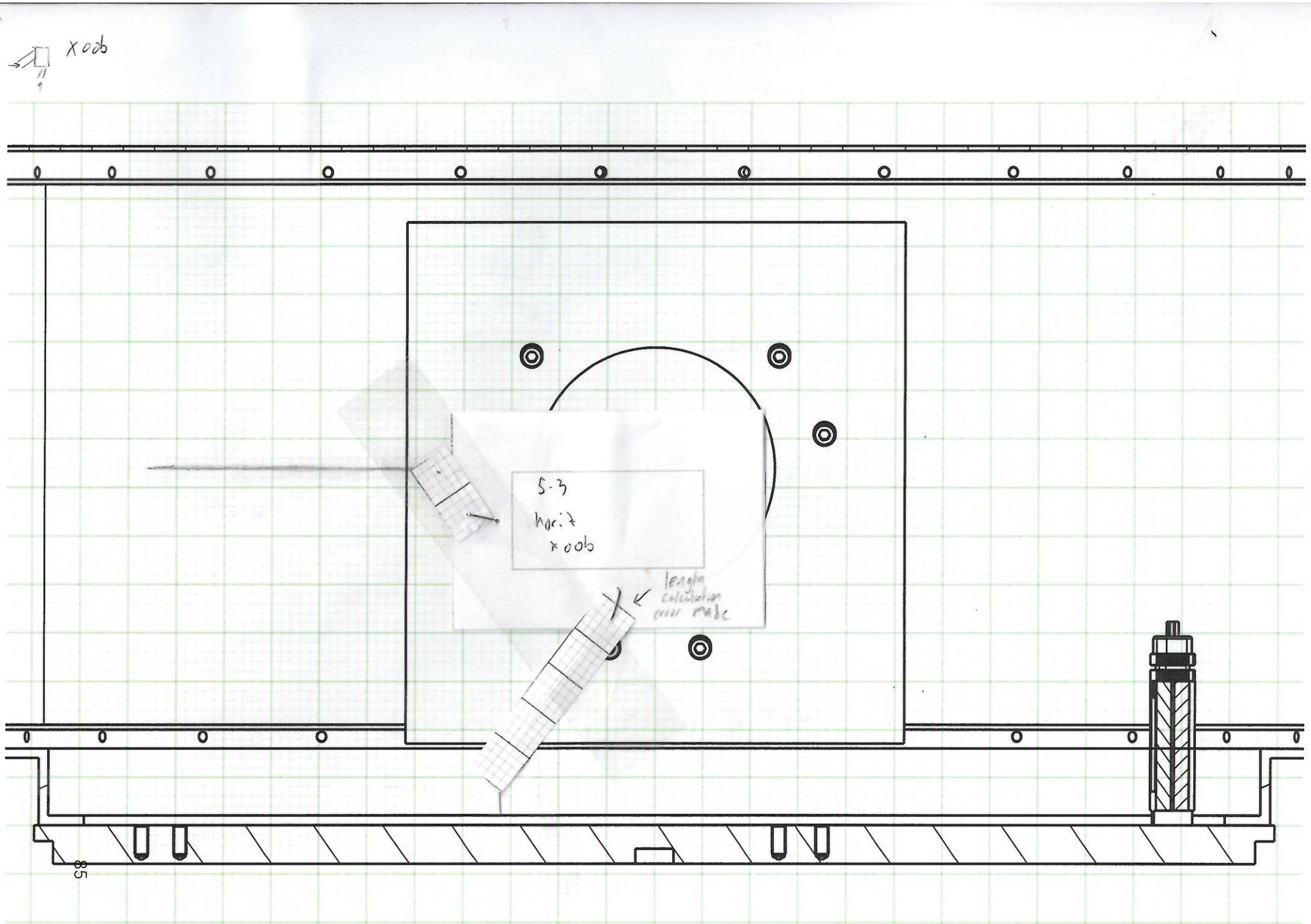

grid 2mm - bold 10mm

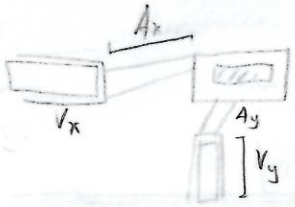

V_x = x rom $A_x = \frac{1}{2}$ y rom

V_y = y rom $A_y = \frac{1}{2}$ x rom

makes sense they are the same they are just 90° rotated

horiz

y oob

yrom = holder thick + LVF short + radius
= 12.5 + 20 + 25
= 57.5

xrom = LVF long
= 40

V_x = 40 A_x = 28.75

V_y = 57.5 A_y = 20

x oob

yrom = 20

xrom = holder thick + LVF long + radius
= 77.5

V_x = 77.5 A_x = 10

V_y = 20 A_y = 38.75

Vert

x oob

yrom = 40

xrom = 57.5

V_x = 57.5 A_x = 20

V_y = 40 A_y = 28.75

Pros

- good potential for stiffness

Cons

- 90° of joint flexion required
- linear guide required for the VCA

1.1 Serial RR w/ parallelograms driven by belt (or chain)

radial/axial DC motor

Koese, 2021

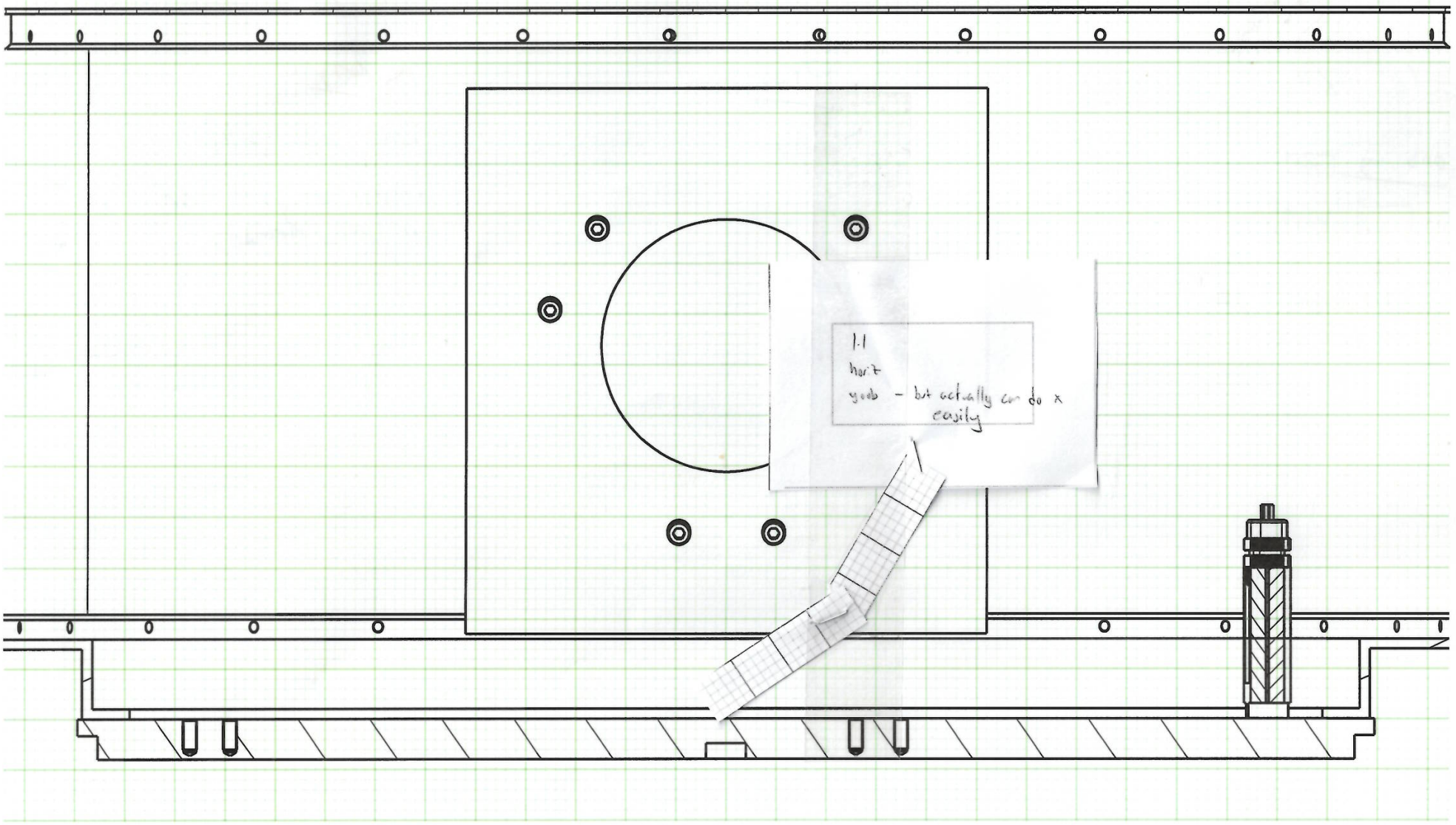

m - ~~bold~~ 5mm
grid 2mm
bold 10mm

- horizontal or vertical LVF?
- x or y out?
- link lengths?

oob -y

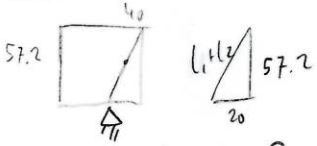

equal lengths? IDK

30.5 x 2

Pros

- simple

Cons

- very not stiff
- motor in joint or a belt needed

E Mechanism Offset Supplement

The diagrams are shown on the following page.

This is a supplementary explanation, along with diagrams, for the derivation of the mechanism offset equation;
$mechanism\ offset = LVF\ holder\ width + \frac{1}{2}ROM_{x\ margined} + \frac{1}{2}L_c + \frac{1}{2}(parallelogram\ width - LVF\ total\ width)$.

- The LVF shown in the diagrams serves only as a reference for dimensions. This is not the real positioning of the LVF within the cryostat.
- The black dashed line denotes the center of the cryostat.
- The origin of the mechanism is positioned at the base of the left arm.
- The orange dashed line denotes the $L_c/2$ line of the mechanism.
- The orange line with arrows at both ends denotes the difference between parallelogram length and the total width of the LVF; $parallelogram\ width - LVF\ total\ width$. The vertical line on this line denotes its midpoint.

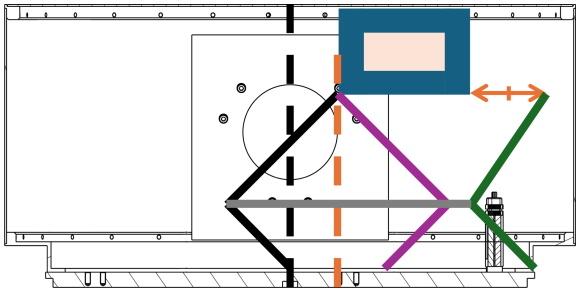

(a) The mechanism starts with its origin aligned with the center of the cryostat.

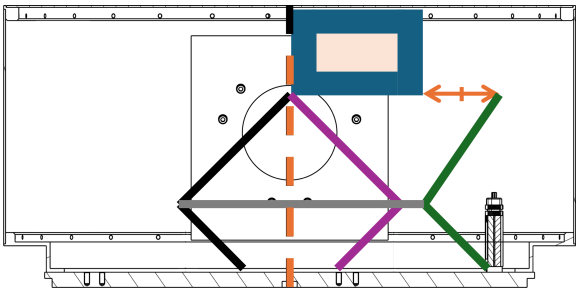

(b) The mechanism is shifted to the left by $\frac{1}{2}L_c$.

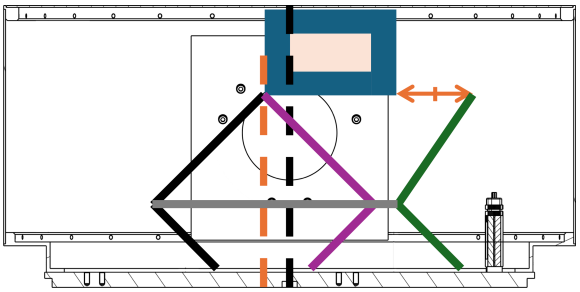

(c) The mechanism is shifted to the left by one $LVF\ holder\ width$.

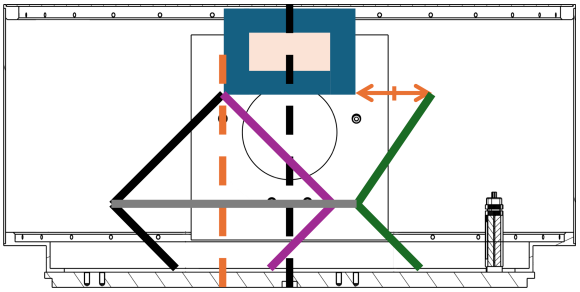

(d) The mechanism is shifted to the left by $\frac{1}{2}ROM_{x\ margined}$ (in this case equal to the X dimension of the LVF). This step, along with the previous two, results in the LVF (or more precisely said the workspace of the mechanism) being positioned symmetrically in the cryostat with respect to the black dashed line.

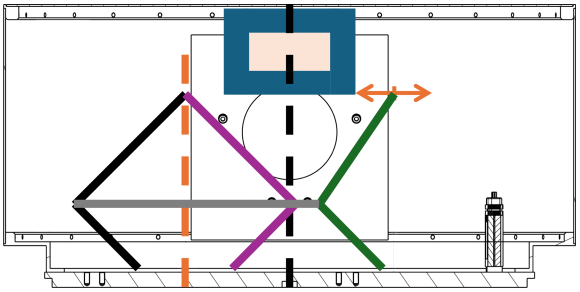

(e) Lastly the mechanism is shifted to the left by $\frac{1}{2}(parallelogram\ width - LVF\ total\ width)$ (while the LVF is "left behind"). This results in the LVF being positioned centrally within the parallelogram of the mechanism.

Figure E.1: Supplementary diagrams for the derivation of the mechanism offset equation.

F Preliminary Design Phase - Optimal Triplet Investigation

F.1. Flexpivots

Within the model there are still unknowns, and therefore assumptions must be made. For example: the mass of the LVF and its holder are known to be 52 g, however like stated before, a bracket must be later designed to serve as the interface between the LVF and the mechanisms, and its mass is yet unknown. The mass of the bracket is given an estimation of 100 g, which is chosen to be generous. The links are given an estimated 5×5 mm cross section with a density of 2.7e−6 $\frac{\text{kg}}{\text{mm}^3}$, corresponding to that of aluminum. The LVF has a size of 40×20 mm with a holder of width 12.5 mm around each edge. The ROM required of the mechanism is 77.5×20 mm. The motor is assumed to be a VSS-19 stepper motor with a gearbox of ratio 245:1 attached (hereafter to be referred to as a 245 gearbox). The stepper motor has a detent torque of 0.9 Nmm and the gearbox has an efficiency of 80 % [8]. This stepper motor and gearbox combination results in a detent torque of 176.4 Nmm. The gearbox is the highest ratio gearbox available for the smaller VSS motors and therefore can not be increased. The gearbox is able to support radial loads of 30 N. The origin of the mechanism is offset from the floor of the cryostat by $10.25 + 19/2 + 2 = 21.75$ mm, where the 19 comes from the diameter of the assumed motor, the 10.25 from the offset required for BIORAD compatibility, and the 2 allows for some material thickness. This will be called *floor offset*. Flexpivots are given a maximum angular flexion of ±15°, which is the absolute maximum flexion of an unloaded 10-series flexpivot for infinite life. They are assumed to be the smallest double-ended flexpivots available from C-Flex (AD-10), which have an undeflected maximum radial load capacity of 20.4 N [12]. This is smaller than the radial load capacity of the gearbox, and is therefore used as the maximum tolerable value for joint radial load. Lastly, the parallelogram is given a width equal to the total width of the LVF (65 mm). Many of these assumptions are of no consequence. For example the motor and gearbox assumption sets the maximum torque. If it is discovered that the selection of this motor results in stringent constraints, a larger motor with more torque can be assumed. This motor was chosen for the space savings as it allows the mechanism to be positioned lower and therefore offers more vertical space.

Applying the above assumptions results in 90,937 123ms-viable triplets. Their distribution is shown in the scatter plot below.

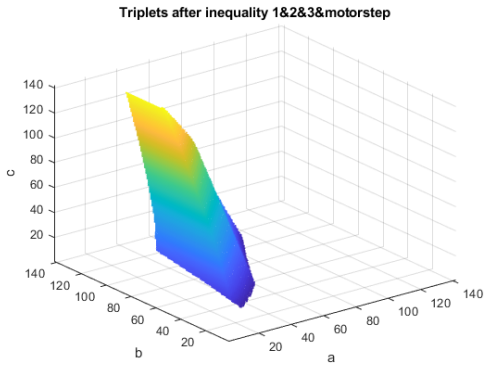

Figure F.1: The triplets left after inequality 1, 2, 3, and the precalculated motor step requirement for a gearbox with a 245:1 ratio.

The UpSet plot below shows the intersections of different passing triplets within the set of 123ms-viables. An UpSet plot can be seen as a multi-dimensional Venn-diagram. It shows the intersections between the different performance metrics. For example, the first bar shows that within the 123ms-viables, every

single triplet has a sufficiently low maximum joint load and maximum motor torque requirement for the assumed flexpivots and motor.

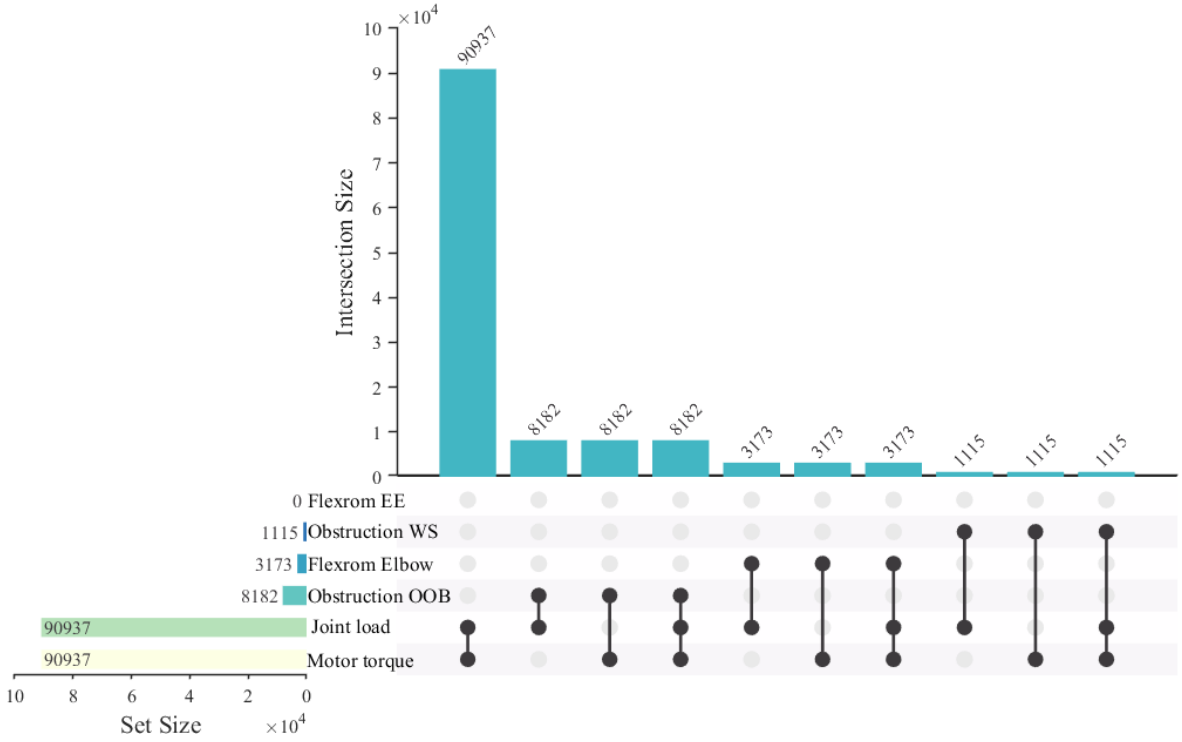

Figure F.2: UpSet plot 1. The total number of 123ms-viable triplets is 90,937 (where the motor step requirement is set by the 245:1 gearbox)

The UpSet plot above (Figure F.2) also shows that there are no triplets where the joint flexion ROM of the LVF joint is small enough to employ flexpivots. One assumption that effects joint flexion ROM is the floor offset. This can never be lower than 19/2 as the motor has a diameter of 19 mm. However the 10.25 mm in the offset is a result of the desire to have compatibility with the BIORAD. To investigate whether or not this compatibility requirement prevents the use of flexpivots in the LVF joint this 10.25 mm can be removed from the offset, resulting in floor offset of $19/2 + 2 = 11.5$ mm. This results in the following UpSet plot (Figure F.3) consisting of 104,216 123ms-viable triplets. 13,284 triplets have been gained, however no significant benefits are provided. There are still no triplets where the LVF joint flexion ROM is small enough to use flexpivots. Furthermore, no new intersections, and therefore no new functionality, arises. BIORAD compatibility is strongly desired, and due to the fact that its elimination poses no real benefits, the choice is made to keep the compatibility, and thereby the additional 10.25 mm in the floor offset. All further plots will be BIORAD compatible.

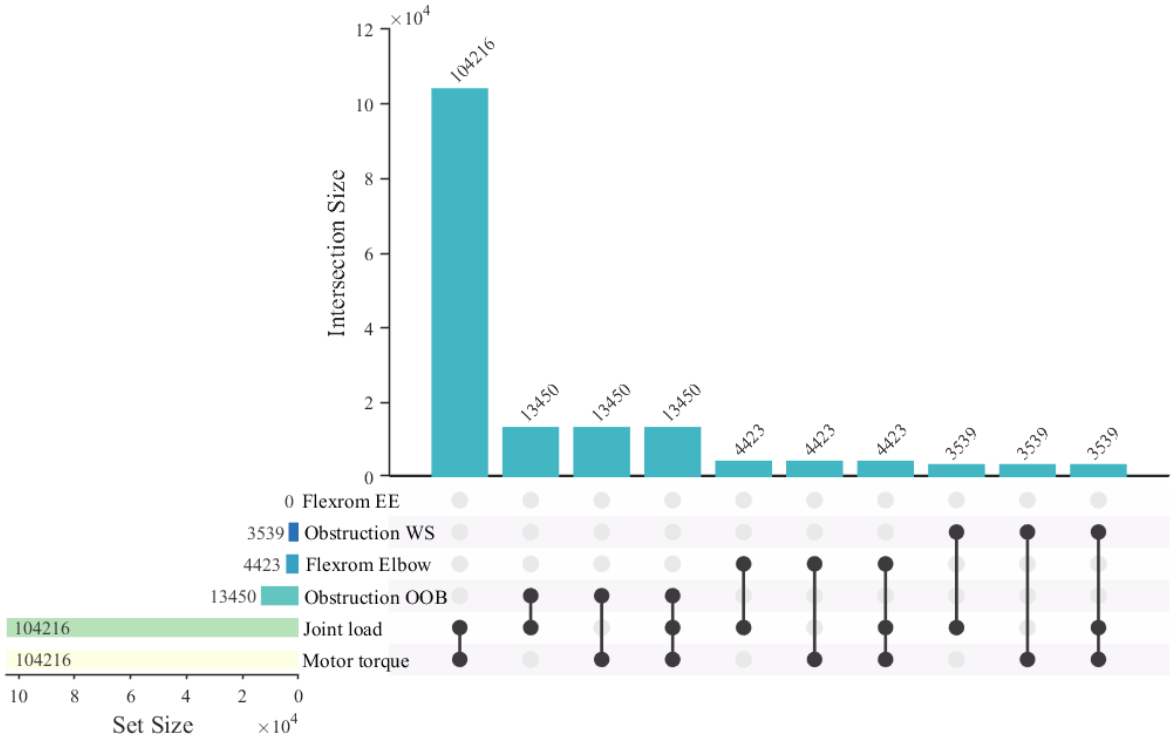

Figure F.3: UpSet plot 2. Floor offset reduced by 10.25 mm as to evaluate the effect that BIORAD compatibility has on the available triplets. The total number of 123ms-viable triplets is 104,216 (where the motor step requirement is set by the 245:1 gearbox)

Looking once again at the first UpSet plot (Figure F.2), is is clear that the torque of the smallest VSS stepper motor is already sufficient, and that the radial load capacity of the smallest flexpivots is also already sufficient. Out of the 90,937 123ms-viable triplets represented in the plot, not a single one requires a torque that exceeds the capacity of the VSS-19 and the limit for the radial load of the flexpivots. Furthermore, when disregarding the bottom two rows of the UpSet plot, which represent joint load and motor torque and are inherently passed by every triplet, two critical observations can be drawn. Firstly, there are no intersections left at all. Optical obstruction OOB, optical obstruction WS and elbow joint flexion ROM, are mutually exclusive. Opt to chose one, and be forced to concede the other two. This presents a significant challenge, as it suggests that optical obstruction is inevitable. For example, choosing to avoid optical obstruction in the WS necessitates obstruction in the OOB position. However, having no optical obstruction in both the WS and the OOB position required, and therefore a solution must be found. Secondly, resulting from the same mutual exclusivity, any triplet that is flexpivot compatible has optical obstruction both in the WS and OOB. This means that the limitations imposed by the flexpivots make both types of optical obstruction unavoidable. This observation is kept in mind while proceeding to the next step: analysing histograms to gain a deeper understanding of the data that is presented within the UpSet plot. Currently the only data presented is binary, pass or fail. Histograms will be presented of the different performance metrics to gain insight into the distribution of the performance of the triplets.

Plotting the histogram of the required motor step for 123-viable triplets results in the following plots. It is clear that stepping the LVF in Y-direction is more demanding than stepping it in X. Every single 123-viable triplet is capable of sufficiently small LVF steps in X direction with the 245 gearbox. This is not the case for steps in Y direction. The Y-direction histogram shows that there are a significant number of triplets cut off by the motor step requirement. The next (substantially larger ratio) gearbox is a 400:1. this gearbox however is only available for motors with a diameter of 52–57 mm. The constraint line that this 400 ration gearbox would impose is plotted as a dashed red line. The gain in available triplets is deemed to be less valuable than using a smaller motor and gearbox and the space savings and lower price that come along with it.

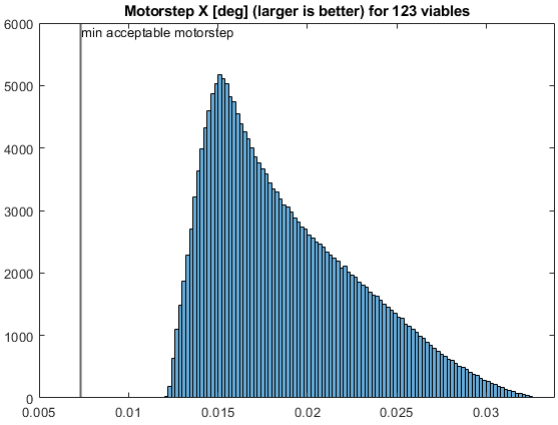

(a) X direction

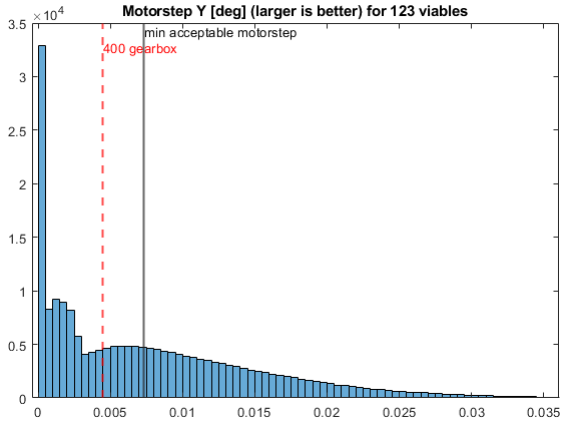

(b) Y direction

Figure F.4: Histograms of the minimum motor angular step required to step the LVF the desired 25 µm in a given direction of a given triplet. The triplets represented in the histograms are 123-viable.

The histograms of motor torque and joint load for 123ms-viable triplets show what the UpSet plot already showed: the VSS-19 stepper motor provides sufficient detent torque and the flexpivots are resistant enough to the radial loads on the joints.

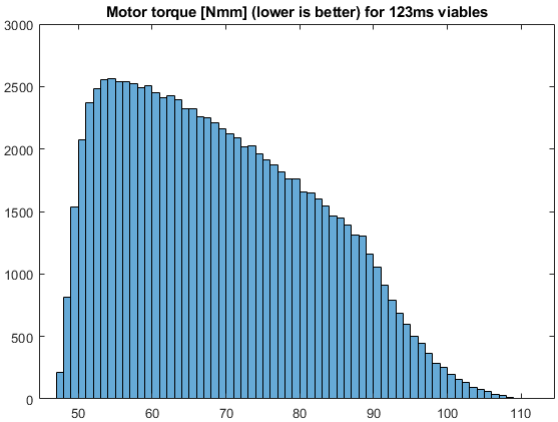

(a) Required motor torque. The vertical line that denoted the maximum acceptable radial load is placed at 176.4 Nmm and has been omitted to increase visibility of the histogram.

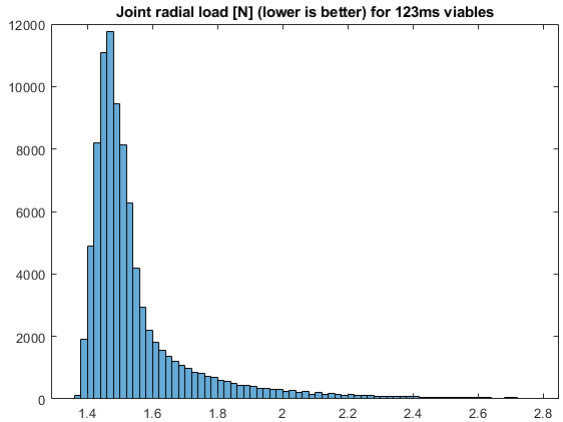

(b) Maximum joint radial load. The vertical line that denoted the maximum acceptable radial load is placed at 20.4 N and has been omitted to increase visibility of the histogram.

Figure F.5: Histograms of the maximum required torque and joint load within the WS of a given triplet. The triplets represented in the histograms are 123ms-viable.

The histograms of optical obstruction distance for 123ms-viable triplets shows that optical obstruction is a very limiting condition. The two discontinuities in the histogram in Figure F.6b occur at -27.5 and -2.5; respectively relating to the center-line of a link passing through the center of the window, and the center-line of a link being tangential to the circle of the window. These discontinuities have been verified to not be caused by a bug or inconsistency in the MATLAB code. They are both simply artifacts resulting from the constraints and kinematics of the system. Two representations of example triplets exhibiting the behaviour that causes the discontinuities are displayed in Figure F.7.

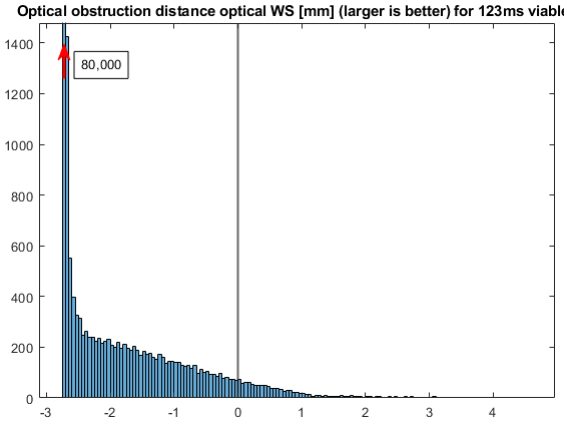

(a) Optical obstruction in the optical WS. The leftmost histogram bar (containing approximately 80,000 triplets) has been truncated to increase the visibility of the other bars.

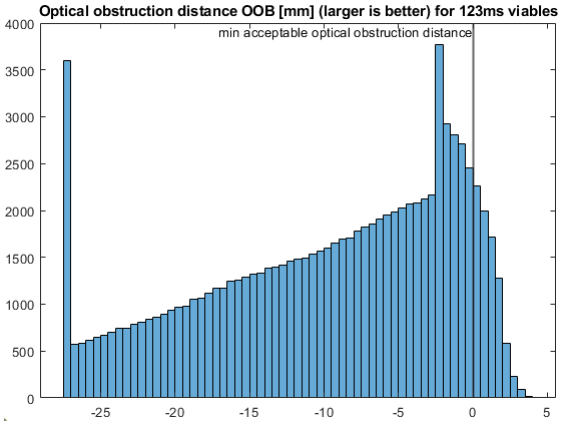

(b) Optical obstruction in OOB position.

Figure F.6: The minimum distance within the WS of a given triplet from the infinitesimally thin line that represents the link and the point at the center of the window of the cryostat. A negative number therefore means that there is optical obstruction. The triplets represented in the histograms are 123ms-viable.

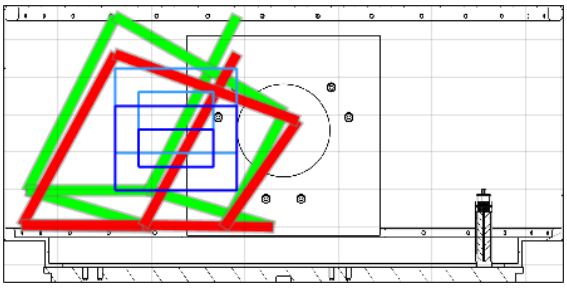

(a) A triplet showing that in-between these two positions, there is one position where a link of the mechanism passes directly through the middle of the window, resulting in an optical obstruction of -27.5.

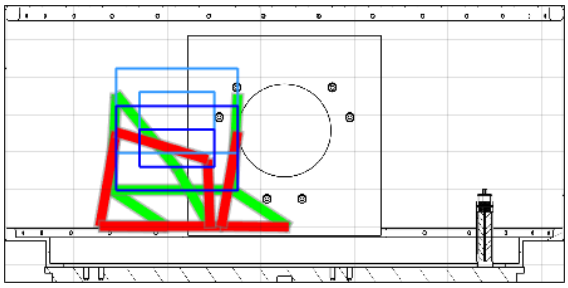

(b) A triplet showing that in between these two positions, there is one position where the center-line of a link of the mechanism is exactly a tangent line of the circle of the window, resulting in an optical obstruction of -2.5.

Figure F.7: Two cryostat representations of triplets to explain the discontinuities in the OOB histogram.

The histograms for the joint flexion ROM's show that quite a large flexion ROM would be required in order to be able to make all joints flexpivots. While strongly discouraged and undesirable, a possible solution is to mount two flexpivots in series. Theoretically this doubles the possible flexion ROM of the joint, however due to the less then optimal loading of the flexpivots, the load capacity of the assembly reduces, thereby reducing the infinite life flexion ROM of the assembly. However, due to the very low loads in the joints of the mechanism this may not be an issue, and is worth investigating. The loads in the joints are almost certain to be less than 2 N (as shown in Figure F.5b). In private communications, C-Flex recommended G-10 flexpivots for series flexpivots for this application. A G-10 flexpivot (12.7 mm diameter), which normally has a load capacity of 255.3 N [12], has a load capacity of 8.9 N when used in a series configuration: a 28.6 times reduction. Assuming a load of 2 N corresponds to 22.5 % of the maximum load capacity of the series flexpivot assembly. Using the life expectancy diagram from [12] (shown in Figure F.8) it can be derived that a maximum load of 22.5 % corresponds to a maximum flexion ROM of approximately 87.5 %. This leads to the series flexpivot assembly having an approximate total flexion ROM of $15 \cdot 2 \cdot 0.875 = \pm 26.25°$, where 15 is the standard maximum infinite life flexion ROM of an unloaded 10-series flexpivot, times 2 because there are two flexpivots in series, and times 0.875 for the reduction in flexion ROM due to the load. This gain in joint flexion ROM is significant, and the effect it has on the mechanism is shown in the UpSet plot in Figure F.10. In this UpSet plot the joint load and motor torque categories have been omitted as it is already known that every triplet passes these, and omitting them will increase the readability of the plot.

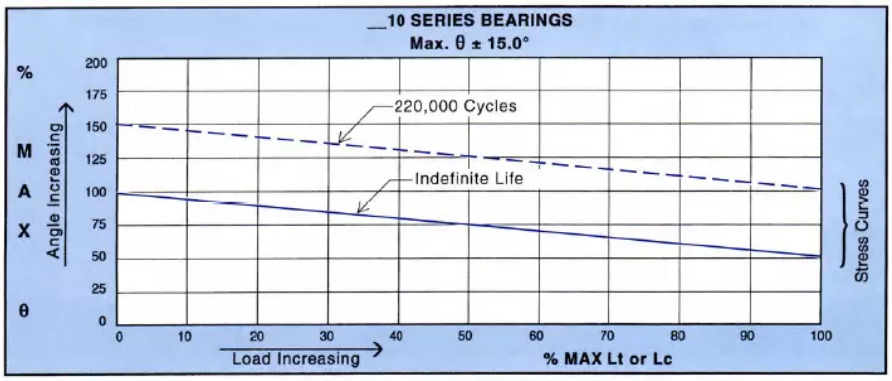

Figure F.8: Life expectancy diagram for a C-Flex 10-series flexpivot [12].

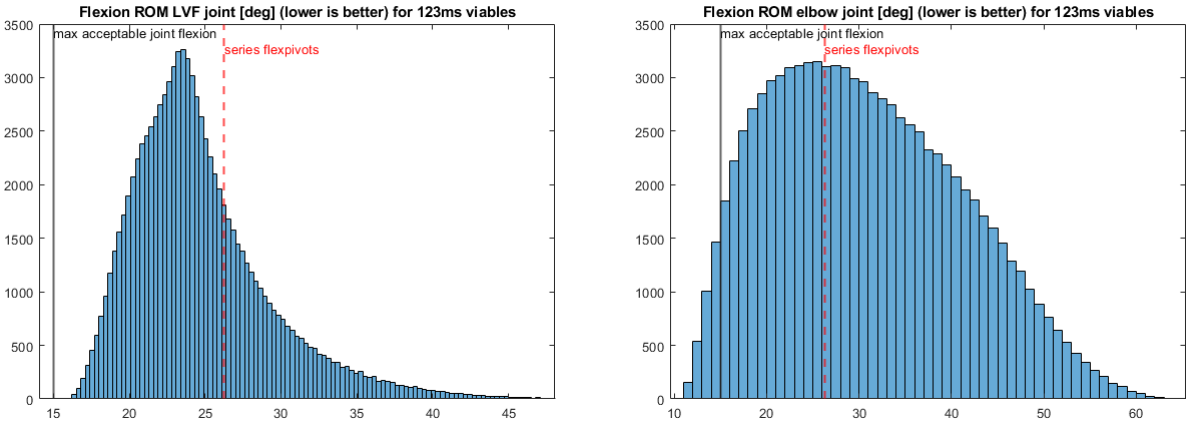

(a) LVF joint flexion ROM

(b) Elbow joint flexion ROM

Figure F.9: Joint flexion required to move the LVF over the given WS. The triplets represented in the histograms are 123ms-viable. A red dashed line is placed at the maximum flexion ROM of a series flexpivot assembly.

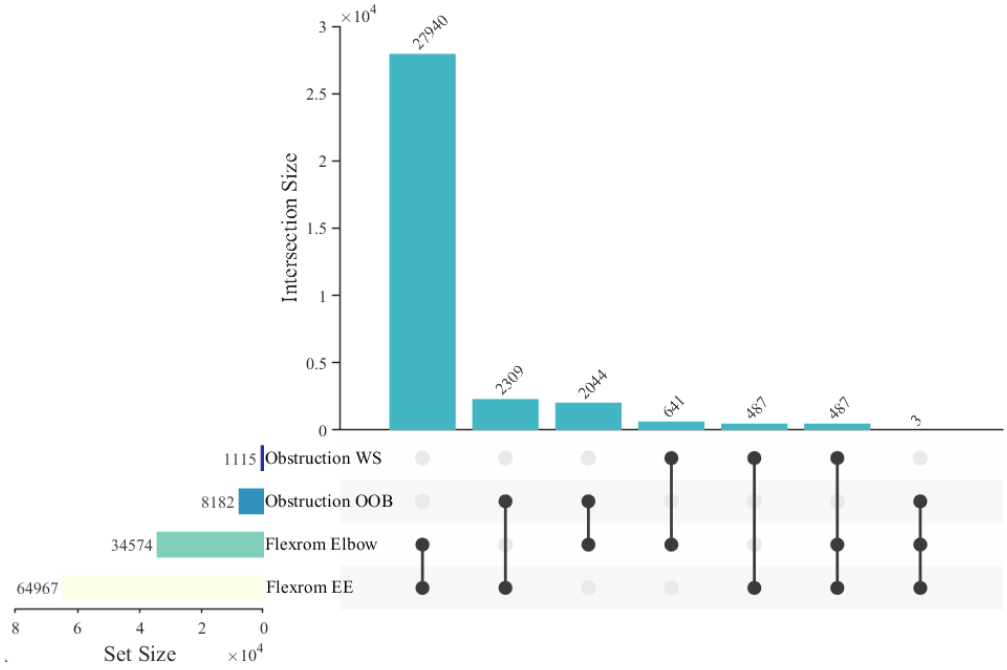

Figure F.10: UpSet plot 3. Assuming series flexpivots in the joints. The total number of 123ms-viable triplets is 90,937 (where the motor step requirement is set by the 245:1 gearbox)

Clearly new intersections, and therefore new functionality, has been gained by applying series flexpivots. However, still no triplets exist in the intersection of: flexpivots in every joint and no WS and OOB optical obstruction. There are 487 triplets that have flexpivots in every joint and no optical obstruction in the WS, and there are 3 triplets that have flexpivots in every joint and no OOB optical obstruction. Within each intersection, the least obstructing triplet can be found. Within the set of triplets with series flexpivots in every joint and no WS optical obstruction, the triplet with the least amount of OOB optical obstruction is found, and is shown in Figure F.11. Similarly, within the set of triplets with series flexpivots in every joint and no OOB optical obstruction, the triplet with the least amount of WS optical obstruction is found, and is shown in Figure F.13. First the triplet without WS optical obstruction (Figure F.11) is considered. Firstly, this triplet has extremely long links, leaving almost no margin before they crash into the sidewall or ceiling of the cryostat. Essentially this already makes this a failing triplet, as currently no extra width is given at the joints, which would have to be there, to account for the size of the flexpivots. The links are currently 5 mm wide. Even if smaller diameter flexpivots were used (given that their load capacity was sufficient) some space has to be given to the material surrounding the flexpivot. The links will almost certainly need to be a double-ended "lollipop" shape, with extra width around each joint as a result of the flexpivots and the material required to surround them. Furthermore, the OOB optical obstruction of this triplet is bad, the elbow joint of the right arm passes straight through the middle of the cryostat window. This triplet is too poor of a performer to be considered.

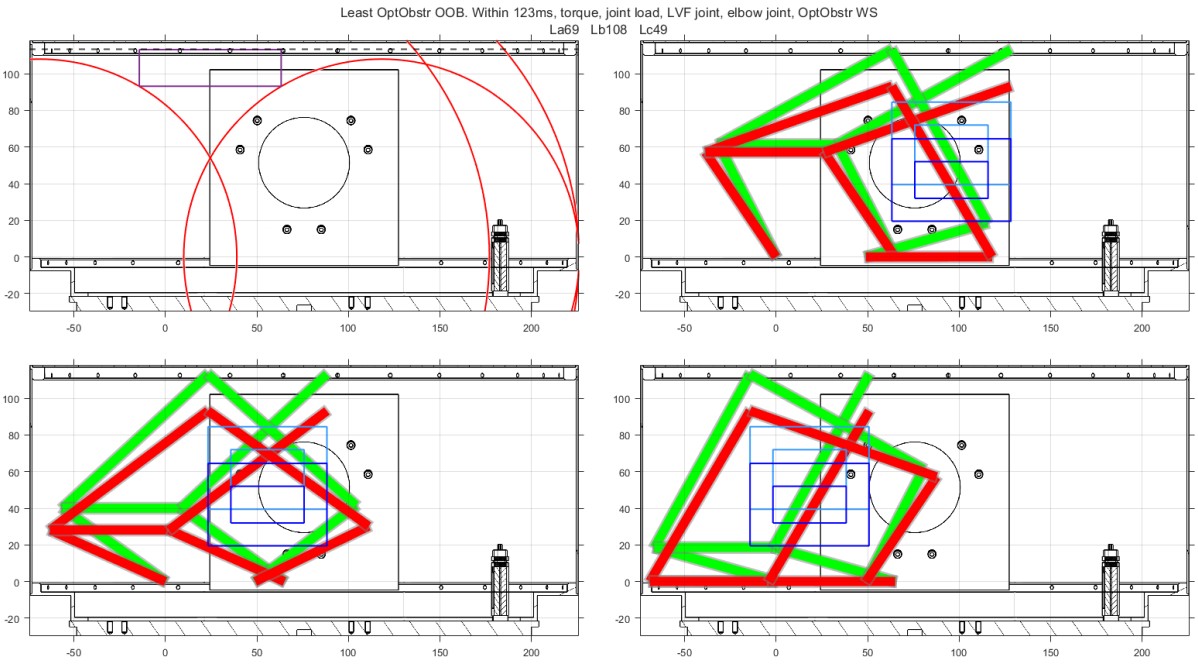

Figure F.11: A representation of a triplet within the cryostat. The triplet has series flexpivots in every joint and, no optical obstruction in the WS, and optimizes for having the least amount of OOB optical obstruction.

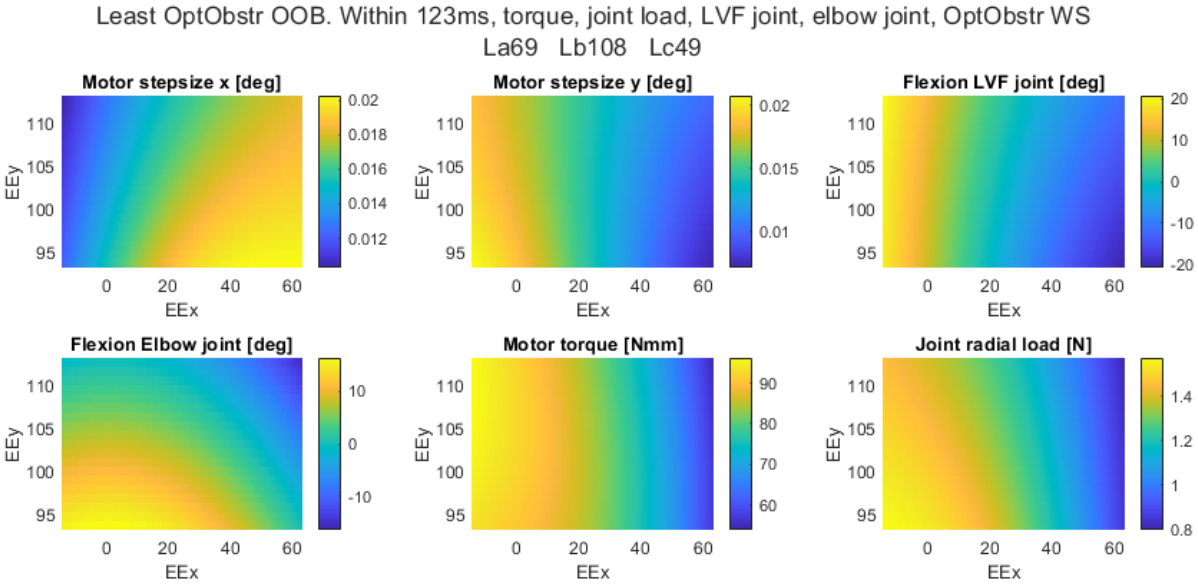

Figure F.12: The heatplots of different performance metrics over the WS of a triplet. The triplet has series flexpivots in every joint and, no optical obstruction in the WS, and optimizes for having the least amount of OOB optical obstruction.

Next, the triplet without OOB optical obstruction (Figure F.13) will be considered. The link lengths here are much more manageable, and have some margin between the walls and ceiling. There is also some margin between the WS and the singularity curves. The link that causes the WS optical obstruction is the B-link of the parallelogram arm. Increasing the parallelogram length will move the entire parallelogram arm (and therefore also the B-link) to the right, and decreasing it will move the arm to the left. Both are options and would move the parallelogram arm out of its obstructing position as shown in the top right subplot. Moving the arm to the left by only a couple of mm would potentially already result in sufficient clearance. Moving the arm to the right would mean moving it by the entire diameter of the window (50 mm) as to not induce OOB optical obstruction. The right arm of the 5-bar

mechanism also comes close to causing OOB obstruction, and it would cause OOB obstruction if the lollipop shape is taken into account. However, once again, the entire mechanism can be shifted to the left to create sufficient clearance. Though both of these options, shifting the parallelogram arm left or right, or shifting the 5-bar mechanism left or right, will result in being required to mount the LVF not centrally within the parallelogram. Another option to aid in solving the WS optical obstruction is to use curved links. The links are not required to be straight. If the B-link of the parallelogram arm was curved like a segment of a circle, it could potentially aid in avoiding the WS optical obstruction. The optical obstruction is however very close to the joint, and a curved shape may not help.

This triplet still does not provide a position for the collimated measurement mode, where no part of the optical area may be obstructed. Once again this could be aided by shifting the arms around; moving the mechanism to the left and the parallelogram arm either to the left or right.

In conclusion, series flexpivots are undesirable, and the limited gain they pose for mechanism performance is deemed to be insufficient to justify their use. Series flexpivots are deemed to be less desirable components than ball bearings due provide more limited performance. Therefore, ball bearings are preferred, as they will offer far greater flexibility in mechanism design due to their unlimited angular ROM. Additionally, as series flexpivots struggle to provide viable mechanism solutions for the 40×20 mm LVF, finding valid solutions for the 55×25 mm LVF will be an even greater challenge.

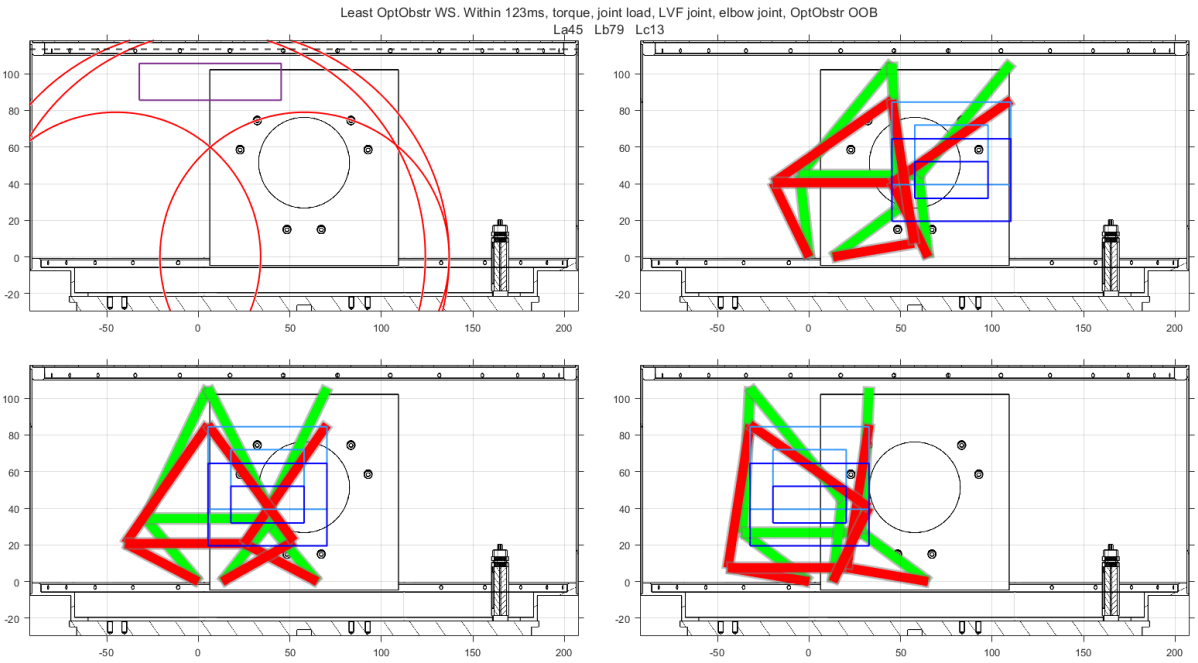

Figure F.13: A representation of a triplet within the cryostat. The triplet has series flexpivots in every joint and, no optical obstruction in the OOB position, and optimizes for having the least amount of WS optical obstruction.

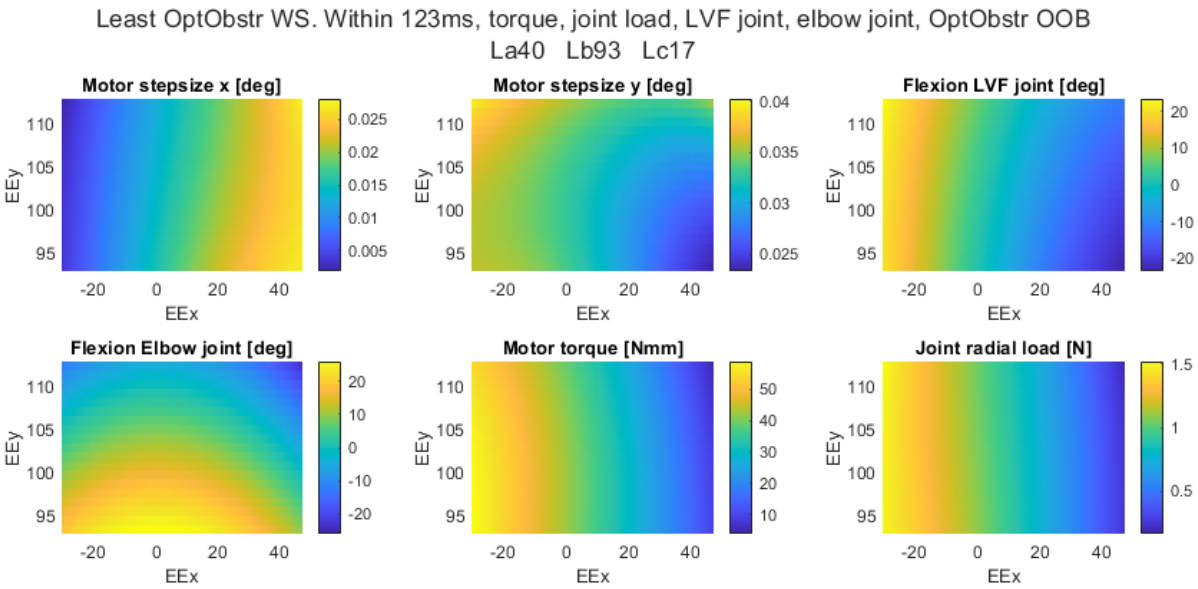

Figure F.14: The heatplots of different performance metrics over the WS of a triplet. The triplet has series flexpivots in every joint and, no optical obstruction in the OOB position, and optimizes for having the least amount of WS optical obstruction.

F.2. Ball Bearings

Due to the mutual exclusivity of the upper four sets (optical obstruction OOB, optical obstruction WS, flexpivot LVF, flexpivot elbow) in first UpSet plot (Figure F.10) it is clear that even when assuming the use of ball bearings in every joint, thereby ignoring any joint flexion ROM constraints, still no triplets exist in the intersection between no optical obstruction in the WS and no optical obstruction in the OOB position. Once again, representations will be created of the least OOB and WS obstructing triplets within 123ms and joint load and motor torque viables. It is still known that, as before, every 123ms-viable triplet also is acceptable regarding joint load and motor torque. Notably, the triplet with no optical obstruction in the WS and minimal OOB obstruction is the same triplet as before, which was series flexpivot compatible (shown in Figures F.11 and F.12). The triplet without OOB optical obstruction and minimal WS obstruction is shown below and is quite similar to the triplet from before.

This leads to the conclusion that under the current assumptions, no triplets offer a solution as each one has either WS or OOB optical obstruction.

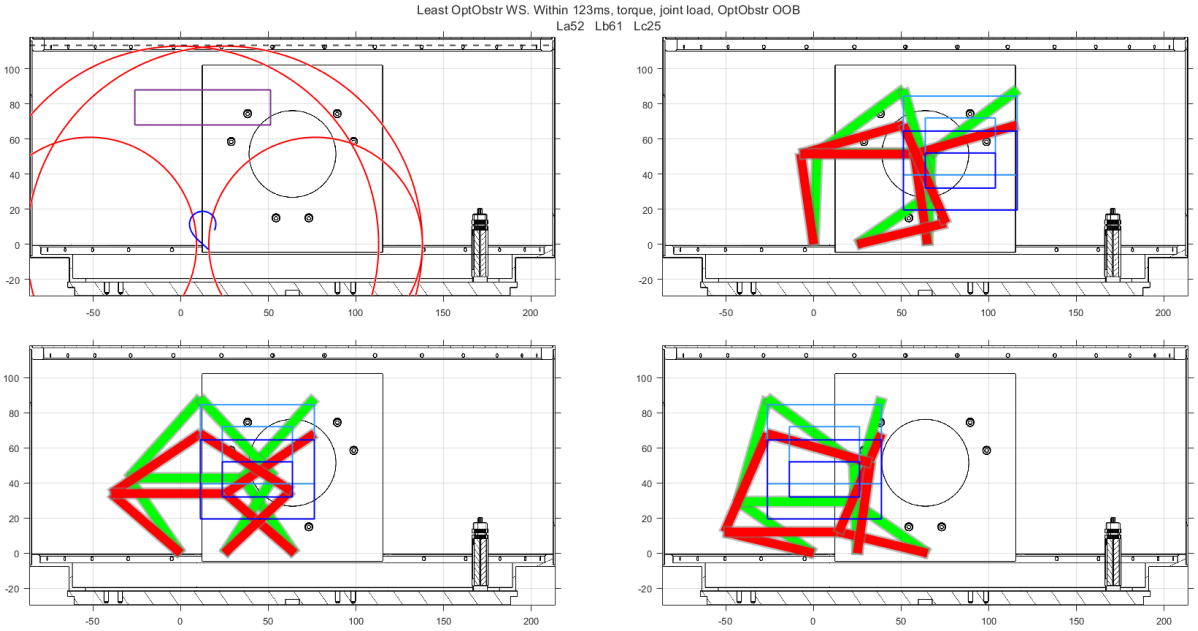

Figure F.15: A representation of a triplet within the cryostat. The triplet has bearings in every joint and, no optical obstruction in the OOB position, and optimizes for having the least amount of WS optical obstruction.

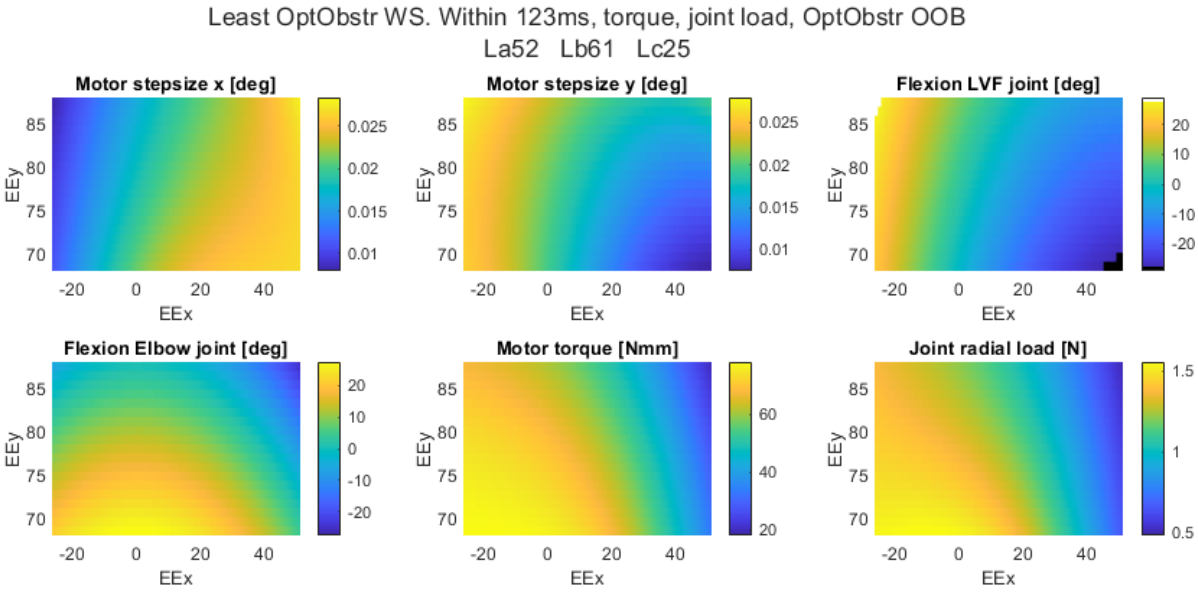

Figure F.16: The heatplots of different performance metrics over the WS of a triplet. The triplet has bearings in every joint and, no optical obstruction in the OOB position, and optimizes for having the least amount of WS optical obstruction. In the LVF joint flexion plot, the white in the top left corner and black in the bottom right corner show where the flexion would have been unacceptable if series flexpivots were used instead of bearings.

F.3. Reducing Rectangular ROM

In order to find a triplet without optical obstruction, the assumptions made previously must be evaluated. One assumption or design decision made is to enforce symmetry: the LVF is mounted in the middle of the parallelogram, and the $Lc/2$ line is right in the middle of the WS. This constraint could be loosened up to gain design freedom. However this will not be investigated as there is another, more critical, assumption made: setting the ROM to 77.5×20 mm. While it is true that the LVF must move at least 77.5 mm total in X-direction in order to clear the window of the cryostat, it is not true that while in the leftmost position the LVF must be able to move up or down 20 mm. The true rectangular

WS of the mechanism is only required to be $40 \times 20\,\text{mm}$, as long as there is a single OOB position that is sufficiently far to the left. Using Figure F.17 as a visual aid, the true WS can be set to $40 \times 20\,\text{mm}$ and the OOB position can be placed within the pink highlighted area to the left of the WS: which exists if the coordinate of the intersection point of the circles (marked with a black X) is sufficiently far to the left. The X-coordinate of the intersection point can be calculated using circle intersection equations [16] [17]. Triplets can then be eliminated where this point is not sufficiently far to the left. Another constraint is that the Y-coordinate of the intersection point between the smaller circle (radius L_b and origin at $(-L_a, 0)$) and the vertical dashed OOB line must be lower than the ceiling of the cryostat, otherwise the sufficiently far to the left OOB position can never be reached as the mechanism would crash into the ceiling. These two conditions (sufficiently far to the left and lower than the ceiling) are called inequality 4.

Reducing the ROM requirement to only the optical ROM ensures that the area in WS of the mechanism where the optical area of the LVF is scanned is placed directly above the center of the mechanism. Earlier, this area was placed off-center to the right in the total WS of the mechanism. This centered placement of the WS where performance is required is beneficial and results in more passing triplets. Looking at the motor step size Y plot in Figure F.16 shows that the most demanding (dark blue) motor steps are present in the right edge of the WS. Therefore, reducing the width of the WS and placing it centrally above the mechanism (which is equivalent to cutting off the left and right edges of the motorstep heatplot) will relax the motorstep requirement. Furthermore, as the mechanism is always calculated to be placed centrally under the WS, and the WS has become less wide while its right edge stays in the same place (as the position of the right edge of the WS is placed so as to place the left edge of the LVF on the laser beam), the mechanism as a whole, moves slightly to the right. This results in more triplets passing the inequalities that verify that the mechanism does not crash into the sidewall of the cryostat. Lastly, shorter links will also become viable, simply due to the fact that the mechanism is no longer being required to reach as far.

Flexpivot (or series flexpivot) compatibility will not be evaluated. This is due to limitations in the MATLAB model, as the calculations over the WS (which produce the heatplots) are only implemented only for the purple rectangle, and not the pink highlighted area. To find the best OOB position would require calculations over a grid of points within the pink area, like is done for the purple rectangle. Similar UpSet plots and heatplots can then be made to evaluate the OOB positions. The best OOB position may then be said to be the position in the OOB area which does not have any optical obstruction, and has minimal joint flexion. These OOB calculations over a grid of points were not implemented due to time constraints. The omission of flexpivots however is not as consequential as it may initially seem. This is due to the fact that in order to go OOB, the mechanism must still provide a ROM of at least 77.5 mm in X-direction. Meaning that at some point, the flexpivots still must be capable of bringing the LVF to what is essentially the left edge of any of the flexion heatplots shown previously. Therefore, although it does help, the reduction in required rectangular ROM does not significantly reduce joint flexion.

The viability of a triplet is influenced by the parallelogram length, which dictates the position of the parallelogram arm. The optimal parallelogram length, which prevents optical obstruction by the arm, varies across triplets. For instance, in Figure F.11, the currently assumed parallelogram length is suitable for long arms, as it does not cause optical obstruction in the WS or OOB position. However, for shorter arms (as depicted in Figure F.15), it is evident that a larger parallelogram length, enough to shift the parallelogram arm to the opposite side of the window, would be advantageous in minimizing optical obstruction. In summary, the parallelogram length should be either sufficiently small to position the parallelogram on the left of the window, or sufficiently large to place the entire parallelogram arm on the right side of the window. Additionally, the parallelogram length cannot be so small that it positions the attachment point of the parallelogram arm within the optical area of the LVF. The optimal parallelogram length is is narrowed in on through trial-and-error.

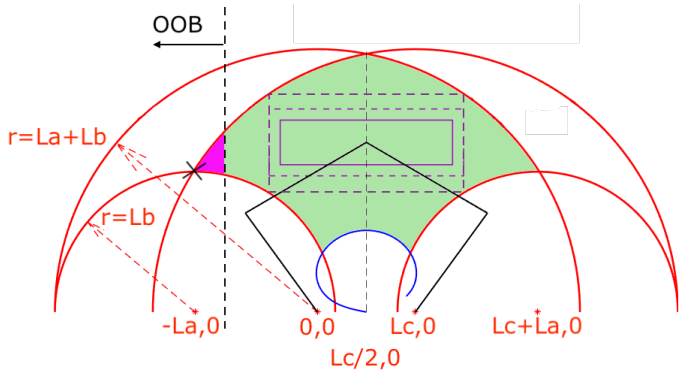

Figure F.17: The reachable area of the mechanism, showing that the OOB position can be placed in the pink area, allowing for the required rectangular ROM to be reduced from what was previously required.

An indication of the increase in design flexibility crated by reducing the ROM, while maintaining the same parallelogram length of 65 mm, is shown in the Venn diagram in Figure F.18. Previously, using the overly large rectangular ROM, there were 90,937 123ms-viable triplets. Using the reduced ROM has increased this to 222,034; more than doubling the number of available triplets. The Venn diagram shows how many of these triplets have no optical obstruction in the WS, and pass inequality 4. 66,841 triplets are able to move the LVF sufficiently far to the left while also providing no optical obstruction within the optical WS. This is a significant 60 times improvement over the 1,115 non-WS obstructing triplets available when assuming the overly large rectangular ROM. Among these 66,841 available triplets, some may still cause optical obstruction in the OOB position. Due to limitations in the MATLAB model this cannot be programmatically evaluated. However it is still clear that this reduction of the ROM has expanded the design possibilities.

The next step involves examining these triplets to identify the characteristics of high-performing triplets and to assess the situation regarding OOB obstruction. This subsequent exploration of available triplets and the design space is inherently iterative. The iterative exploration of the available triplets leads to learning which characteristics result in a favorable and high performing triplet, allowing for the narrowing down of the design space.

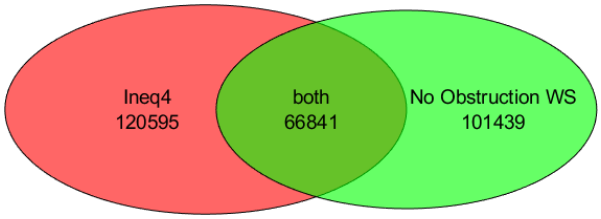

Figure F.18: Venn diagram of the 222,034 123ms-viable triplets for a 40 × 20 mm WS.

Through trial-and-error exploration of the available triplets it was determined that a smaller L_c is preferable. Triplets with a large L_c are unable to avoid OOB obstruction as L_c can never be large enough, nor the arms long enough, reach entirely around the cryostat window in the OOB position. Therefore, the L_c should be small enough in order to keep the right arm on the left side of the window, thereby avoiding OOB obstruction. This characteristic is shown in Figures F.19 and F.20 which depict triplets calculated for the 40 × 20 mm WS and optimized for both large and small L_c. The triplet with the largest L_c and the longest arms is unable to avoid OOB obstruction as it is incapable of reaching around the window. The smaller L_c triplet is a better performer, as it is nearer to avoiding OOB obstruction, and additionally is far more compact. This characteristic was also shown earlier in Figures F.11 and F.15, where the first has OOB obstruction and a large L_c, and the second has no OOB obstruction and a small L_c. Furthermore, even if these long arms and L_c did not suffer from unavoidable OOB obstruction, short arms and short L_c would be preferred as it reduces the total envelope of space occupied by the mechanism, and the large length triplets also impose small margins

between the mechanism and the walls and ceiling of the cryostat.

As such, a smaller L_c is preferred. The smaller the L_c, the more clearance the right arm has from the window. Increasing L_c only moves the right arm closer to the window, reducing the space available to it before there is OOB or collimated mode obstruction. This is also shown in the scatter plot of 1234ms-viable triplets in Figure F.21, which shows that as L_c increases, the number of triplets decreases. The choice was made to set L_c to be equal to zero, rather than search a design space where L_c ranges from 0 to some small number (for example 20 mm). This is due to the following reasons: firstly, the group of better performing triplets already already consists primarily out of small L_c triplets; secondly, little design freedom is lost, as most of the combinations of La and Lb present for slightly larger L_c's are also available when L_c=0; and lastly, there is a gain in manufacturing accuracy. Manufacturing tolerances, and their effects on mechanism performance are detailed further in Chapter 7.1, for now, consider a situation where L_c=3 mm. To manufacture this, the two holes that determine the motor location must be drilled in the floor bracket, with their centers 3 mm apart. This distance has some uncertainty due to the manufacturing tolerance. However, if L_c=0, the location of both motors can be determined by the same drill hole, therefore there is zero uncertainty in the position of the motors.

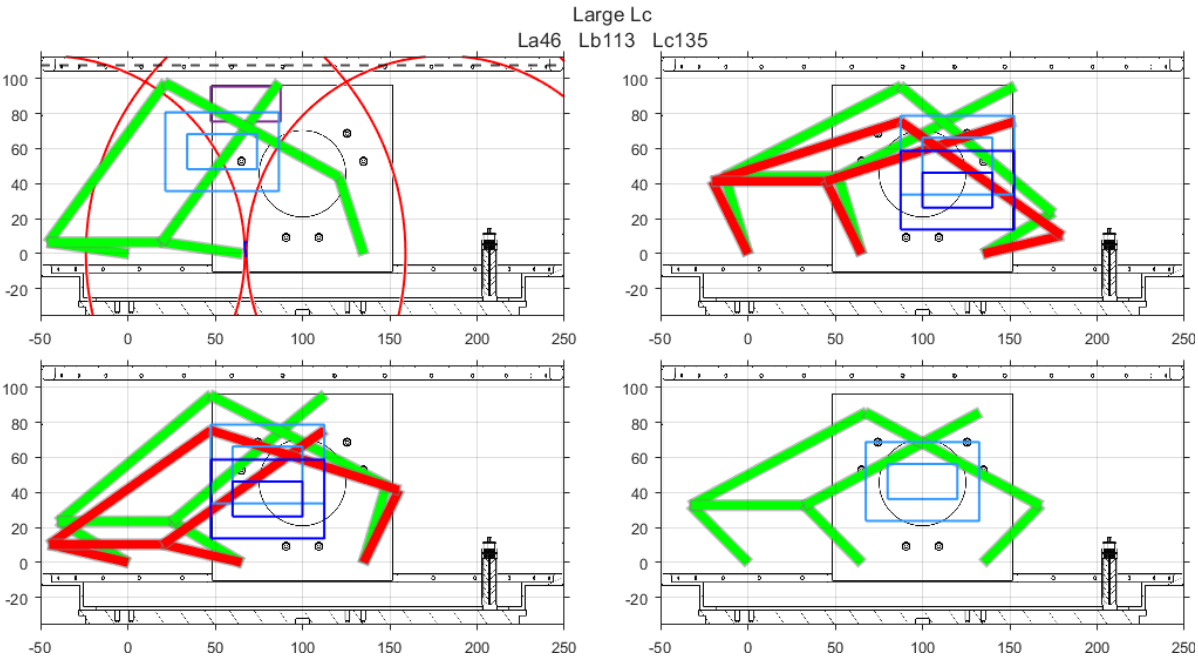

Figure F.19: A cryostat representation of a triplet with a maximised L_c, for a WS of 40 × 20 mm and a parallelogram length of 65 mm. Showing that there are no viable triplets where the right arm is able to reach around the cryostat's window.

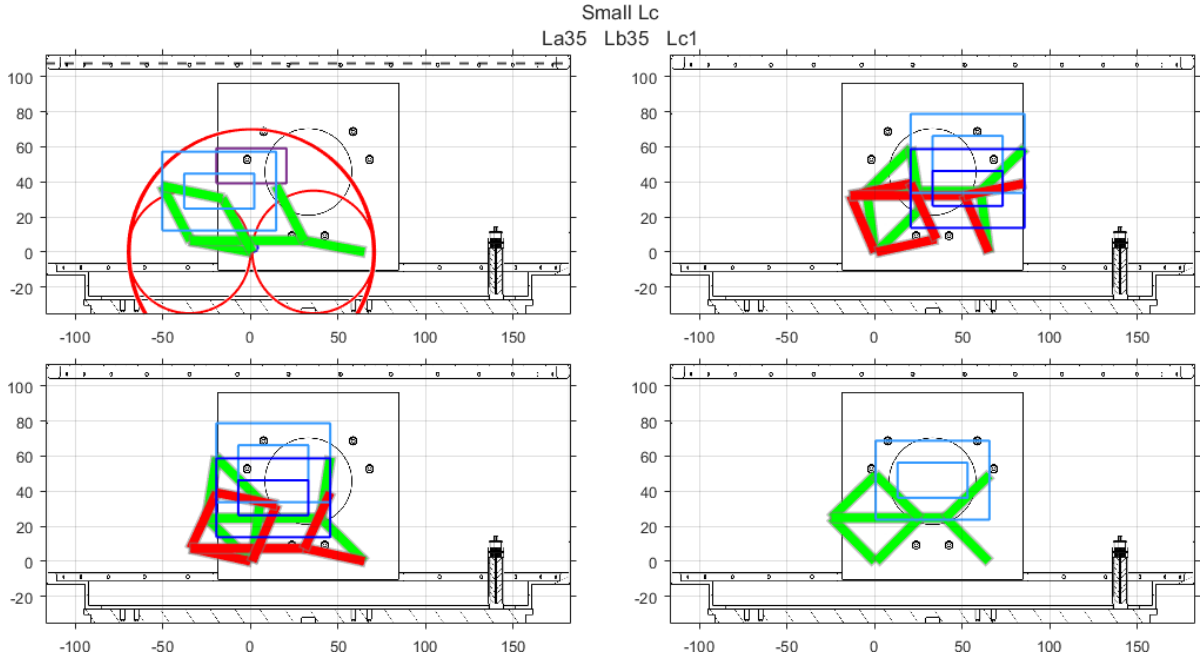

Figure F.20: A cryostat representation of a triplet with a minimized L_c, for a WS of 40×20 mm and a parallelogram length of 65 mm. Showing that these smaller L_c triplets are better performers as they have less obstruction issues.

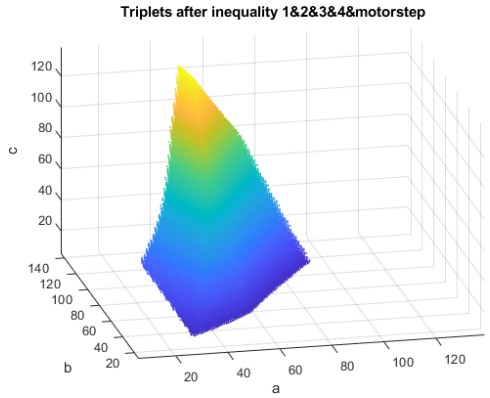

Figure F.21: The triplets left after inequality 1, 2, 3, the precalculated motor step requirement for a gearbox with a 245:1 ratio, and inequality 4. Showing that the number of viable triplets reduce as L_c increases.

Through development of the CAD model (detailed in Chapter 7.2) it was learned that the floor offset (for which the initial assumption was placed at 21.75 mm) must be updated to 27.5 mm. This is in-part due to updating the limiting diameter, from the 19 mm of the motor, to the 22 mm of the 245 gearbox; and in part due to more thickness being required for a stiff motor connection. As it is the gearbox diameter that is the limiting factor, this increase in floor offset is not due to the increase in motor diameter (resulting from the updated choice of the VSS-25 stepper motor, over the VSS-19). Additionally, it was learned that there is a limit on the maximum drive angle θ_1 due to collision of the parallelogram link with the motor axle. How the mechanism looks when driven with this maximum drive angle is now shown in the top left of the cryostat representation, as in F.22. This maximum drive angle is calculated using the equation for the Y-coordinate of the left elbow (simply $L_a \sin\theta_1$), and the width of the parallelogram link. Where it can be formulated that the minimum allowable Y-coordinate of the elbow joint is equal to $(link\ width + motor\ axle\ diameter)/2$, resulting in $\theta_{1\,max} = 180 - \sin^{-1}\left(\frac{(link\ width + motor\ axle\ diameter)/2}{L_a}\right)$.

The process of identifying the best triplet, while parallelogram length is a variable, involves two main steps. First, optimize the based on a specific criterion, in this case, maximum WS obstruction margin.

Following this, adjust the parallelogram length to ensure that the parallelogram arm does not introduce any obstruction issues. The chosen triplet is then visualized in two positions: the maximum OOB position, as is limited by the collision of the parallelogram link with the motor axle; and the collimated mode position, where the LVF is centered over the window

Joint flexion ROM is no longer a limitation, motor torque and joint load are not critical as they are passed by every triplet, and motor step is simply a requirement. This leaves only optical obstruction distance to optimize for. For a 40×20 mm ROM and 5 mm wide links, the maximum possible optical obstruction margin is 7 mm. This triplet is shown in Figure F.22 and Figure F.23. Coincidentally, and advantageously has a generous 8 mm of ROM margin.

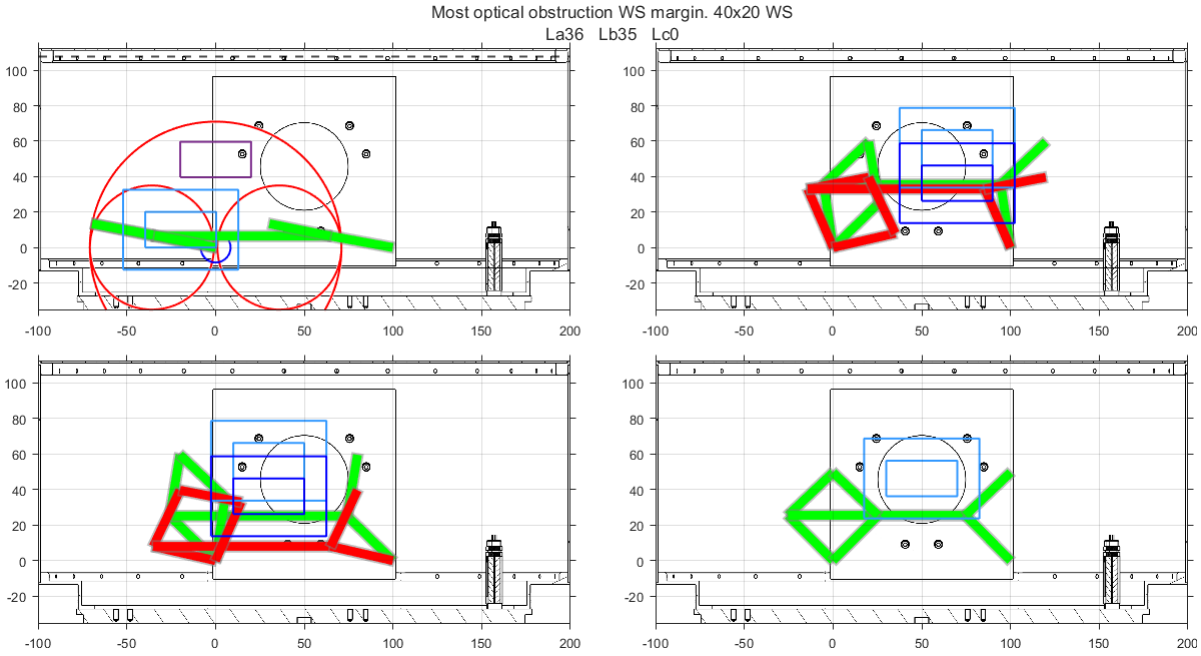

Figure F.22: A cryostat representation of the triplet optimized for the largest optical obstruction margin over a 40×20 mm WS. The triplet has 7 mm of optical obstruction margin and 8 mm of WS margin.

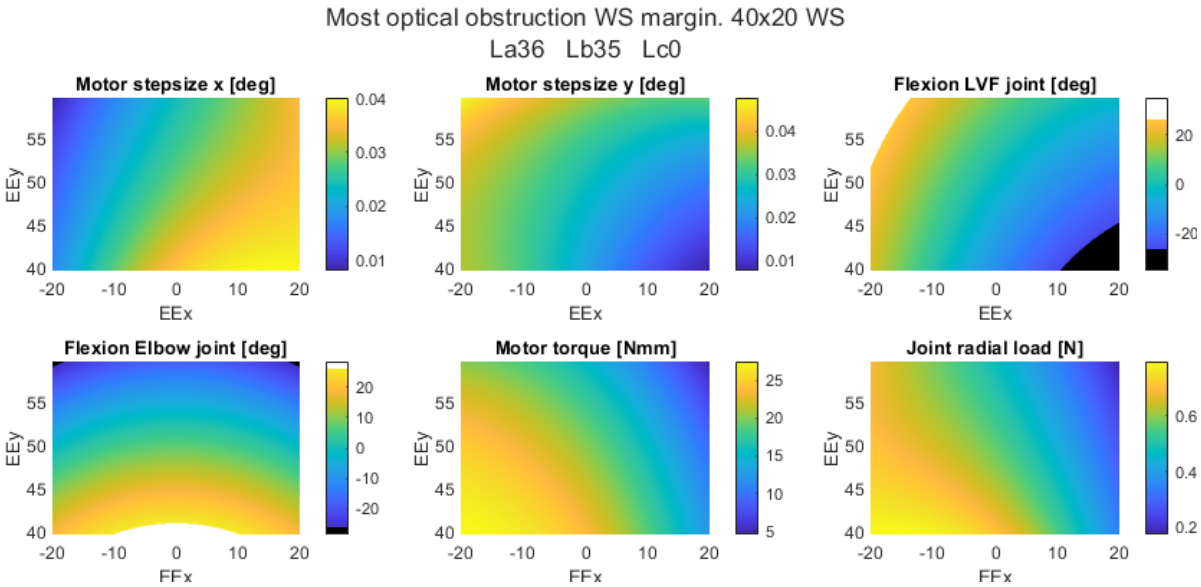

Figure F.23: Heatplots for the triplet optimized for the largest optical obstruction margin over a 40×20 mm WS. The triplet has 7 mm of optical obstruction margin and 8 mm of WS margin.

During the course of the thesis, it became evident that there may be a desire to scale up the dimensions of the LVF to $55 \times 25\,\text{mm}$. It is clear that allowing for the use of ball bearings, and reducing the rectangular ROM to only the required optical ROM has opened a lot of design possibilities. Thus it is valuable to asses the mechanism's ability to scan this larger $55 \times 25\,\text{mm}$ LVF.

Achieving 25 µm steps over this larger $55 \times 25\,\text{mm}$ while not optically obstructing becomes challenging. There is not a single 1234ms-viable triplet left which does not obstruct in the WS. This optical obstruction also can not be aided by manipulating the parallelogram length. This is due to the fact that it is the parallelogram *link* that obstructs. Widening the parallelogram will have no effect on the vertical position of the parallelogram link. Therefore, the search for the most optimal triplet for the $55 \times 25\,\text{mm}$ LVF is conducted within the 1234ms-viable triplets, optimizing to minimize the area where the motor steps are unacceptably small. This can be visualized as minimizing the black area in the motor step size heatplot (Figure F.26), or in other words, finding the triplet with the largest area of acceptable motor step.

The optimal triplet varies based on the minimum optical obstruction distance that is acceptable. This is illustrated in Figure F.24, where the best performing triplets are highlighted. As the optical obstruction margin increases, so does the area of the LVF that cannot be scanned with 25 µm (or smaller) steps. This presents a balancing act. An optical obstruction margin of 3.5 mm and the accompanying 2.9 % of single-motor failing area was determined to be a good compromise. It is important to note that the failing area is in-fact $2.9 * 2 = 5.8\%$ due to the fact that the two motors of the mechanism fail in different parts of the workspace. The heatplot for the motorstep required of the stepper motor driving θ_1 is shown in Figure F.26, where it it shown to fail in the top left corner of the WS. The stepper motor driving θ_4 will (due to the symmetry of the system) fail the motor step requirement in the *top right* of the WS.

This triplet, in conjunction with VSS-25 stepper motor and a 245 gearbox, is the final recommendation, and considered to be the most optimal and best performing triplet possible. It is able to scan the $40 \times 20\,\text{mm}$ optical area of the small LVF with the requires step size of 25 µm or smaller. It is optimized to be able to scan the maximum area of the $55 \times 25\,\text{mm}$ with 25 µm (or smaller) steps while still maintaining a margin of 3.5 mm to optical obstruction. The maximum joint load is a fraction of the maximum acceptable joint load, and the maximum occurring motor torque is a factor 12.6 times smaller than the detent torque of the VSS-25 stepper motor with a 245 gearbox. It is worth noting that if it is desired to scan the black area of the motor step graph with 25 µm (or smaller) steps it is still possible through microstepping of the stepper motor. This however comes at the cost of dissipation, as detent torque is not able to be used when in between full steps, and therefore the motor can not be depowered. Figure F.24 shows that the triplet (with $5 \times 5\,\text{mm}$ cross-section links) shows no optical obstruction in the WS or in the OOB position. Figure F.26 shows that the motor torque and joint load are acceptable at every point within the optical WS, and that the upper left corner of the WS is where the motor step size is unacceptable. It is worth noting that this same heatplot, but mirrored around the $x = 0$ line applies to the second motor in the system. Therefore, both the top left and right corners of the WS are incapable of 25 µm steps, as in the top left it is on motor that is the limitation, and in the top right it is the other motor that is the limitation. Furthermore, the heatplots show that, even when limited only to the optical WS of the mechanism, the joint flexion ROM is out of reach for a series arrangement of flexpivots. This suggests that scanning a $55 \times 25\,\text{mm}$ LVF with series flexpivots was likely to be infeasible, and that therefore, likely little was lost due to not being able pragmatically calculate the joint flexion ROM required to bring the mechanism to the OOB position.

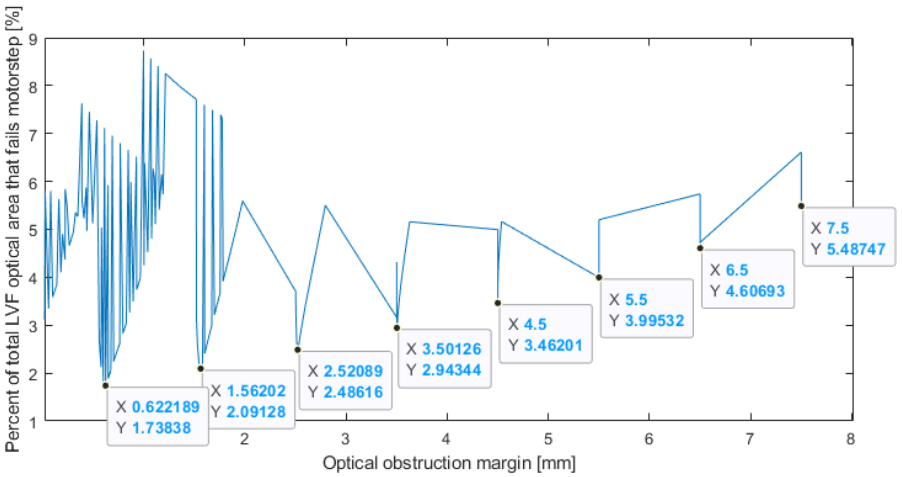

Figure F.24: A plot showing, for all remaining triplets, the percent of total LVF area that fails the motor step requirement vs. the optical obstruction margin.

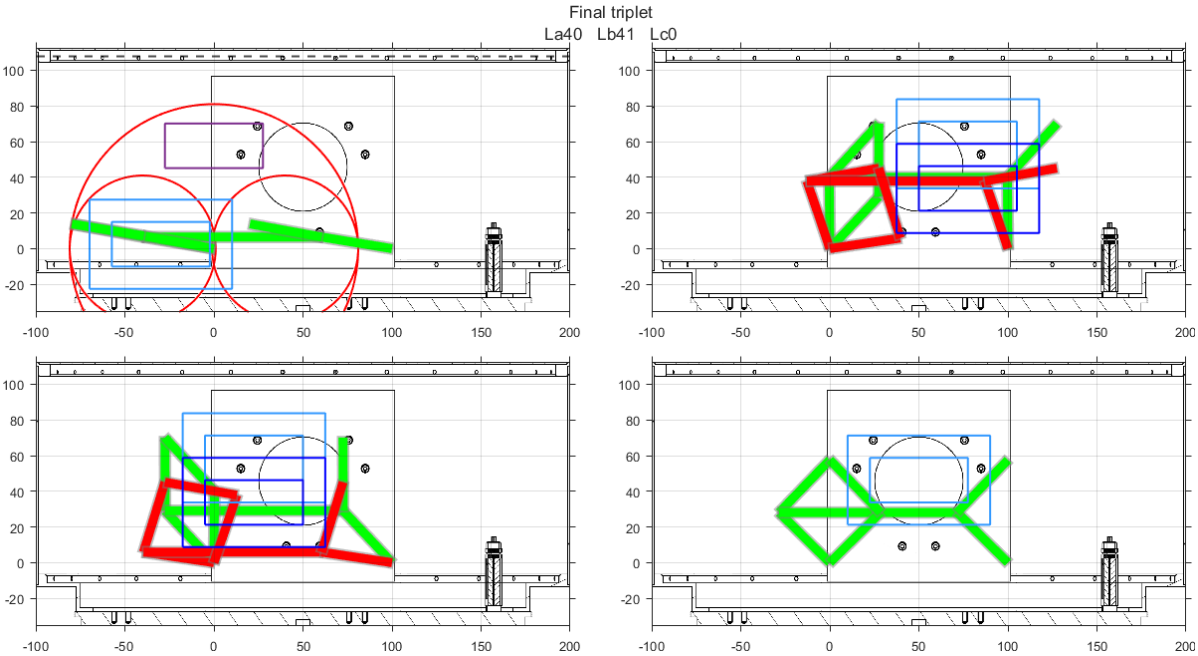

Figure F.25: Cryostat representation of the final triplet.

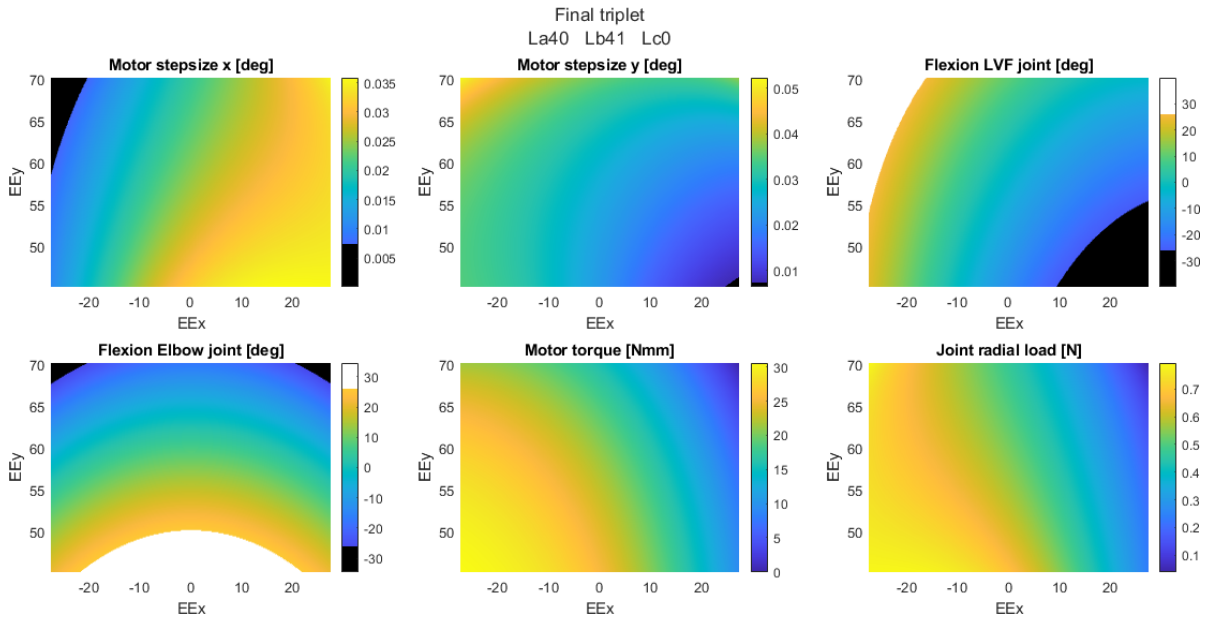

Figure F.26: Heatplots for the final triplet.

G Detailed Design Phase - Tolerance Analysis - Loose Tolerance Investigation

G.1. Tolerance Analysis

An initial tolerance analysis is made using a manufacturing tolerance of ±100 µm. This results in $max\ tolerance = \pm(100+2 \cdot 0.75) = \pm 101.5$ µm. Figure G.2 clearly shows that a manufacturing tolerance of ±100 µm results in X and Y LVF position errors that far exceed what is acceptable. Additionally, in 18 of the 1e5 cases the mechanism was perturbed in such a way that it was incapable of reaching every point in the WS. In these 18 cases there was at least one point in the WS where there was no solution to the kinematic equations. It is clear that the manufacturing tolerances must be tightened. Setting the tolerance to the highest possible tolerance of ±2 µm leads to the results shown in Figure G.5 and G.6, which show that the errors in X and Y position of the LVF are still unacceptably large. The 95 % confidence error in Y is almost acceptable, however the error in X is not. The conclusion is therefore that Measuring the lengths of the links to the highest accuracy possible within SRON does not result in a mechanism wish an acceptably small error in LVF position. Therefore, it is necessary to identify a solution capable of reducing the error further.

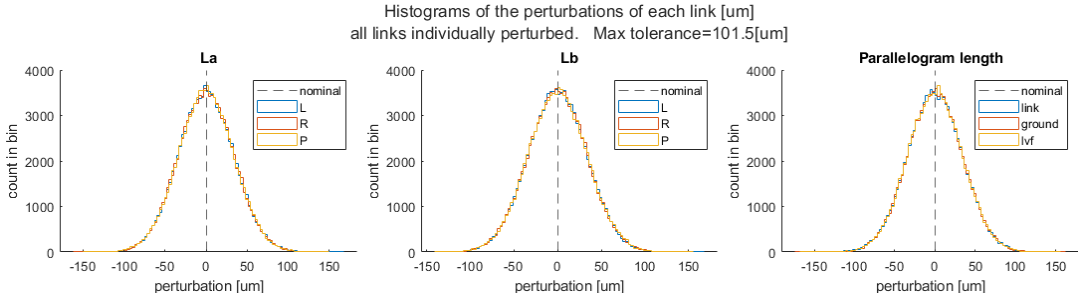

Figure G.1: Histograms showing the perturbation values for each of the different lengths of the mechanism for a manufacturing tolerance of $\pm 100\,\mu m$.

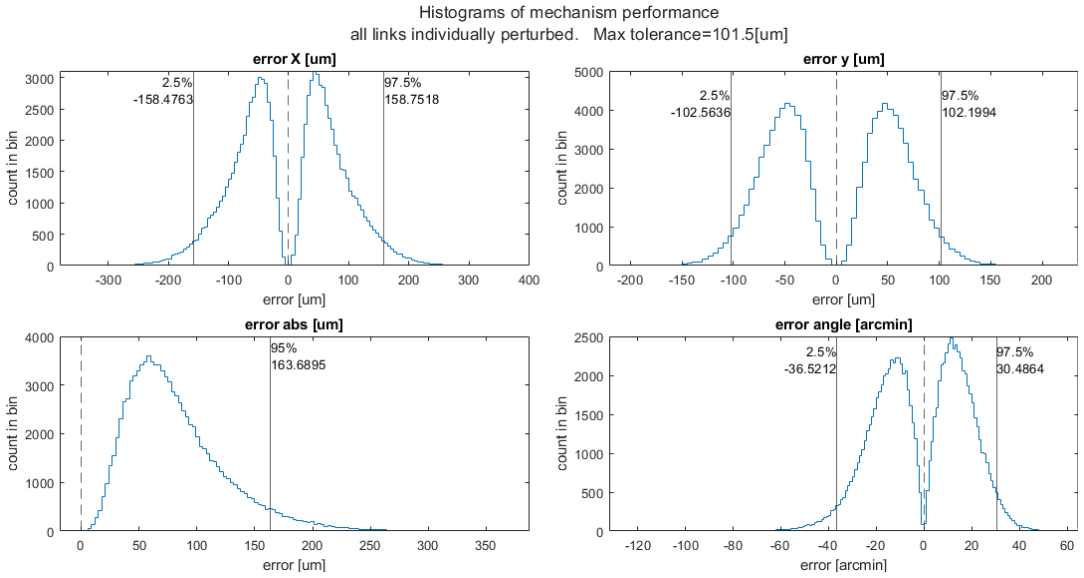

Figure G.2: Histograms showing the performance of the different perturbed mechanisms for a manufacturing tolerance of $\pm 100\,\mu m$. The largest error that occurs anywhere within the WS of a given perturbed mechanism is plotted.

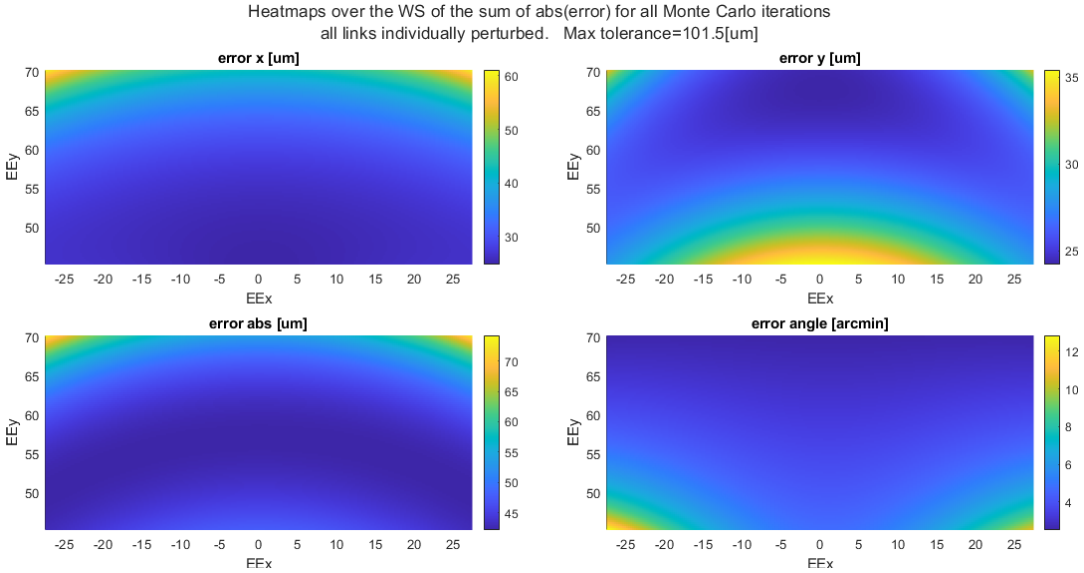

Figure G.3: Heatplots showing where in the WS the largest errors occur for a manufacturing tolerance of $\pm 100\,\mu m$. The heatplots are made by summing the absolute value of the errors over the WS of the different perturbed mechanisms from the Monte Carlo simulation.

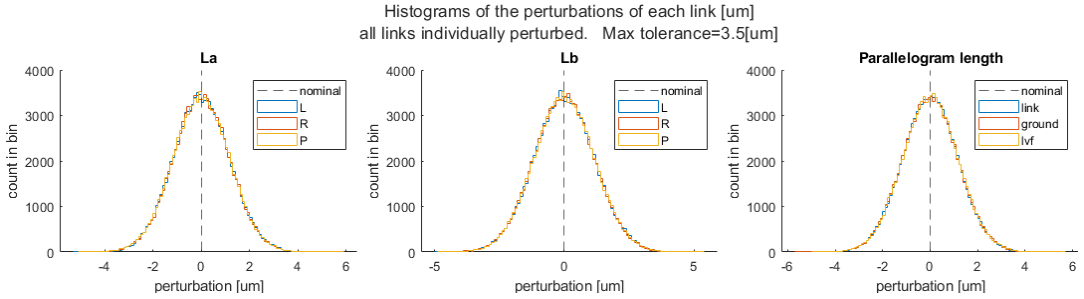

Figure G.4: Histograms showing the perturbation values for each of the different lengths of the mechanism for a manufacturing tolerance of $\pm 2\,\mu m$.

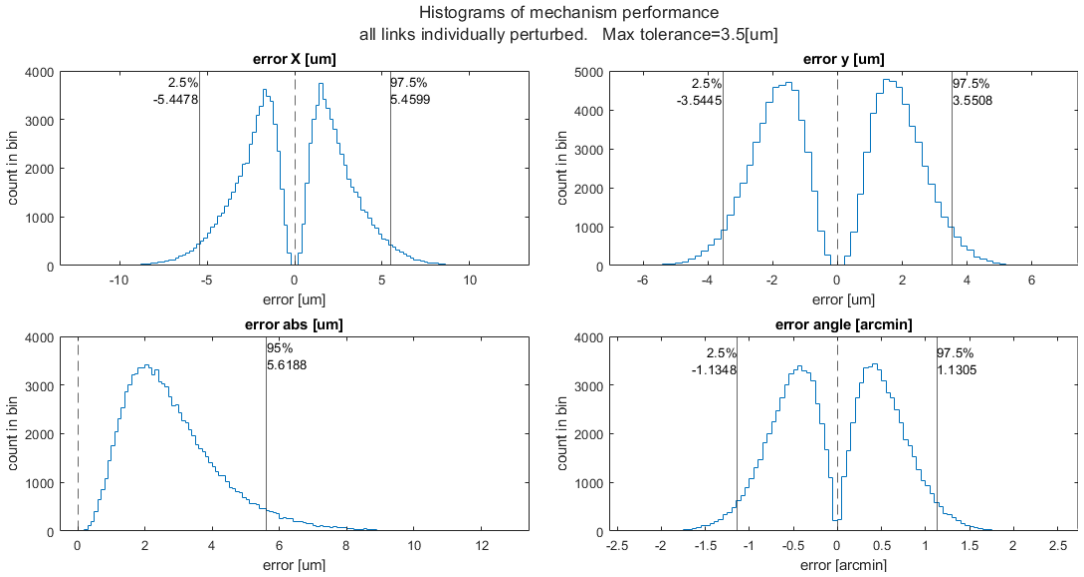

Figure G.5: Histograms showing the performance of the different perturbed mechanisms for a manufacturing tolerance of $\pm 2\,\mu m$. The largest error that occurs anywhere within the WS of a given perturbed mechanism is plotted.

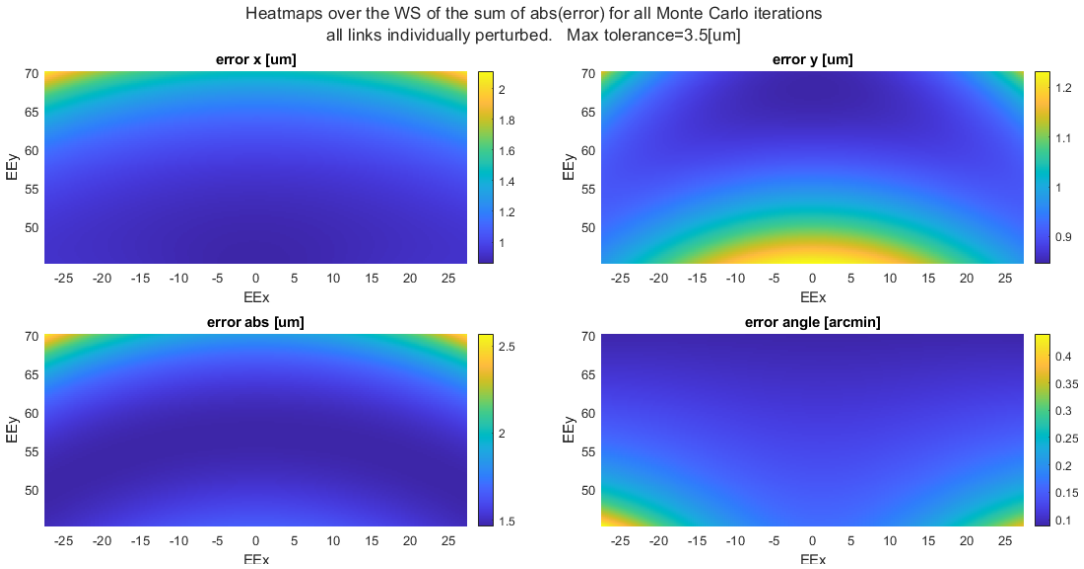

Figure G.6: Heatplots showing where in the WS the largest errors occur for a manufacturing tolerance of $\pm 2\,\mu m$. The heatplots are made by summing the absolute value of the errors over the WS of the different perturbed mechanisms from the Monte Carlo simulation.